COMPUTATIONAL MODELLING OF POLYOXOMETALATES ADSORBED ON METALLIC SURFACES

Xavier Aparicio Anglès

Dipòsit Legal: T. 1525-2013

Computational Modelling of Polyoxometalates Adsorbed on Metallic Surfaces

Xavier Aparicio Anglès

PhD. Thesis
Departament de Química Física i Inorgànica
Universitat Rovira i Virgili
Tarragona, October 2013

Xavier Aparicio Anglès

Computational Modelling of Polyoxometalates Adsorbed on Metallic Surfaces

PhD Thesis

Supervised by Dra. Anna Clotet Romeu and Prof. Josep Maria Poblet Rius

Departament de Química Física i Inorgànica
Grup de Química Quàntica

UNIVERSITAT ROVIRA I VIRGILI

Tarragona, October 2013

UNIVERSITAT ROVIRA I VIRGILI
COMPUTATIONAL MODELLING OF POLYOXOMETALATES ADSORBED ON METALLIC SURFACES
Xavier Aparicio Anglès
Dipòsit Legal: T. 1525-2013

UNIVERSITAT ROVIRA I VIRGILI
COMPUTATIONAL MODELLING OF POLYOXOMETALATES ADSORBED ON METALLIC SURFACES
Xavier Aparicio Anglès
Dipòsit Legal: T. 1525-2013

Departament de Química Física i Inorgànica

Anna Clotet Romeu, professora titular del Departament de Química Física i Inorgànica de la Universitat Rovira i Virgili i Josep Maria Poblet Rius, catedràtic titular del Departament de Química Física i Inorgànica de la Universitat Rovira i Virgili,

Fem constar que la present memòria, titulada:

"Computational Modelling of Polyoxometalates adsorbed on Metallic Surfaces"

ha estat realitzada sota la nostra direcció al Departament de Química Física i Inorgànica de la Universitat Rovira i Virgili per Xavier Aparicio Anglès per a l'obtenció del títol de Doctor i que acompleix els requeriments per poder optar a Menció Europea.

Tarragona, 7 d'octubre de 2013

Els directors de la tesis doctoral

Anna Clotet Romeu

Josep Maria Poblet Rius

UNIVERSITAT ROVIRA I VIRGILI
COMPUTATIONAL MODELLING OF POLYOXOMETALATES ADSORBED ON METALLIC SURFACES
Xavier Aparicio Anglès
Dipòsit Legal: T. 1525-2013

Agraïments / Acknowledgments

No vull estendre'm massa en aquesta part així que seré breu. Si he de començar per algú serà pels meus directors de tesis. Al llarg d'aquests anys he après un munt de coses de vosaltres, Anna i Poblet. Només donar-vos les gràcies per haver fet de mi una persona més humil i haver-me donat les eines que necessito per emprendre el viatge sol, i això va més enllà del món de la ciència. Els dos m'heu donat grans consells per a la vida i això és el que realment m'importa de la tesis. I si algun dia escric un llibre de prosa, que no de poesia, us el dedico. Palabra!

A la resta de "jefes": Xavi L., Toni, Jordi, Coen, Mar, Rosa, gràcies pels consells i bons moments que hem passat.

Als passats: Igor, Nadya, Benjamí, Gerard, Mireia, Yannick, Ramón, Susanna, Eva, m'enduré de vosaltres un bon record. Paraules a part es mereixen gent com l'Àlex i el seu famós "kikifriend" o el seu "I have a question" en unes condicions si més no difícils. Pere, part d'aquesta tesis es tant teva com meva! Joan Petit, espero que les classes de català al tren les recordis molt de temps. Laia, jo no sé com t'ho feies per a que tot fos tant superguay, però molava quan ens passaves aquest bon rollo. Sonia, aparte de tus fantásticas aportaciones a nuestro vocabulario cuotidiano tales como "mátame camión", "rata pelúa", "ay chica, pero como te pones" te recordaremos por tu violencia gratuita y tu sentimiento vasco. Ahora fuera coñas, un placer haber pasado este tiempo contigo. Yo aún te hecho de menos. I finalment, Alberto. Demasiadas cosas han pasado en el despacho, demasiadas confesiones y cosas variadas. Sigo pensando lo que te dije cuando te fuiste, y así será durante mucho tiempo.

Als presents: Murillo, Posada, Pep, Mariano, Pedro espero que tingueu un gran camí en la ciència. Laura, crec que arribaràs lluny, però això de que et fotem el pèl amb facilitat, ho hauràs de millorar. Magda, recorda sempre: "Oh, where is the Sun? OH HERE! Pssss". Saureu, seràs la nostra reina del departament sempre. Pablo A. o "la fallera", nuestro rollo de primos mola, porque solo lo entendemos nosotros. Y admítelo, sabemos que te pasa algo. Jess!!! T'hauré de regalar una foto meva per quan arribin les tardes en que només quedem tu i jo, per no sentir-te tant sola. Ximo, encara somnio amb el que vaig veure a Lanzarote :P. Geisont I, II, III, IV, V Papa del nostre grup, ets el meu ídol i ja saps en quin sentit, guapo!.

Mulet, trobaré a faltar la cara que fiques que em fa riure sempre. Gigi, eres una grandíssima persona, divertido, gracioso, pero no canvies de tema porque sí. Eric, you've been here just for three months but I must say it's been incredible to meet you. And I have to specially thank you for the corrections you did, so part of this thesis is as yours as mine! I per acabar les dues princeses del grup: Núria, només per un cop ho diré. T'estimo molt i et trobaré a faltar, menys quan parles de colors o m'ensenyes la roba que et compres. Pablo J. ets una grandíssima i bellíssima persona, amb un cor més gran que el teu pit, però per favor, no et dediquis a monologuista.

Als de més enllà: Miriam, Idoia. Necessitaria un llibre per cadascuna de vosaltres. La vostra amistat ha estat un pilar fonamental durant tot aquest temps. Des dels mítics cafès que acabaven pitjor que una boda gitana, passant pels viatges, discussions de la vida, concerts, ... però per damunt de tot gràcies per ser les orelles que m'escolten, les cames que em sostenen i les consciències que em guien, cadascuna a la seva manera. Sempre estareu amb mi. I recordeu que "no habrá nube oscura en el cielo capaz de tapar la luz que estos dos soles desprenden!" (amb to sevillano, con deje y duende). Isma i Eli, a l'igual que elles dues han estat importants per mi, vosaltres també ho heu estat i ho sou. Tot i que ara ja no visquem junts m'heu escoltat quan ho he necessitat, ens hem escoltat, ens hem ajudat i el que hem viscut al pis no ens ho traurà ningú. I igual que he dit a les meves dones també us dic que us portaré amb mi sempre. Sou "estrelladamnics"!

A la família. Papa, Mama. Sempre heu estat allí i sé que sempre hi sereu. No dic mai res perquè no sóc de dir res jo però sense vosaltres no estaria aquí. Per tant, aquesta tesis és tant vostra com meva. Espero que estigueu ni que sigui una mica orgullosos de mi. Mon, mai sistaa. Tot i que tens un caràcter de tela, ets ma germana i això es nota. Ara potser estàs lluny i sembla que la sort no t'acompanyi però "quien la sigue la consigue" i tots sabem que a tossuda no et guanya ningú, en el bon sentit de la paraula. Us estimo als tres, aquí queda dit.

Als de Reus. Fèlix i Marta, uns dels meus pilars a Reus. Sónia, Javi, Aida, Jose, Myri, Adri, Gemma, Álex, Jordi, Joan, Marc. Gràcies! I també a les nenes, l'altre pilar que tinc a Reus: Regina, Mireia, Agnès, Martin i Pujola. Això s'ha de celebrar!

I a tots aquells que em deixo però que també porto amb mi. Albert, Puxeu, Maci, Espadas, Aleix, Anna, Lídia, Billie, Juanma, Zarko, Irantzu, Gorka, Patricia, Héctor i

els que m'oblido. Gràcies a tots! Grácias! Merci! Thank you! Tak! хвала! Diolch! Eskerrik Asko! (esto va por ti Sonia!)

Només un últim apunt. El dibuix final no és meu, l'he trobat a internet, concretament a aquesta pàgina:

"http:// http://society6.com/ChristineChangArt/And-so-my-watch-begins_Print

Pel que he vist és una noia que viu d'això així que no és la meva intenció saltar-me les normes legals. Però crec que aquest dibuix de Tyrion Lannister reflexa el que representa acabar la tesis! Així que, després de cinc anys ...

UNIVERSITAT ROVIRA I VIRGILI
COMPUTATIONAL MODELLING OF POLYOXOMETALATES ADSORBED ON METALLIC SURFACES
Xavier Aparicio Anglès
Dipòsit Legal: T. 1525-2013

Resum en català

Els polioxometal·lats (POM) són agregats inorgànics d'òxids metàl·lics. Estan constituïts a partir d'unitats estructurals bàsiques [MO_n] en les que un centre metàl·lic (M), normalment del bloc d de la taula periòdica i en el seu estat d'oxidació més elevat, està envoltat per un nombre n de lligants oxo. Mitjançant la compartició d'arestes o vèrtexs s'obtenen infinitat d'estructures tals com els anions tipus Linqvist, Keggin o Wells-Dawson.

Aquests compostos de naturalesa aniònica, són altament oxidants, extremadament àcids i molt versàtils. Es presenten tant en estat sòlid com en solució aquosa, tot i que també poden ser dissolts en altres medis polars. Una característica també important és que tot i ser aniònics, tendeixen a agregar-se formant estructures nanomètriques d'elevada complexitat. Aquests agregats també s'observen a les interfícies entre dos medis diferents.

Centrant l'atenció en la interfície formada per una superfície i una solució aquosa, els polioxometal·lats s'agreguen formant monocapes que cobreixen dites superfícies. Tot i que les aplicacions d'aquests sistemes són molt diverses, tals com protecció de superfícies, electrocatàlisis o desenvolupament de materials electrònics, no hi han estudis teòrics sobre quina és la naturalesa d'aquesta interacció.

Per tal de poder modelitzar aquesta interacció s'ha de poder descriure de manera correcta el sistema. En aquest cas, la naturalesa periòdica de la superfície així com la mida i l'alta càrrega negativa del POM fan de la modelització d'aquests sistemes una tasca realment complexa. Cal afegir també que molts cops, per a la correcta descripció *ab-initio* de l'estructura electrònica dels POMs, s'ha d'incloure l'efecte del solvent en els càlculs, bé sigui de manera explícita o implícita.

El propòsit d'aquesta tesis és posar les bases per al disseny computacional d'un model que tingui en compte tots els elements que s'acaben d'enumerar i pugui proporcionar informació acurada sobre la interacció entre POM i superfície. Basant-nos amb les dades estructurals que el grup del Dr. Andrew A. Gewirth publicà a finals dels anys noranta sobre la deposició de [α-$SiW_{12}O_{40}$] sobre superfícies de plata, s'ha dissenyat una estratègia computacional que permeti

obtenir informació sobre l'estructura electrònica del sistema, així com també del comportament dels contraions al voltant del polioxometal·lat.

El primer capítol posa en context aquesta tesis, descrivint què són els polioxometal·lats, la seva classificació i les seves propietats. Se'n ressalta la seva capacitat de formar agregats de manera espontània i com aquests es formen al voltant de superfícies tant metàl·liques com no metàl·liques, tal i com ja s'ha exposat en la primera part d'aquest resum.

El segon capítol està dedicat a les aproximacions computacionals i als models utilitzats. S'hi descriuen les diferents metodologies utilitzades, basades en la Teoria del Funcional de la Densitat (DFT) i en models de dinàmica molecular clàssica (MD). També s'enumeren i expliquen les diferents eines utilitzades per analitzar els resultats dels càlculs teòrics tals com l'energia d'interacció iònica, funció de treball, densitat d'estats o funcions de distribució lineal entre d'altres.

Sobre la modelització del sistema, en aquest capítol es fa una descripció de les superfícies emprades, que són les (100) i (111) de plata i or. En base a aquestes, es defineixen les cel·les unitat que s'utilitzen. Per cada superfície se'n plantegen dues de diferents. En un primer cas es descriu la cel·la unitat proposada experimentalment pel grup del Dr. Andrew A. Gewirth, la qual implica la situació de màxim recobriment per a l'adsorció de l'anió α-Keggin. En aquesta cel·la, la distància entre $[\alpha\text{-}SiW_{12}O_{40}]^{4-}$ és relativament curta, fet que comporta una elevada interacció entre veïns. En un segon cas, s'hi descriu una cel·la unitat proposada per tal que la distància entre POMs sigui el suficientment gran com per assegurar una no interacció entre ells. Sobre la construcció final del model es proposen tres situacions diferents: una primera en la que només es considera la superfície i el POM; una segona en la que s'inclouen només els contraions i una tercera que inclou POM, superfície, contraions i solvent.

En els treballs publicats pel Dr. Gewirth es proposen els llocs i modes d'adsorció per al POM, les distàncies entre POM i superfície, els espectres d'infraroig i la informació electroquímica. El tercer capítol està dedicat bàsicament a l'estudi dels llocs i modes d'adsorció, la geometria i l'espectroscòpia d'infraroig. A partir de les quatre cel·les proposades i utilitzant el model amb superfície i POM, s'estudien diferents llocs d'adsorció per a cadascuna d'elles. En les cel·les que impliquen major recobriment, es determina que per la superfície (100), el POM s'adsorbeix via l'eix S_4 en "*Hollow*", amb una rotació respecte la superfície de 37 graus.

Experimentalment també s'indica aquest *site* com el més probable, tot i no indicar cap reorientació del POM sobre la superfície. S'evidencia doncs que les interaccions entre veïns són importants en aquests casos. Pel que fa a la superfície (111), el lloc d'adsorció obtingut és el "Bridge" amb 22^{o} de rotació, reproduint també les dades experimentals. Es posa de manifest però que hi ha diversos modes d'adsorció que es troben a molt poca energia i que per tant, també són termodinàmicament accessibles. En les cel·les de menor recobriment no s'observa reorientació del POM, fet que posa de manifest la importància de les repulsions entre veïns. Les dades estructurals analitzades coincideixen també amb les dades experimentals referents a les distàncies oxigen – superfície del POM, tot i alguna discrepància referida a la separació entre l'àtom central i la superfície. També es reprodueix l'espectre d'infraroig per al *site* "Bridge-22" i s'assignen les bandes als modes normals de vibració. L'espectre concorda plenament amb l'experimental amb l'excepció de la regió entre 900 i 1000 cm^{-1}, fortament dependent de la presència dels contraions. Es reassignen les bandes i es conclou que el pic més intens de l'espectre correspon al a la tensió de l'enllaç Ag-O-W. El model amb contraions no aconsegueix reproduir ni el lloc d'adsorció, ni la geometria ni tampoc l'espectre d'infraroig. És per això que es desestima per a poder estudiar la interacció entre POM i plata.

En el quart capítol s'estudia l'estructura electrònica del sistema. A nivell experimental s'observa que l'espècie $[\alpha\text{-}SiW_{12}O_{40}]^{4-}$ es redueix espontàniament al dipositar-se en aquesta superfície. Malauradament, el nostre model no és capaç de reproduir aquestes dades, ja que els orbitals del POM estan desestabilitzats al no haver-se inclòs els efectes del solvent ni dels contraions. Per aquesta raó es dissenya una estratègia computacional que combina dinàmica clàssica i càlculs quàntics. A partir de la geometria obtinguda en el capítol anterior sobre la cel·la d'alt recobriment per la cara (100), s'inclouen contraions i solvent i es procedeix a realitzar diverses simulacions de dinàmica clàssica per estudiar el comportament d'ambdues espècies. A partir dels resultats obtinguts, es determina les regions de major presència de contraions i s'extreuen diverses geometries a l'atzar de les trajectòries. Un cop calculada l'estructura electrònica del sistema es conclou que, efectivament, el polioxometal·lat es troba reduït quan aquest està en contacte amb la superfície metàl·lica.

Per tal de comprovar la validesa de l'estratègia computacional plantejada, en el capítol cinc es realitza un estudi comparatiu utilitzant polioxometal·lats amb

diferents càrregues i metalls: $[\alpha\text{-}AlW_{12}O_{40}]^{5-}$, $[\alpha\text{-}SiW_{12}O_{40}]^{4-}$, $[\alpha\text{-}PW_{12}O_{40}]^{3-}$, $[\alpha\text{-}SiMo_{12}O_{40}]^{4-}$ i $[\alpha\text{-}PMo_{12}O_{40}]^{3-}$. Procedint de la mateixa manera que en el capítol anterior, es determina que a priori, la càrrega formal del POM no sembla influir de manera significativa en el lloc d'adsorció. Per tal de determinar si el metall té algun efecte en l'adsorció s'estudia l'energia d'interacció iònica així com l'energia d'adsorció dels fragments $W_{12}O_{36}$ i $Mo_{12}O_{36}$. Tots els resultats indiquen que els molibdats s'adsorbeixen millor sobre la superfície i que, tal i com s'observa en el cas dels fragments $W_{12}O_{36}$ i $Mo_{12}O_{36}$, els molibdats es troben a menor distància que els tungstats.

S'observa també que les distàncies entre els POMs i la superfície sí que varien en funció de la càrrega però semblen més curtes del que s'espera. A més, no s'observa la tendència descrita pels fragments sense unitat central. Això ens porta a pensar que tot i que en un primer moment el model sense contraions sembla ser el correcte, estava descrivint una interacció entre superfície i POM més forta del que hauria de ser. Per això, es decideix continuar amb el procediment ordinari i realitzar una optimització final incloent aigües i contraions en la relaxació. Per tal d'arribar a aquest punt es procedeix a la introducció de solvent i contraions mitjançant dinàmica clàssica i se n'obtenen diverses geometries per a cadascun dels cinc sistemes a estudiar. Per comprovar si la optimització introdueix canvis significatius a la nostra metodologia es fa l'estudi de l'estructura electrònica abans i després d'optimitzar els sistemes. Els resultats són clars: no optimitzar els sistemes amb el solvent i els contraions porta a resultats no lògics sobre la transferència de càrrega tals com que aquesta augmenta amb la càrrega formal del POM. Les desviacions a més són majors quan la càrrega dels sistemes augmenta. Amb la optimització es corregeixen aquestes discrepàncies i es conclou que tots els POMs estudiats es redueixen espontàniament quan estan adsorbits sobre superfícies de plata.

La última part de la tesis està dedicada a reformular l'estratègia computacional per tal de poder tractar sistemes altament carregats i també intentar fer un salt cap a un model que ens permeti simular nanopartícules. L'objectiu final és determinar com s'adsorbeix el compost $[\alpha\text{-}AlW_{11}O_{39}]^{9-}$ en nanopartícules d'or. Donat que el sistema és altament carregat, la posada a punt del model es realitza amb el seu homòleg $[\alpha\text{-}AlW_{12}O_{40}]^{5-}$. Com a punt de partida en aquest cas prenem el model amb contraions i el comparem amb el model sense ells. Els resultats indiquen que tot i no obtenir el mateix mínim, les diferències d'energia són insignificants i que

per tant podem partir del model amb contraions. La introducció de solvent revela que el POM no es redueix en contacte amb superfícies d'or.

La conclusió general d'aquesta tesis és que és possible tractar computacionalment l'adsorció de polioxometal·lats sobre superfícies metàl·liques. A partir de diversos models i aproximacions computacionals s'ha aconseguit determinar la reducció espontània dels polioxometal·lats en superfícies metàl·liques i s'ha reproduït també l'espectroscòpia d'infraroig d'aquests sistemes, per bé que el model proposat pot continuar sent millorat per a poder aplicar-lo a altres tipus de POMs i superfícies.

List of Publications

Related with this Thesis

X. Aparicio-Anglès, A. Clotet, C. Bo and JM. Poblet. **"**Understanding the effect of the charge and the metal atoms in the adsorption of α-Keggin anions on silver surfaces" *In preparation.*

X. Aparicio-Anglès, P. Miró, A. Clotet, C. Bo and JM. Poblet. **"**Polyoxometalates adsorbed on metallic surfaces: immediate reduction of $[SiW_{12}O_{40}]^{4-}$ on Ag(100)" *Chem. Sci.* **2012**, 3, 2020-2027

X. Aparicio-Anglès, A. Clotet, C. Bo and JM. Poblet. Towards the computational modelling of polyoxoanions on metal surfaces: IR spectrum characterisation of $[SiW_{12}O_{40}]^{4-}$ on Ag(111). *Phys. Chem. Chem. Phys.* **2011**, 13, 15143-15147

X. López, L. Vila-Nadal, X. Aparicio-Anglès, JM. Poblet. "Theoretical View on the Origin and Implications of Structural Distortions in Polyoxometalates" *Physics Procedia* **2010**, 8, 94-103

Not related with this Thesis

X. Aparicio-Anglès, N. Alegret, A. Clotet, A. Rodríguez-Fortea and J. M. Poblet. "Endohedral Metallofullerenes Containing Lanthanides: A Robust Yet Simple Computational Approach" *J. Phys. Chem. C* **2013**, 117, 12916-12921

N. Alegret, M. Mulet-Gas, X. Aparicio-Anglès, A. Rodríguez-Fortea and J. M. Poblet. "Electronic Structure of IPR and non-IPR endohedral metallofullerenes: Connecting orbital and topological rules" *C. R. Chim.* **2012**, 15, 152-158

M. N. Chaur, X. Aparicio-Anglès, B. Qu. Mercado, B. Elliott, A. Rodríguez-Fortea, A. Clotet, M. M. Olmstead, A. L. Balch, J. M. Poblet and L. Echegoyen. "Structural and Electrochemical Property Correlation of Metallic Nitride Endohedral Metallofullerenes" *J. Phys. Chem. C* **2010**, 114, 13003-13009

UNIVERSITAT ROVIRA I VIRGILI
COMPUTATIONAL MODELLING OF POLYOXOMETALATES ADSORBED ON METALLIC SURFACES
Xavier Aparicio Anglès
Dipòsit Legal: T. 1525-2013

UNIVERSITAT ROVIRA I VIRGILI
COMPUTATIONAL MODELLING OF POLYOXOMETALATES ADSORBED ON METALLIC SURFACES
Xavier Aparicio Anglès
Dipòsit Legal: T. 1525-2013

Contents

Contents

UNIVERSITAT ROVIRA I VIRGILI
COMPUTATIONAL MODELLING OF POLYOXOMETALATES ADSORBED ON METALLIC SURFACES
Xavier Aparicio Anglès
Dipòsit Legal: T. 1525-2013

UNIVERSITAT ROVIRA I VIRGILI
COMPUTATIONAL MODELLING OF POLYOXOMETALATES ADSORBED ON METALLIC SURFACES
Xavier Aparicio Anglès
Dipòsit Legal: T. 1525-2013

Chapter 1
Introduction and Scope of the Thesis

Inorganic metal oxygen clusters, commonly known as polyoxometalates, are a vast class of inorganic compounds that is unequalled in terms of molecular and electronic structural versatility, reactivity and relevance. Although their chemistry is well known in aqueous media, they are also used in combination with other chemical compounds to obtain new materials with new applications. This chapter presents a general overview to the polyoxometalate world and to these new composite materials. The final part will detail the main aims of this thesis.

UNIVERSITAT ROVIRA I VIRGILI
COMPUTATIONAL MODELLING OF POLYOXOMETALATES ADSORBED ON METALLIC SURFACES
Xavier Aparicio Anglès
Dipòsit Legal: T. 1525-2013

1.1. The Polyoxometalates

1.1.1. An historical perspective of polyoxometalates

"*Sur la Mine de Plomb ou Molybdène*". This is the tittle, translated from Swedish to French, of the first known article related with polyoxometalates (POMs).[1] Written by the Swedish chemist Scheele and published in 1778, this paper is the first description of molybdenum blue, observed in certain fountains from Idaho Springs, Colorado, and from the Valley of the Ten Thousand Smokes (Alaska).

In the 19th century, Berzelius reported the synthesis of what we nowadays know as phosphomolybdenum acid, $[PMo_{12}O_{40}]^{3-}$.[2] Also in this century, Marignac carried out a systematic study of their tungsten homologues, the phosphotungstate acid, $[PW_{12}O_{40}]^{3-}$.[3] However, it was not until the 20th century, when POM's structure started to be revealed, thanks to the development of powerful spectroscopic techniques like X-Ray diffraction. Is at this point when names such as Keggin or Dawson became familiar in the POMs family.[4]

The big "explosion" in the polyoxometalate field occurred almost thirty years ago, in the 80s with the improvement of analytical and computational techniques.[5] Since then, new types of POM appear and new materials based on them are synthesized or characterized every year. Indeed, POM chemistry is an old field that keeps presenting us with new and marvellous surprises day by day.

1.1.2. Structure and Properties

Polyoxometalates are a well-defined class of discrete anionic metal-oxide clusters.[6] We can view them as a result of $[MO_n]$ building blocks condensation where M (or addenda atom) is typically a metal from the d-block. $[MO_n]$ blocks most commonly incorporate W, Mo or V as metals (M) and posses a number of oxo ligands between four and seven. These units can share edges and vertexes that lead to an uncountable number of different structures, which depends primarily on the synthesis procedure.[7] Within the same structure can appear a combination of different metal centers, other elements of the periodic table usually referred to as *heteroatoms*, and even different kinds of ligands such as sulfur, nitrogen or fluorine in place of oxygen.[8]

There are several ways to rationalize the entire POM family. One of the most usual is classify them based on their composition. Thus, we can distinguish two different subsets:

- ***Isopolyanions*** are those POMs in which no heteroatom is present in the structure. The most popular structure in this family is the Lindqvist anion $[M_6O_{19}]^{q-}$. (See Figure 1.1 a))
- ***Heteropolyanions*** are those metal oxide clusters that have incorporated heteroatoms like $[SiO_4]^{4-}$, $[SO_4]^{2-}$, $[SO_3]^{2-}$ or $[AsO_4]^{4-}$ as examples. Two of the iconic POMs belonging to this family are the Keggin anion, $[XM_{12}O_{40}]^{q-}$, and the Wells-Dawson anion, $[X_2M_{18}O_{60}]^{q-}$. (See Figure 1.1 b) and c))

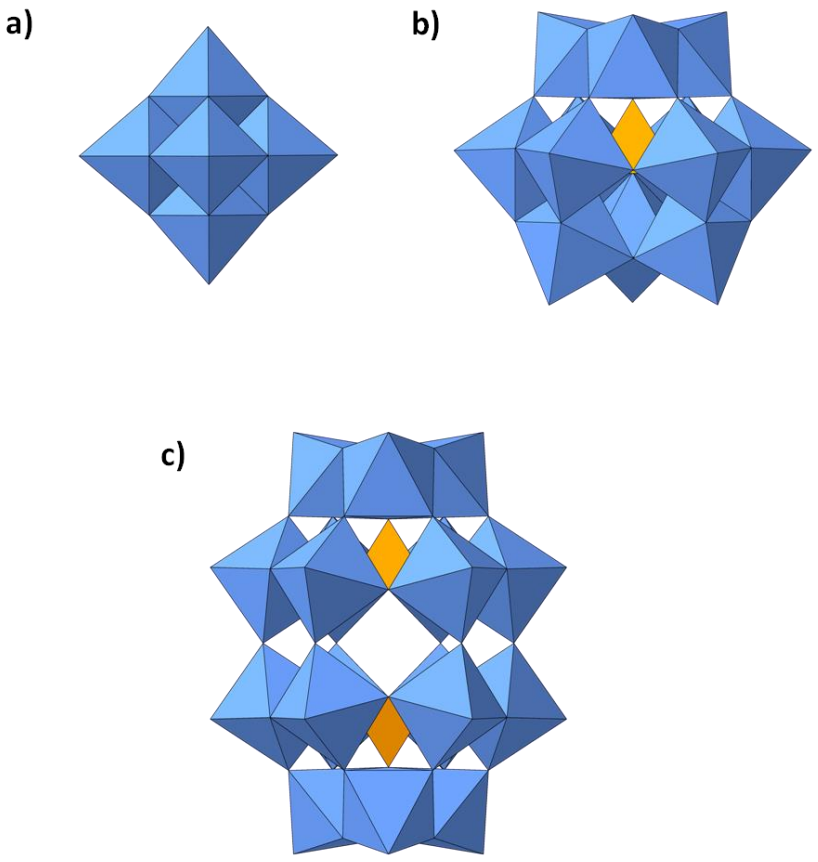

Figure 1.1 Polyhedral representation for a) Linqvist, b) α-Keggin, and c) Wells-Dawson anions.

The addenda atom is in its highest oxidized state whereas the oxo ligands are fully reduced, bearing similarities to the archetypical metal-oxide surfaces.[9] When POMs are reduced, incoming electrons are allocated to empty metallic orbitals. These electrons are delocalized over many metallic centers by hopping mechanisms, which lead to minimal structural changes upon reduction.[10] As a result, POMs can be reduced very low negative potentials.

Heteropolyanions are known to be superacids, since they present very low pk_a constants. As a consequence of this, they are commonly used in acid-base reactions, and as proton conductor as well. Although being a superacid species, they can polymerize at very low pH values, whereas they decompose at basic pH.

Other typical features of POMs are related to their magnetic properties. As was mentioned previously, POMs can incorporate more than one metal type into their structure. If this atomic type has magnetic nature, the POM can posses also magnetic properties.

1.2. Synthesis, modification and functionalization

The formation process of polyoxometalates is simple and typically involves few steps. The aggregation of the different building blocks can be managed by controlling experimental variables such as: (1) concentration and type of metal oxide anion, (2) concentration and type of heteroatom oxide, (3) ionic strength, (4) pH, (5) presence of additional ligands, (6) reducing agent, (7) pressure and temperature during the synthesis, (8) counterions, and (9) processing method. Generally speaking, synthesis of polyoxometalates can be summarized as:

$$x\, MO_4^{n-} + z\, H^+ \rightarrow \left[M_x O_y\right]^{m-} + \frac{z}{2}\, H_2O$$

The introduction of new synthetic approaches has let to the discovery of novel architectures that could not be found otherwise. Two salient examples are that of top-down syntheses that obtain the building blocks from the decomposition of larger POMs, and the in-flow synthesis based on mixing different reaction mixtures in order to allow reactions between different intermediates.[11]

From classic POM architectures we can also obtain lacunary polyoxometalates (L-POMs), *i.e.* POMs with vacancies. Depending on the polyoxometalate, lacunary architectures can be obtained differently. One route is related to the basic hydrolysis of the plenary cluster, although in some cases (such as lacunary Keggin clusters) the L-POM can be directly prepared under strict pH control.[12]

Lacunas are nucleophile regions that can easily assemble with other lacunary POMs for obtaining larger polyanions. However, they can also react with different electrophiles capable of octahedral coordination. For example, reactions with other transition metals compounds leads to the aforementioned mixed-metal polyoxometalates, such as $[PVW_{11}O_{40}]^{4-}$, $[PNbW_{11}O_{40}]^{4-}$, and $[PTaW_{11}O_{40}]^{4-}$.[13]

As said, lacunary POMs can be employed as ligands for active inorganic catalysts. This class of POMs are generally known as transition metal-substituted polyoxometalates (TMSPs). In these systems, lacunary POMs can stabilize from little to large metallic complexes. For example $[Ru_4O_6(H_2O)_4(PW_{10}O_{36})_2]^{10-}$ in which Ru_4O_6 moiety is stabilized by lacunary $\{PW_{10}\}$ fragments, is known for their remarkable catalytic properties in the oxidation of water.[14] An example of large metallic complexes stabilized by lacunary POMs is the $[Mn^{II}_{19}(OH)_{12}(SiW_{10}O_{37})_6]^{34-}$, which has revealed a significant catalytic activity towards the oxygen evolution reaction (OER).[15]

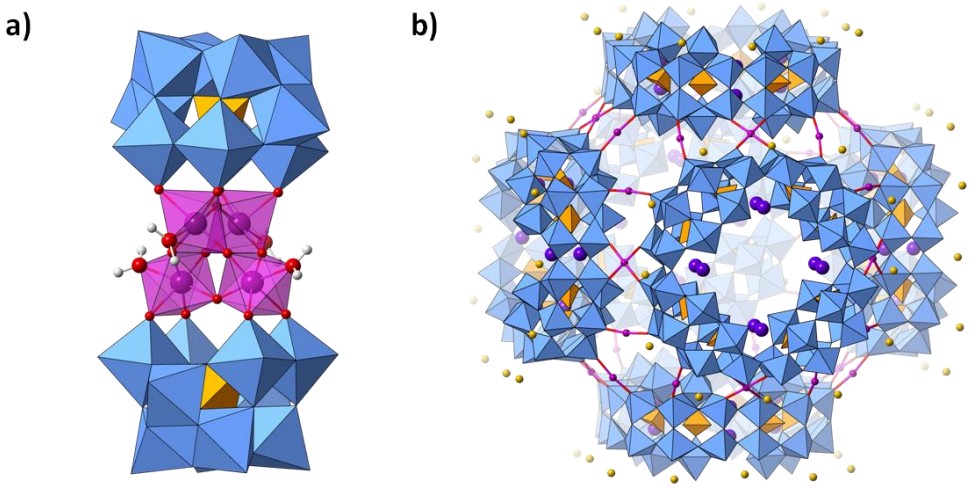

Figure 1.2 Polyhedral representation for a) $[Ru_4O_6(H_2O)_4(SiW_{10}O_{36})_2]^{10-}$ and b) face-centered unit cell for $[Mn_8(H_2O)_{48}(P_8W_{48}O_{184})]^{24-}$ with the corresponding counterions.

They can even self-assemble into 3D extended frameworks, such as the reported by the Cronin Group where in which $\{P_8W_{48}\}$ fragments are linked by Mn^{II} centres. It represents an all-inorganic porous system capable to capture other metals by changing the oxidation state of the Mn^{II} linkers.[16]

Organic frameworks can also be incorporated into POM structures (see Figure 1.3).[17] The combination of organic ligands and inorganic polyoxometalate supports offers diverse options for their integration into functional materials and devices, as well as applications in catalysis, photochemical assisted catalysis or microelectronics for example.

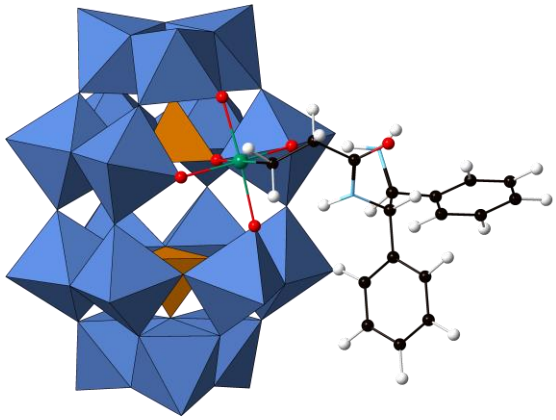

Figure 1.3 Polyhedral and ball-and-stick representation for the α_1-$[P_2W_{17}O_{61}(Sn\text{-}\{N\text{-}(2\text{-amino-}1,2\text{-diphenylethyl})propionamide\}]^{7-}$, an example of organofunctionalized Wells-Dawson polyoxometalate.[18]

1.3. POM-based materials

One of the principal interests in developing new functional materials is the rational design of materials with a certain desired set of properties for targeting specific applications. These materials can be composed of one molecular entity or possess a combination of different chemical components. Materials corresponding to the latter category are usually referred as hybrid materials or composites.

The performance of POM-based materials strongly depends on the interaction between the POM and other compounds present in the substance, which can vary

between weak to covalent. Based on the nature of these interactions we distinguish between Class I Materials in which the different components interact *via* electrostatic, Van der Waals or Hydrogen bonding; and Class II that includes materials held together by means of strong covalent bonds.[19]

Self-assembled POM architectures such as blackberries are perfect examples of Class-I POM-based materials. Mo_{132}[20] (see Figure 1.4) or Mo_{154}[21] POMs are building blocks of this type of structures, in which both solvent and counterions play a determinant role in nucleation and stability. Solvation and counterion attachment to the POM surface reduces the repulsion between adjacent building blocks. In addition, Van der Waals and H-bonding between the solvent and POM also influences the formation of these large structures.[22]

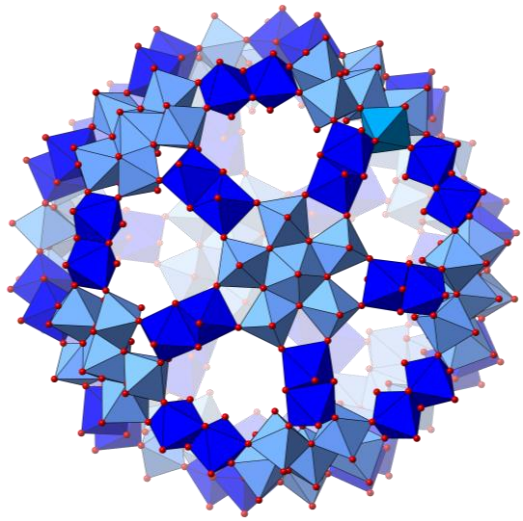

Figure 1.4 Polyhedral representation of the $\{Mo_{132}\}$ with Mo^{VI} in low blue and Mo^{V} moieties in dark blue.

In addition to solvents and counterions, POMs can also interact with other ionic materials like ionomers (or ionic polymers), where POMs are trapped in a cationic polymeric network. The resulting composite material can be used to obtain a catalytic solid material with accessible catalytic active sites, as proton membranes in fuel cells or rechargeable molecular cluster batteries, where the environment allows for the successive reduction of the POM.[23]

Covalent functionalization of POMs (Class II materials) mainly relates to their organic functionalization, although it also encompasses organometallic/inorganic catalysts. The organic framework can be used for grafting POMs onto surface or polymeric matrixes, for turning POMs into surfactant agents or combining organic conjugated systems with the photochemical properties of POMs.[24]

Composite materials can also be classified by their final dimensionality, which can range from zero dimensions to three dimensions. For example, the aforementioned micelles formed by $\{Mo_{132}\}$ are considered as zero-dimensional (0D) materials; one-dimensional (1D) materials are related to fibres or belts; two-dimensional (2D) materials are modified surfaces and films, and three-dimensional (3D) are POM crystals. The next section will emphasize on the 2D materials, the main topic of this thesis.

1.3.1. 2D POM-based materials

POM-based materials can be 2D structured by means of thin films. This planar disposition maximizes the interfacial surface with a substrate or a matrix, a feature of great utility for various different applications, as will be discussed further this section.

POMs can be covalently anchored on a surface *via* organic frameworks. To do so, it is necessary to functionalize both, surface and POM. The advantages of this strategy with respect to "raw" POM's chemistry are: (1) enhancing synergistic effects between the moieties, (2) rational design of extended architectures, (3) improved dispersion in matrices and (3) improvements of the stability.[24] An example of this kind of anchoring can be found in the fixation of $[(MeO)TiW_5O_{18}]^{3-}$ on derivatized silicon surfaces.[25]

Although POMs can be linked by means of strong covalent bonds, in most cases the immobilization of POMs or their structuration in thin films relies on non-covalent interactions with the support. Polyoxometalates spontaneously aggregate at aqueous interfaces, due to the high surface tension of water.[26] Some techniques have been developed to take advantage of this feature, allowing for control over the thickness and the composition of thin films. Several of them are summarized below. It is worth mentioning that this capacity was exploited in the late eighties for the modification of electrode surfaces to modify their response for

the Hydrogen Evolution Reaction (HER)[27] was long exploited during the nineties.[28]

One way to assist the monolayer formation is the dip coating method (see Figure 1.5) or electrodeposition. Dip coating consists of a repeated immersion of the electrode on a POM solution, whereas electrodeposition uses electric potential as the driving force for adsorption.

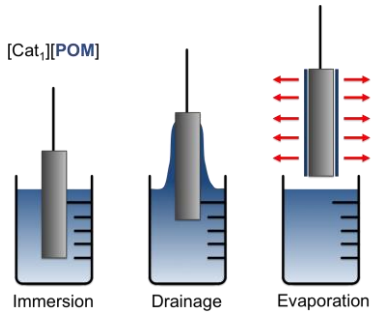

Figure 1.5 Schematic representation of the dip coating technique.

Quite similar to the dip coating method is the extensively employed Layer-by-Layer (Lbl) method (see Figure 1.6). It is used for preparing hybrid thin films by immersion of the support into different substrate solutions repeatedly. The substrates are oppositely charged, so that when POMs are employed, the secondary material must be cationic. Examples of thin films obtained by means of Lbl include P_5W_{30}-poly(ethyleneimine) layers, synthesised by Einaga *et al.*[29] and the POM-porphyrin films obtained by the Ruhlmann group, with applications in light-driven synthesis of metallic nanoparticles.[30]

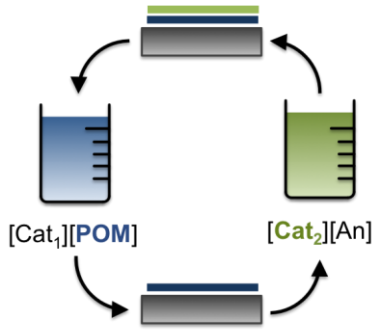

Figure 1.6 Schematic representation of the Layer-by-layer technique.

The Langmuir-Blodgett technique (Figure 1.7) is relatively similar to the dip coating and the LbL methods. In this case, a film formed at the air-aqueous interface is deposited on an immersed mobile support. As it was the case with the two aforementioned methods, the number of immersions controls the thickness of the layer. POMs encapsulated in surfactant shells, or biphasic solutions of POMs and amphiphile are deposited on a surface using this method.[31]

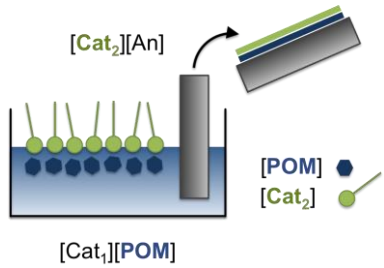

Figure 1.7 Schematic representation of the Langmuir-Blodgett technique.

Some of the applications of thin films have been mentioned previously. In electrocatalysis for example, POMs play several roles simultaneously. The POM can act as a catalyst itself, as it was noted with the Hydrogen Evolution Reaction (HER), and can rapidly transfer incoming electrons to the electrode with minimal resistance. They can also be combined with other catalytically active components, including metal nanoparticles. POMs thermodynamically stabilise nanoparticles, and aid them in linking to other electronically active materials such as Single Walled Carbon Nanotubes (SWCNTs). Pt/Ru nanoparticles linked *via* $H_3PMo_{12}O_{40}$ or $H_3PW_{12}O_{40}$ to the electrode or the hybrid Pt-POM-Carbon Nanotube system have displayed potential utility in for methanol electroxidation reactions.[32] An additional example involves the aforementioned $\{Ru_4\}\{SiW_{10}\}_2$ complex, which, when embedded in a functionalised multi-wall carbon nanotube presented promising results for the Oxygen Evolution Reaction (OER).[33]

One of the state-of-the-art applications of POMs on surfaces involves their use in electronic materials. This is primarily a consequence of two features: (1) overlap between the POM and neighbouring clusters is not really strong, so electrons remain trapped within the polyanion; (2) POMs can act as electron transfer mediators that are highly responsive to environmental changes, both chemical and physical. Examples of these applications are POMs used in Li-ion batteries,[34] as single molecular magnets;[35] and as electronic sensors.[36]

1.3.2. Structural determination of 2D-POM based materials

The large number of POM types with different properties and applications, combined with the great variety of matrix materials, results in an unfathomable number of possible new materials with fashionable applications. In order to drive this search in a rational manner it is therefore necessary to understand the interaction between POMs and matrix materials. One of the firsts steps of this search is to unravel how polyanions are interacting with the surfaces, in specific cases.

During the nineties, several groups were interested in determining how Keggin anions were adsorbed on various surface types, including graphite, graphene, carbon, and gold.[37] At the end of the nineties, the group of A. A. Gewirth focused their attention on adsorption on silver surfaces. The primary difference between this system and the others studied is the strength of interaction with silver; the anion-surface interaction is much stronger in this case.

By means of STM imaging, Gewirth and co-workers proposed different unit cells for the adsorption of $[\alpha\text{-}SiW_{12}O_{40}]^{4-}$ on Ag(100) and Ag(111) surfaces.[38] They also combined the STM images with X-Ray Specular Diffraction for obtaining more precise information about the system. The resulting data suggested that the distance between the surface and the terminal oxygens was around 2.06 Å,[38c] which was considered to be an evidence of the strong interaction between the two moieties. They also performed experiments that revealed the possibility of spontaneous reduction of the silicotungstate acid after adsorption.[39]

1.3.3. Nanoparticles protection

As in the case on flat surfaces, POMs also attach to the surface of nanoparticles (NPs), but the role they play here is somewhat different. NPs are thermodynamically unstable because of their tendency to lower their very high surface energy.[40] The best way to stabilize them is protecting them by deposition of different molecules. POM-protected NPs can be obtained by substitution of existing stabilizers like citrate anions.[41]

It is also possible to obtain *in-situ* POM-protected NPs. In fact, POMs can be used for the synthesis of NPs as a reducing and nucleating agent. At the same time, the negative charge of the POM also allows for a good dispersion of these POM-protected NPs onto an electric active material such as graphene or carbon nanotubes used in electro-oxidation reactions.[32a]

However in the case of NPs we also realize that very few articles are related to with how POMs are deposited onto their surfaces. Recently, by using Cryo-Tem images and surface plasmon, Weinstock *et al*. have been able to provide evidences of the adsorption of POMs on gold nanoparticles, also indicating the important role of counterions in the stability of the monolayer.[42]

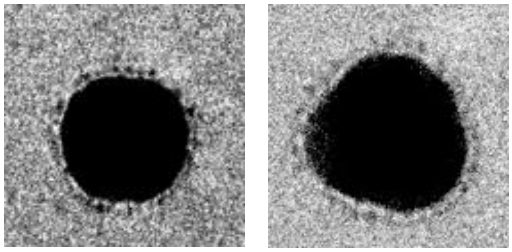

Figure 1.8 Cryo-TEM images for $AlW_{12}O_{40}^{5-}$ on gold nanoparticles with Cs^{+} as counterion, obtained by the group of Ira Weinstock.

1.4. Role of computational chemistry

Computational chemistry has been demonstrated to be a key tool in the understanding of the physical and chemical properties of polyoxometalates. Their 'relationship' started around thirty years ago, in 1986, when Xα studies were carried out to study the frontier orbitals of $[PMo_{12}O_{40}]^{3-}$.[43] In following years, new methods were also applied for the study of POMs, including SCF CNDO/2 and Hartree-Fock. The irruption of DFT however, marked a turning point in their computational study. DFT allowed introducing, with remarkably little computational demand, the effect of electron correlation, which is not included in the aforementioned methods. Present DFT calculations also include other effects such as relativity, solvation or better description of the correlation by means of hybrid functionals. Examples of the various topics and developments achieved during these years include the improved understanding of their electronic

structure, redox properties, reactivity, spectroscopy and magnetism.[44] Selected developments will be briefly reviewed in this thesis.

The study of properties derived from the behaviour of POMs in solution does not require the same level of accuracy as for the aforementioned topics. Classic Molecular Dynamics, based on Newtonian equations in which the electronic part is no longer considered, is the most appropriate tool for these kind of investigations. Examples of such studies include are ion pairing,[45] interaction with cations,[46] the water structuration around the POM,[47] and interphase behaviour.[48]

Thanks to improvements in the computational resources, it has become possible to study larger systems with high precision. This is the case with 2D-POM based materials. However, this kind of systems present several issues that must be reviewed. Firstly, we should consider that POMs are anions interacting with the surface. For smaller adsorbates such as Cl^-, CO_3^{2-} or SCN^-, charge does not represent a huge problem. The group of F. Illas demonstrated that the studying the adsorption of these species with and without charge consideration yields approximately the same results.[49] However, POMs are large polyanions and the charge becomes more important, as we will see later in this thesis. In fact, the adsorbate size becomes another important drawback, as well as the periodic nature of the surface. Fortunately, thanks to ever-increasing computational power, this represents a minor problem with respect to the charge of the POM.

Despite this, various groups have started to study the direct interaction of POMs with planar surfaces in recent years. In 2005, Borzenko *et al*. studied the self-inhibition of the Anderson $[CoMo_6O_{24}H_6]^{3-}$ in the mercury electrode by means of a cluster model.[50] They compared different POM orientations and determined how the formation of an adlayer is responsible for the inhibition. In 2010, Lefebvre, Sautet and co-workers analysed the adsorption of $H_3PMo_{12}O_{40}$ on silica surfaces.[51] They revealed the formation of hydrogen bonds between POM protons and OH groups from silica and the dehydration process, leading to POM-O-Si bonds. DFT studies also permitted them to construct stability diagrams as a function of temperature and the partial pressure of water for this system.[52] Finally, in 2012, S. Wen *et al*. studied the adsorption of $[PMo_{12}O_{40}]^{3-}$ on graphene, showing that the dominant interactions between the surface and POM were electrostatic.[53]

1.5. Scope of the Thesis

Theoretical modelling of adsorption of polyoxometalates is still a challenge. The large size of the formal adsorbates in addition to the periodic nature of the system has limited the exploration of this field until now. This thesis intends not to be definitive work but a starting point for understanding the interactions between a POM and a surface.

The combination of different computational models and approaches, as well as the enhancement of the computational resources is evident throughout this work. During these years we sought to answer different questions and to design a strategy able to describe these systems.

The results presented here will concern the following topics:

- Based on the structural information reported by Gewirth and co-workers, we want to study the adsorption active sites for $[\alpha\text{-}SiW_{12}O_{40}]^{4-}$ on low index silver surfaces.

- To compare experimental spectroscopic data for the $[\alpha\text{-}SiW_{12}O_{40}]^{4-}$ anion adsorbed onto silver surfaces.

- To design a strategy for including the effects of solvation and counterions in our calculations.

- To determine if the $[\alpha\text{-}SiW_{12}O_{40}]^{4-}$ polyoxometalate is spontaneously reduced when it is adsorbed on silver surfaces.

- To extend our strategy to a comparative study of the behaviour of $[\alpha\text{-}XW_{12}O_{40}]^{q-}$ with X = Al, Si and P and q = 5, 4 and 3, as well as $[\alpha\text{-}XMo_{12}O_{40}]^{q-}$, with X = Si and P and q = 4 and 3, improving if necessary the strategy developed.

- To model highly charged POMs concretely the $[\alpha\text{-}AlW_{12}O_{40}]^{5-}$ on gold surfaces as a test system for even highly charged systems such as the lacunary anion $[\alpha\text{-}AlW_{11}O_{39}]^{9-}$.

References Chapter 1
Introduction and Scope of the Thesis

[1] L. Cronin, A. Muller, *Chem. Soc. Rev.* **2012**, *41*, 7333-7334.
[2] J. J. Berzelius, *Annalen der Physik* **1826**, *82*, 369-392.
[3] C. Marignac, *Ann. Chim. Phys.* **1864**, *3*, 1.
[4] (a) J. Keggin, *Nature* **1933**, *131*, 908; (b) H. D'Amour, *Acta Crystallographica Section B* **1976**, *32*, 729-740; (c) B. Dawson, *Acta Crystallographica* **1953**, *6*, 113-126.
[5] M. T. Pope, A. Müller, *Angew. Chem.-Int. Edit. Engl.* **1991**, *30*, 34-48.
[6] M. T. Pope, *Heteropoly and Isopoly Oxometalates, Vol. 8*, Springer-Verlag, Berlin, **1983**.
[7] D.-L. Long, R. Tsunashima, L. Cronin, *Angew. Chem., Int. Ed.* **2010**, *49*, 1736-1758.
[8] (a) E. Cadot, B. Salignac, S. Halut, F. Sécheresse, *Angew. Chem., Int. Ed.* **1998**, *37*, 611-613; (b) R. J. Errington, R. L. Wingad, W. Clegg, M. R. J. Elsegood, *Angew. Chem., Int. Ed.* **2000**, *39*, 3884-3886; (c) J. B. Strong, G. P. A. Yap, R. Ostrander, L. M. Liable-Sands, A. L. Rheingold, R. Thouvenot, P. Gouzerh, E. A. Maatta, *J. Am. Chem. Soc.* **2000**, *122*, 639-649; (d) A. Bino, M. Ardon, D. Lee, B. Spingler, S. J. Lippard, *J. Am. Chem. Soc.* **2002**, *124*, 4578-4579.
[9] J. B. Moffat, *Metal-Oxygen Clusters. The Surface and Catalytic Properties of Heteropoly Oxometalates*, 1st ed., Springer, New York, **2001**.
[10] J. Maestre, J. Poblet, C. Bo, N. Casañ-Pastor, P. Gomez-Romero, *Inorg. Chem.* **1998**.
[11] H. N. Miras, J. Yan, D.-L. Long, L. Cronin, *Chem. Soc. Rev.* **2012**, *41*, 7403-7430.
[12] (a) G. Herve, A. Teze, *Inorg. Chem.* **1977**, *16*, 2115-2117; (b) J. Canny, A. Teze, R. Thouvenot, G. Herve, *Inorg. Chem.* **1986**, *25*, 2114-2119.
[13] E. Radkov, R. H. Beer, *Polyhedron* **1995**, *14*, 2139-2143.
[14] (a) A. Sartorel, P. Miró, E. Salvadori, S. Romain, M. Carraro, G. Scorrano, M. D. Valentin, A. Llobet, C. Bo, M. Bonchio, *J. Am. Chem. Soc.* **2009**, *131*, 16051-16053; (b) Y. Geletii, C. Besson, Y. Hou, Q. Yin, D. Musaev, D. Quiñonero, R. Cao, K. Hardcastle, A. Proust, P. Kögerler, C. Hill, *J. Am. Chem. Soc.* **2009**, *131*, 17360-17370.
[15] B. S. Bassil, M. Ibrahim, R. Al-Oweini, M. Asano, Z. Wang, J. van Tol, N. S. Dalal, K.-Y. Choi, R. Ngo Biboum, B. Keita, L. Nadjo, U. Kortz, *Angew. Chem. Int. Ed.* **2011**, *50*, 5961-5964.
[16] S. G. Mitchell, C. Streb, H. N. Miras, T. Boyd, D.-L. Long, L. Cronin, *Nat Chem* **2010**, *2*, 308-312.
[17] A. Dolbecq, E. Dumas, C. R. Mayer, P. Mialane, *Chem. Rev.* **2010**, *110*, 6009-6048.
[18] S. Bareyt, S. Piligkos, B. Hasenknopf, P. Gouzerh, E. Lacôte, S. Thorimbert, M. Malacria, *J. Am. Chem. Soc.* **2005**, *127*, 6788-6794.
[19] C. Sanchez, F. Ribot, *New J. Chem.* **1994**, *18*, 1007-1047.
[20] A. Müller, E. Krickemeyer, H. Bögge, M. Schmidtmann, F. Peters, *Angew. Chem. Int. Ed.* **1998**, *37*, 3359-3363.

[21] A. Müller, S. K. Das, V. P. Fedin, E. Krickemeyer, C. Beugholt, H. Bögge, M. Schmidtmann, B. Hauptfleisch, *Z. Anorg. Allg. Chem.* **1999**, *625*, 1187-1192.

[22] P. Yin, D. Li, T. Liu, *Chem. Soc. Rev.* **2012**, *41*, 7368-7383.

[23] H. Wang, S. Hamanaka, Y. Nishimoto, S. Irle, T. Yokoyama, H. Yoshikawa, K. Awaga, *J. Am. Chem. Soc.* **2012**, *134*, 4918-4924.

[24] A. Proust, B. Matt, R. Villanneau, G. Guillemot, P. Gouzerh, G. Izzet, *Chem. Soc. Rev.* **2012**, *41*, 7605-7622.

[25] R. J. Errington, S. S. Petkar, B. R. Horrocks, A. Houlton, L. H. Lie, S. N. Patole, *Angew. Chem. Int. Ed.* **2005**, *44*, 1254-1257.

[26] R. A. Pierotti, *Chem. Rev.* **1976**, *76*, 717-726.

[27] (a) B. Keita, L. Nadjo, *J. Electroanal. Chem.* **1985**, *191*, 441-448; (b) B. Keita, L. Nadjo, *J. Electroanal. Chem.* **1988**, *243*, 87-103; (c) B. Keita, L. Nadjo, *J. Electroanal. Chem.* **1988**, *247*, 157-172; (d) B. Keita, L. Nadjo, J. M. Saveant, *J. Electroanal. Chem.* **1988**, *243*, 105-116.

[28] M. Sadakane, E. Steckhan, *Chem. Rev.* **1998**, *98*, 219-238.

[29] Y. Nagaoka, S. Shiratori, Y. Einaga, *Chem. Mater.* **2008**, *20*, 4004-4010.

[30] D. Schaming, R. Farha, H. Xu, M. Goldmann, L. Ruhlmann, *Langmuir* **2010**, *27*, 132-143.

[31] (a) D. G. Kurth, P. Lehmann, D. Volkmer, A. Muller, D. Schwahn, *J. Chem. Soc., Dalton Trans.* **2000**, *0*, 3989-3998; (b) M. Clemente-León, E. Coronado, C. J. Gómez-García, C. Mingotaud, S. Ravaine, G. Romualdo-Torres, P. Delhaès, *Chem. Eur. J.* **2005**, *11*, 3979-3987; (c) J. J. Giner-Casares, G. Brezesinski, H. Möhwald, S. Landsmann, S. Polarz, *J. Phys. Chem. Lett.* **2012**, *3*, 322-326.

[32] (a) S. Li, X. Yu, G. Zhang, Y. Ma, J. Yao, P. de Oliveira, *Carbon* **2011**, *49*, 1906-1911; (b) J. R. Ferrell Iii, M.-C. Kuo, J. A. Turner, A. M. Herring, *Electrochim. Acta* **2008**, *53*, 4927-4933.

[33] F. M. Toma, A. Sartorel, M. Iurlo, M. Carraro, P. Parisse, C. Maccato, S. Rapino, B. R. Gonzalez, H. Amenitsch, T. Da Ros, L. Casalis, A. Goldoni, M. Marcaccio, G. Scorrano, G. Scoles, F. Paolucci, M. Prato, M. Bonchio, *Nature Chem.* **2010**, *2*, 826-831.

[34] (a) N. Kawasaki, H. Wang, R. Nakanishi, S. Hamanaka, R. Kitaura, H. Shinohara, T. Yokoyama, H. Yoshikawa, K. Awaga, *Angew. Chem., Int. Ed.* **2011**, *50*, 3471-3474; (b) D. Pan, J. Chen, W. Tao, L. Nie, S. Yao, *Langmuir* **2006**, *22*, 5872-5876.

[35] (a) C. Ritchie, A. Ferguson, H. Nojiri, H. N. Miras, Y.-F. Song, D.-L. Long, E. Burkholder, M. Murrie, P. Kögerler, E. K. Brechin, L. Cronin, *Angew. Chem., Int. Ed.* **2008**, *47*, 5609-5612; (b) A. Giusti, G. Charron, S. Mazerat, J.-D. Compain, P. Mialane, A. Dolbecq, E. Rivière, W. Wernsdorfer, R. Ngo Biboum, B. Keita, L. Nadjo, A. Filoramo, J.-P. Bourgoin, T. Mallah, *Angew. Chem. Int. Ed.* **2009**, *48*, 4949-4952.

[36] C. Fleming, D.-L. Long, N. McMillan, J. Johnston, N. Bovet, V. Dhanak, N. Gadegaard, P. Kogerler, L. Cronin, M. Kadodwala, *Nat. Nanotechnol.* **2008**, *3*, 289-233.

[37] (a) B. Keita, L. Nadjo, *Surf. Sci. Lett.* **1991**, *254*, L443-L447; (b) S. Dong, B. Wang, *Electrochim. Acta* **1992**, *37*, 11-16; (c) B. A. Watson, M. A. Barteau, L. Haggerty, A. M. Lenhoff, R. S. Weber, *Langmuir* **1992**, *8*, 1145-1148; (d) B. Keita, L. Nadjo, *J. Electroanal. Chem.* **1993**, *354*, 295-304; (e) S. Liu, Z. Tang, Z. Shi, L. Niu, E. Wang, S.

Dong, *Langmuir* **1999**, *15*, 7268-7275; (f) L. Cheng, S. Dong, *J. Electrochem. Soc.* **2000**, *147*, 606-612; (g) J.-P. Tessonnier, S. Goubert-Renaudin, S. Alia, Y. Yan, M. A. Barteau, *Langmuir* **2013**, *29*, 393-402.

[38] (a) M. H. Ge, B. X. Zhong, W. G. Klemperer, A. A. Gewirth, *J. Am. Chem. Soc.* **1996**, *118*, 5812-5813; (b) M. H. Ge, A. A. Gewirth, W. G. Klemperer, C. G. Wall, *Pure Appl. Chem.* **1997**, *69*, 2175-2178; (c) L. Lee, J. X. Wang, R. R. Adžić, I. K. Robinson, A. A. Gewirth, *J. Am. Chem. Soc.* **2001**, *123*, 8838-8843.

[39] C. M. Teague, X. Li, M. E. Biggin, L. Lee, J. Kim, A. A. Gewirth, *J. Phys. Chem. B* **2004**, *108*, 1974-1985.

[40] A. Kraynov, T. E. Müller, in *Applications of Ionic Liquids in Science and Technology* (Ed.: P. S. Handy), InTech, **2011**.

[41] Y. Wang, O. Zeiri, V. Gitis, A. Neyman, I. A. Weinstock, *Inorg. Chim. Acta* **2010**, *363*, 4416-4420.

[42] (a) A. Neyman, L. Meshi, L. Zeiri, I. A. Weinstock, *J. Am. Chem. Soc.* **2008**, *130*, 16480-16481; (b) Y. Wang, A. Neyman, E. Arkhangelsky, V. Gitis, L. Meshi, I. A. Weinstock, *J. Am. Chem. Soc.* **2009**, *131*, 17412-17422; (c) Y. Wang, I. A. Weinstock, *Dalton Trans.* **2010**, *39*, 6143-6152; (d) S. Sharet, E. Sandars, Y. Wang, O. Zeiri, A. Neyman, L. Meshi, I. A. Weinstock, *Dalton Trans.* **2012**, *41*, 9849-9851; (e) Y. Wang, I. A. Weinstock, *Chem. Soc. Rev.* **2012**, *41*, 7479-7496; (f) Y. Wang, O. Zeiri, S. Sharet, I. A. Weinstock, *Inorg. Chem.* **2012**, *51*, 7436-7438.

[43] H. Taketa, S. Katsuki, K. Eguchi, T. Seiyama, N. Yamazoe, *J. Phys. Chem.* **1986**, *90*, 2959-2962.

[44] X. Lopez, J. J. Carbo, C. Bo, J. M. Poblet, *Chem. Soc. Rev.* **2012**, *41*, 7537-7571.

[45] (a) F. Leroy, P. Miro, J. M. Poblet, C. Bo, J. B. Avalos, *J. Phys. Chem. B* **2008**, *112*, 8591-8599; (b) A. Chaumont, G. Wipff, *Phys. Chem. Chem. Phys.* **2008**, *10*, 6940-6953; (c) A. Chaumont, G. Wipff, *C. R. Chim.* **2012**, *15*, 107-117; (d) A. Chaumont, G. Wipff, *Eur. J. Inorg. Chem.* **2013**, *2013*, 1835-1853.

[46] X. Lopez, C. Nieto-Draghi, C. Bo, J. B. Avalos, J. M. Poblet, *J. Phys. Chem. A* **2005**, *109*, 1216-1222.

[47] T. Mitra, P. Miro, A. R. Tomsa, A. Merca, H. Bogge, J. B. Avalos, J. M. Poblet, C. Bo, A. Muller, *Chem.--Eur. J.* **2009**, *15*, 1844-1852.

[48] A. Chaumont, G. Wipff, *J. Phys. Chem. C* **2009**, *113*, 18233-18243.

[49] (a) G. Pacchioni, F. Illas, M. R. Philpott, P. S. Bagus, *J. Chem. Phys.* **1991**, *95*, 4678-4684; (b) A. Berná, A. Rodes, J. M. Feliu, F. Illas, A. Gil, A. Clotet, J. M. Ricart, *J. Phys. Chem. B* **2004**, *108*, 17928-17939.

[50] M. I. Borzenko, R. R. Nazmutdinov, D. V. Glukhov, G. A. Tsirlina, M. Probst, *Chem. Phys.* **2005**, *319*, 200-209.

[51] E. Grinenval, X. Rozanska, A. Baudouin, E. Berrier, F. o. Delbecq, P. Sautet, J.-M. Basset, F. d. r. Lefebvre, *J. Phys. Chem. C* **2010**, *114*, 19024-19034.

[52] X. Rozanska, P. Sautet, F. Delbecq, F. Lefebvre, S. Borshch, H. Chermette, J.-M. Basset, E. Grinenval, *Phys. Chem. Chem. Phys.* **2011**, *13*, 15955-15959.

[53] S. Wen, W. Guan, J. Wang, Z. Lang, L. Yan, Z. Su, *Dalton Trans.* **2012**, *41*, 4602-4607.

Chapter 2
Computational details and models

This chapter introduces the basis of both the computational approaches and the models used in this thesis. Based on the experimental data reported for the adsorption of $[\alpha\text{-}SiW_{12}O_{40}]^{4-}$ on silver surfaces, we present the different models we used for the modelling of these systems. This modelling required the combination of Periodic – Density Functional Theory with Classical Molecular Dynamics in order to introduce solvent effects. All the specific information about the calculations is also presented in this chapter.

UNIVERSITAT ROVIRA I VIRGILI
COMPUTATIONAL MODELLING OF POLYOXOMETALATES ADSORBED ON METALLIC SURFACES
Xavier Aparicio Anglès
Dipòsit Legal: T. 1525-2013

All the programs and packages used in this thesis are based on Quantum Mechanics and Classical Mechanics. However, this chapter does not intend to be a compilation of equations and unreadable statements about the theory that lies behind the programs.

2.1. Vienna Ab initio Simulation Package

The Vienna Ab initio simulation package (*VASP*) is a program for modelling atomic scale materials using the Density Functional Theory (DFT) and/or the Hartree – Fock approximation.[1] VASP was developed by Prof. Dr. Jürgen Hafner, Prof. Dr. Georg Kresse, Dr. Doris Vogtenhuber and Dr. Martijn Marsman, and is a powerful tool in the field of material science.

This package works with periodicity in the three dimensions of space, which allows the user to calculate bulk materials, surfaces and single molecules. The periodicity involves that the basis set must be also periodic. In this case, VASP uses plane-waves, which instead of being localized on an atom, are delocalized in the cell, preserving the symmetry of the cell.

VASP permits work with LDA, GGA, Meta-GGA and Hybrid functional, depending on the version used. It is also possible to introduce Grimme dispersion, one site Coulomb interaction and external fields in the calculations, among other implementations. In our specific case, we used VASP based on DFT for geometric and electronic optimization, determining the Density of States, workfunction and vibrational frequencies. Finally, we also computed Bader AIM charges and infrared intensities from the VASP results, using external codes.

2.1.1. Basic Computational Details

The vast majority of the calculations performed throughout this thesis with VASP used the same computational parameters, with few exceptions.

The Exchange Correlation Functional (E_{xc}) used is the Perdew-Wang 91, based on the Generalized Gradient Approximation (GGA).[2] This functional, which is strictly *ab-initio*, describes the chemical bonds rather well. Several tests were performed in order to evaluate whether this functional was appropriate for this study, and

these were mainly related to the structural and electronic properties of the polyoxometalates, as explained in section 2.3.

In order to ensure a good description of the electronic structure and thus the energy of the system, we set the kinetic energy cut-off for the plane waves basis set to 500 eV in all cases. This cut-off is higher than really necessary, to ensure that all interactions are considered.

Plane waves are mathematically described in both the real and the reciprocal space. For a good description of the system, it is therefore necessary to determine where in the reciprocal space the energy is evaluated. These points are the so-called k-points, and the Monkhorst-Pack scheme is used to determine them.[3] We evaluated three different schemes, 5x5x1 and 3x3x1 and concluded that the 3x3x1 Monkhorst-Pack scheme is sufficient for studying our system. Due to the size of the systems, the 1x1x1 scheme is also used in some systems. The preliminary results for evaluating the number of k-points are mentioned in Appendix 2.1 of this chapter.

Table 2.1 List of all the PAW pseudopotentials used with the explicit valence electrons.

Pseudopotential	Explicit valence electrons
H	$1s^1$
O	$[He]2s^2 2p^4$
Al	$[Ne]3s^2 3p^1$
Si	$[Ne]3s^2 3p^2$
P	$[Ne]3s^2 3p^3$
K	$[Ar]3p^6 4s^1$
Mo	$[Kr]5d^4 6s^2$
Ag	$[Kr]4d^{10} 5s^1$
Cs	$[Xe]5s^2 5p^6 6s^1$
W	$[Xe]5d^4 6s^2$
W_pv	$[Xe]5p^6 5d^4 6s^2$
Au	$[Xe]5d^{10} 6s^1$

The partial occupancies are described using a Gaussian smearing for isolated molecules, and the width of this smearing is set to 0.05 eV.[4] For adsorbed

molecules, the partial occupancies are described using the method of Methfessel-Paxton order 2,[5] with a width of 0.2 eV. This width is related to the entropic contribution to the energy, and it cannot be higher than 10^{-3} eV/atom. In those cases where the entropic term was higher, we reduced the bandwidth to 0.1 eV.

In order to reduce the huge number of plane waves, VASP provides different types of pseudopotentials (PPs). In this study, the PPs chosen are the Projector Augmented Wave (PAW) PPs.[6] These PPs have proven high quality results in solid-state chemistry, despite being more demanding in terms of time than other PPs. Table 2.1 shows all the PAW PPs used, with the explicit valence electrons.

2.1.2. Geometry and electronic optimization

For the optimization of the electronic part, we combined two different algorithms: the Blocked Davidson Iteration Scheme (DAV)[7] and the Residual Minimization Scheme, Direct Inversion in the Iterative Subspace (RMS-DIIS).[8] The main difference is the robustness of each one. DAV algorithm is more robust and time demanding than the RMS-DIIS, but it ensures the convergence of the electronic structure in almost all cases. On the other hand, RMS-DIIS is a faster algorithm that generally works rather well, but requires a good initial guess. We used a combination of both methodologies in almost all calculations, starting with five SCF cycles using the DAV algorithm, followed by the required cycles using the RMS-DIIS scheme. If the electronic structure is hard to converge, only the DAV algorithm is used. Electronic optimization is performed regardless until self-consistence, with a convergence criterion of $1 \cdot 10^{-5}$ eV or $1 \cdot 10^{-6}$ eV for specific cases.

The ionic optimization is performed using a conjugate-gradient algorithm (CGA).[9] The algorithm works in three different steps: (i) the program calculates the forces for a given configuration; (ii) VASP generates a trial step and (iii) the code checks the new forces based on the new configuration. If the forces of the new configuration have a strong parallel component in the direction of the steepest descent, the next trial is performed. VASP also allows work with other algorithms but the CGA is the most robust. The convergence criterion for the ionic part is set to 0.02 eV·Å^{-1}.

2.1.3. Vibrational frequencies and IR intensities

There are two main goals when computing vibrational frequencies. First, to confirm that the structure optimized is a true minima in the Potential Energy Surface and second, to compute the infrared (IR) spectrum. When calculating vibrational frequencies, the electronic structure of the system to be studied must be very accurate. To that end, in all frequency calculations the electronic structure of the system is recalculated (as well as the whole structure) with an electronic convergence criterion of $1 \cdot 10^{-6}$ eV.

From the analytical gradients, VASP computes numerical Hessian, obtained by displacing each atomic Cartesian coordinate ± 0.02 Å. After weighting the Hessian matrix for mass and diagonalising the matrix, VASP obtains the frequencies and the Vibrational Normal Modes (VNM), which are all enclosed in the harmonic approach.

The intensities of the infrared spectra are obtained using the external IRIAN code.[10] Based on the (x,y,z) components of the dipolar moment at each displacement, IRIAN calculates the derivatives of the dipolar moments compared to the displacement and thus the intensities associated with the IR fundamental bands. Only the z-component derivatives of the dipolar moment are required for adsorbed species.

2.1.4. Bader's Atoms in Molecules Charges

Bader's theory states that the different atomic regions are separated by a zero flow density surface.[11] It is possible to determine the atomic charges by integrating these regions. In order to reduce the computational costs, Henkelman and co-workers developed an algorithm that allows work on a charge density grid.[12] On one hand, Bader AIM charges are known to give a rather ionic description of the system, so charges will be overestimated. On the other hand, each analysis based on this theory should be considered only when the system is fully relaxed, *i.e.* when the system is found in one minimum of the PES.

2.1.5. Density of States

In order to understand chemical bonds and interaction between molecules, the electronic structure of the whole system must be analysed. In general, this analysis focuses on studying the molecular orbital (MO) diagrams, but this is not the case with periodic materials. When the number of atoms increases in a system, orbitals get closer in energy. When these energy levels are close enough, bands rather than discrete levels are considered. To describe these bands, we must specify where in the reciprocal space we are evaluating them (remembering the mathematical description of the plane waves). The electronic structure is therefore determined at different k-point and need not be equal in each of them. The electronic structure is represented by the Band Diagram or Band structure. (See Figure 2.1)

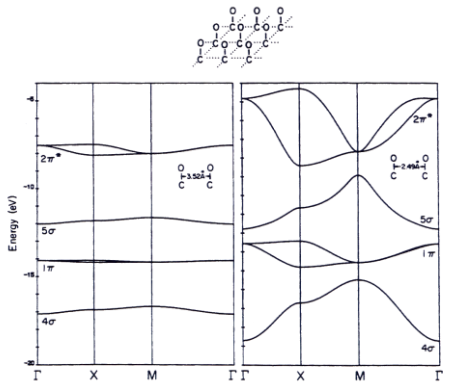

Figure 2.1 Example of band structure of square monolayers of CO at two separations: 3.52 Å (left) and 2.49 Å (right). This image is taken with permision from the book *"Solids and Surfaces: A chemist's view of bonding in extended surfaces"*, by Roald Hoffmann, page 24.[13]

Band structure is extremely rich in information, which means that it is a diagram very difficult to understand. One way to simplify the information it reports is to obtain the Density of States (DOS). The DOS is obtained by integrating the total number of states (considering all k-points) between infinitesimal energy differences, all of which are divided by the volume cell.

In both band structure and DOS, the Fermi level (E_F) is the highest occupied level of the system. It is worth mentioning that this statement is strictly true when talking

about conductor materials. For semiconductors or insulators, E_F would be found between the occupied and the unoccupied states. The intensity of the bands is directly related to the number of states found in a specific energy. However, DOS does not distinguish between different contributions of each atomic species. Projecting DOS into the spherical harmonic orbitals of each atom can solve this issue. We then talk about the Projected Density of States (PDOS). In both DOS and PDOS, energy is represented with respect to E_F ($E-E_F$, usually in eV) against the Density of States or the PDOS (in states·eV^{-1}).

2.1.6. Local Potential and Work function

The work function (ϕ) is defined as the minimum energy required to move an electron from the E_F to the vacuum. This value is equivalent to the first ionization potential in molecules, and it is a characteristic property of the material. VASP does not compute it directly, so it is necessary to first evaluate the local potential (V) along z-axis. The local potential is the potential energy that one electron has in a specific point. When this value remains stable in a specific region of the space, this indicates that this region belongs to the vacuum. The work function is thus calculated from the difference between the potential energy of the electron in the vacuum region and the E_F .

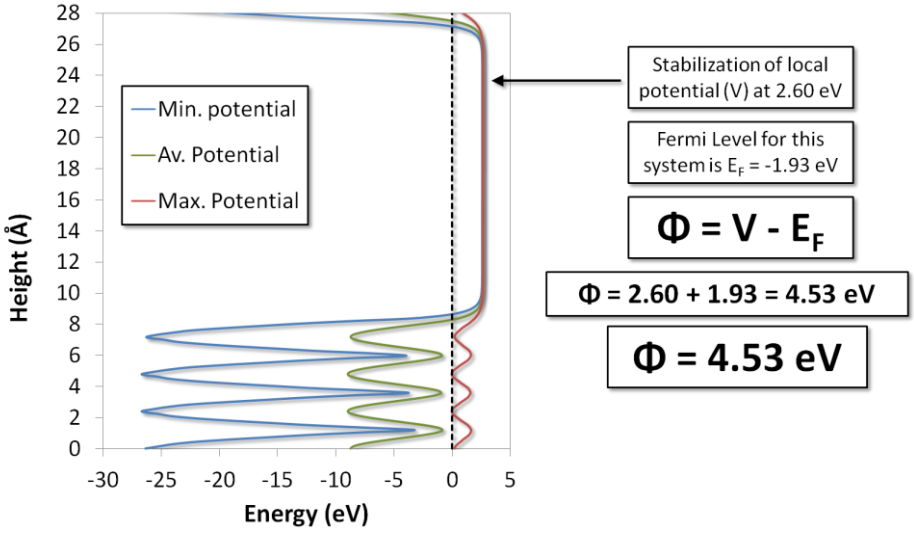

Figure 2.2 Representation of V for Ag(100) and how to compute Φ.

2.2. Modelling POMS on surfaces

Based on the few systematic studies of the adsorption of the α-Keggin polyoxometalate on silver surface, we built a model for the computational study of these systems. In this section, we present the different POMs used, as well as the surfaces that were used in this thesis.

2.2.1. The Polyoxometalate

The polyoxometalate studied in this thesis is the α-Keggin anion; $[XM_{12}O_{40}]^{n-}$, with M = W^{6+} and Mo^{6+} and X = Al^{3+}, Si^{4+} and P^{5+}. Metals (M) and heteroatoms (X) are fully oxidized whereas oxygen atoms are fully reduced. The formal charge of these compounds is therefore negative: $[PMo_{12}O_{40}]^{3-}$ (PMo), $[SiMo_{12}O_{40}]^{4-}$ (SiMo), $[PW_{12}O_{40}]^{3-}$ (PW), $[SiW_{12}O_{40}]^{4-}$ (SiW), and $[AlW_{12}O_{40}]^{5-}$ (AlW).

The symmetry of the α-Keggin anion is T_d, which means that all the metal atoms are equivalent and there are only four different oxygen atoms: the internal oxo ligand (O_a), two different bridging oxo ligands (O_b and O_c) and the terminal oxo ligand (O_d), as shown in Figure 2.3 a). This figure also shows two POM symmetry elements: the C_3 proper axis (Figure 2.3 b)) and the S_4 improper axis (Figure 2.3 c)). Although there are more symmetry elements, both are highlighted because they are used for labeling the different ways the α-Keggin has for adsorbing on surfaces.

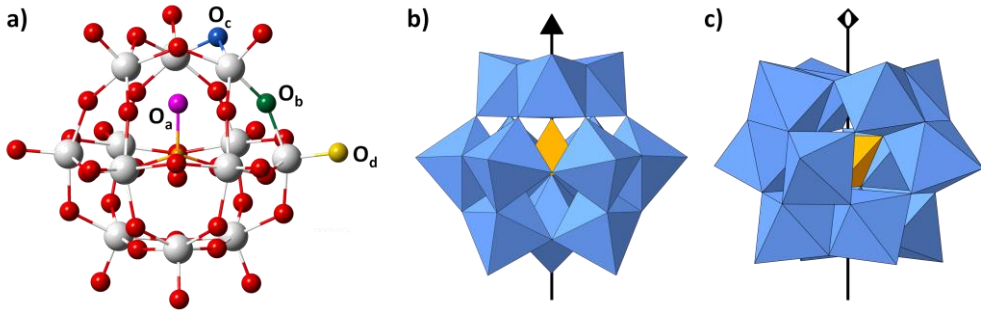

Figure 2.3 a) Ball-and-stick representation for a generic α-Keggin anion with label definitions for oxygens; b) representation of the C_3 improper axis in the α-Keggin anion and c) representation of the S_4 proper axis in the α-Keggin anion.

α-Keggin anions have a simple electronic structure. They can be treated as closed-shell structures in which the occupied orbitals are delocalized over the oxo ligands, whereas the d-metal orbitals describe the unoccupied orbitals. Because of this good separation between the oxo orbitals and the metal orbitals, they are described as "bands" although they are formally not.[14]

We first evaluated whether the PW91 exchange correlation potential is adequate for describing their geometric and electronic structure. Taking the polyoxotungstates as a test group (AlW, SiW and PW) we compared the results obtained with previous published results by Maestre *et al*. in 2001, as well as crystallographic data.[14-15] POMs were calculated as anions in the gas phase, placed in the center of a 20x20x20 Å cubic box. This cell is large enough to avoid interactions between the replications in all directions of the space.

Table 2.2 Comparison of theoretical and X-ray (averaged values) distances (in Å) for different polyoxotungstates. ADF values were computed using BP86 as exchange – correlation functional and TZP basis set.

		AlW	SiW	PW
d(X-O_a)	*Exp*	1.74	1.65	1.52
	ADF	1.74	1.64	1.53
	VASP	1.76	1.64	1.55
d(W-O_a)	*Exp*	2.26	2.34	2.44
	ADF	2.26	2.33	2.35
	VASP	2.30	2.39	2.48
d(W-O_b)	*Exp*	1.91	1.91	1.90
	ADF	1.96	1.94	1.94
	VASP	1.95	1.94	1.94
d(W-O_c)	*Exp*	1.93	1.92	1.90
	ADF	1.93	1.92	1.93
	VASP	1.94	1.93	1.93
d(W-O_d)	*Exp*	1.72	1.70	1.69
	ADF	1.76	1.74	1.73
	VASP	1.75	1.74	1.73

The structural analysis shown in Table 2.2, does not reflect significant differences between other methodologies tested in the group (specifically, using the Amsterdam Density Functional package with BP86 and TZP basis set) nor with the crystallographic data. The most noticeable differences are the distance bond between metal atoms (W) and the internal oxygens (O_a) when compared with the experimental data, but they are only about 0.05 Å in SiW.

Finally, the DOS and PDOS also confirm that calculations performed with VASP reproduce the HOMO-LUMO Gap, such as the separation between the oxo band and the metal band, as shown in Figure 2.4.

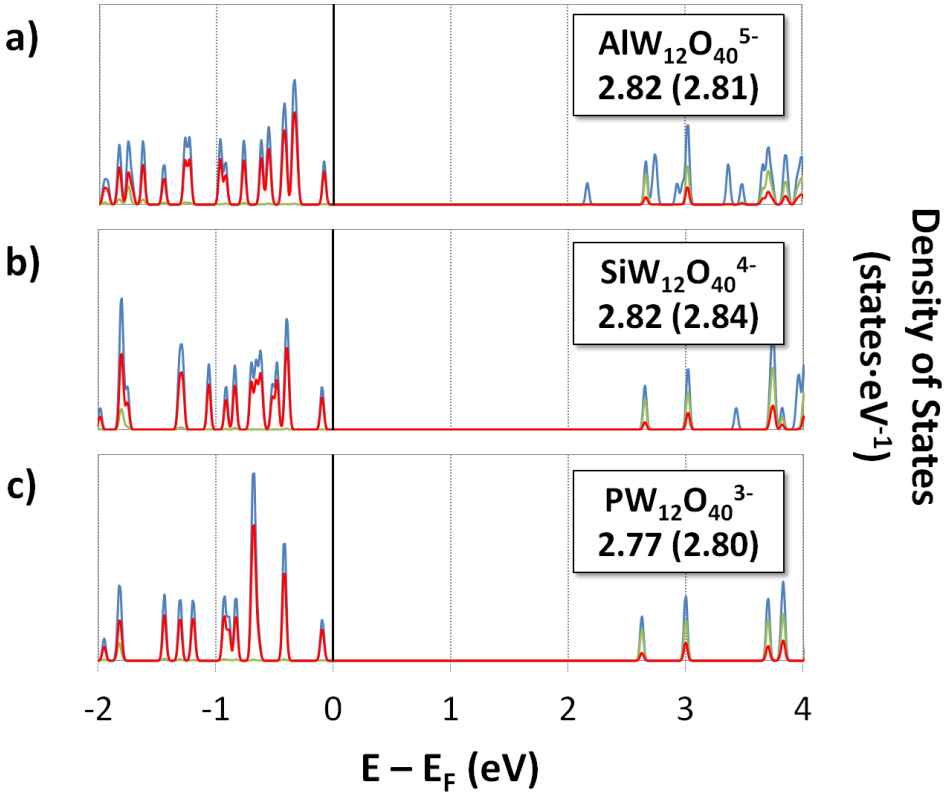

Figure 2.4 Densities of States and Projected Density of States for a) $[AlW_{12}O_{40}]^{5-}$; b) $[SiW_{12}O_{40}]^{4-}$ and c) $[PW_{12}O_{40}]^{3-}$. The straight blue line represents the total Density of States, the red straight line represents the PDOS onto the p orbitals of all oxygen atoms and the green straight line belongs to the PDOS of W(d) orbitals. HOMO – LUMO gaps are expressed in eV for both VASP results and ADF (BP86/TZP) results, in parentheses.

2.2.2. Slab Model

The simulation of surfaces can take place using two different models: the cluster and the slab model. VASP works with periodic boundary conditions (PBC), meaning that using the slab model is direct and straightforward. This model is based on the replication of the unit cell along all space directions. Since the object to model is a surface, it is important to avoid interactions resulting from the replication along Z-axis (by convention). As a result, a vacuum region large enough is introduced along the Z-axis to ensure no interactions with the surface and its replication.

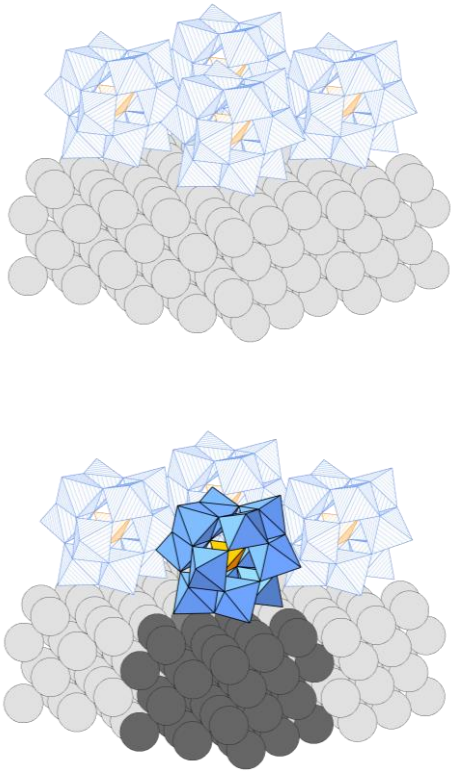

Figure 2.5 Representation of the slab model in a 2x2x2 representation compared to the original cell. In the original cell, metal atoms are colored in dark grey, and polyoxometalate polyhedrons in blue (addenda atom) and yellow (heteroatom). Replications of the original cell are colored with surface atoms in light gray and POM polyhedrons are striped using the aforementioned colors. The distance between the replication in the z-axis represents the vacuum layers left in order not to interact with the replications in this direction.

2.2.3. Surface and adsorption models

The metal surfaces considered in this thesis are silver and gold surfaces. Both are metallic atoms from the d-block of the periodic table in the Ib group. They present a face-centred cubic cell (fcc), with all crystallographic directions equivalent, and present one atom in each vertex and one atom in the centre of all faces. The length of the cell is found at a point on the potential energy surface where the attractive and repulsive forces are balanced.

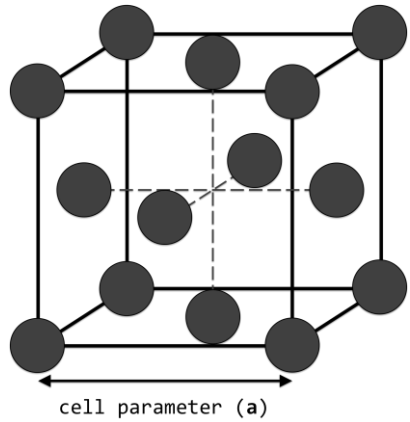

Figure 2.6 Representation of the face centered cubic cell with atoms at all vertices and at the center of all faces.

In computation, these forces are determined by the exchange – correlation potential, and as such prior evaluation of the cell parameter is needed. Although PW91 describes the adsorbate rather well, for Ag and Au bulk it gives slightly larger cell parameters compared to the experimental, as shown in Table 2.3.

Table 2.3 Experimental (a_{exp}) and optimized cell parameter (a_{opt}) in Å for silver and gold metals.

Metal	a_{exp}[16]	a_{opt}
Ag	4.09	4.16
Au	4.07	4.17

Several unit cells are used in the thesis. Here they are all presented starting for those based on experimental structural data, followed by those not based on structural data.

- *High coverage*

In the late 1990s, the group led by Walter G. Kemplerer and Andrew A. Gewirth reported structural information about the adsorption of α-$H_4SiW_{12}O_{40}$ (HSiW) on silver surfaces. In 1996 and in 2001, this group published STM images regarding the self-assembly of $[\alpha\text{-}SiW_{12}O_{40}]^{4-}$ (SiW) on Ag(111) and on Ag(100).[17] Those superstructures are also assumed for respective gold surfaces.

(111) fcc surface

In 1996 M. Ge *et al.* proposed a unit cell for the adsorption of α-$H_4SiW_{12}O_{40}$ on Ag(111) surface. Based on STM images, they set the distance between adsorbates at 10.2 ± 0.5 Å, proposing the almost square $\begin{pmatrix} 4 & 1 \\ 1 & 4 \end{pmatrix}$ Ag(111) as the unit cell (see Appendix 2.2 for further information about the matrix and Wood's notation). In this unit cell, $|\overrightarrow{a_2}| = |\overrightarrow{b_2}| = \sqrt{13} \cdot |\overrightarrow{a_1}|$, with 10.58 Å for silver and 10.76 Å for gold. The value of α_2, defined by vectors $\overrightarrow{a_2}$ and $\overrightarrow{b_2}$ is 92.9°. Since this angle does not match the angle defined by $\overrightarrow{a_1}$ and $\overrightarrow{b_1}$ (120°), Wood's notation cannot be used. A representation for the unit cell is shown in Figure 2.7 a).

This unit cell is the minimum surface cell able to allow the adsorption of a α-Keggin anion, so it involves the highest coverage (θ) possible for Ag(111). This coverage is defined as the number of adsorbates per atoms per unit cell. Hence, considering that there are 15 metal atoms per layer, the maximum coverage for this surface is θ = 1/15 = 0.07.

To determine the adsorption geometry of the α-Keggin anion on the surface, it is necessary to provide:

- The adsorption mode of the polyoxometalate, defined by the POM symmetry axis perpendicular to the surface.
- The active site in which POM is adsorbed.
- The relative orientation of the POM with regard to the surface.

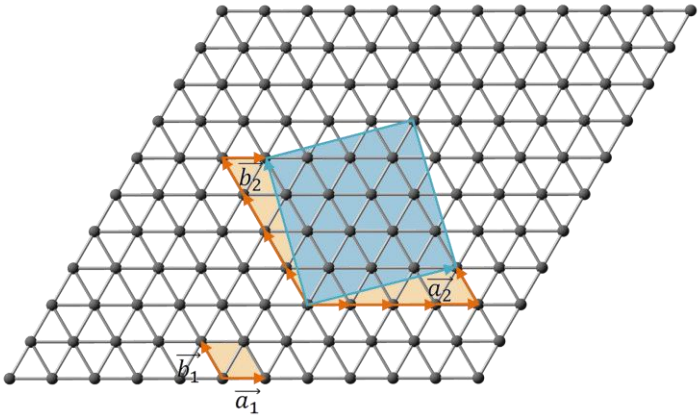

Figure 2.7 Representation of the proposed unit cell for Ag(111) for the highest coverage situation.

For this unit cell, the POM can only be adsorbed *via* its S_4 symmetry axis because *via* its C_3, the POM does not fit into the unit cell. On the surface, the POM can be adsorbed in four different active sites: on top (T), bridge (B), hollow fcc (fcc) and hollow hcp (hcp), all of which are shown in Figure 2.8 a). A. A. Gewirth proposed the definition of the adsorption site considering the relative position of the heteroatom with regard to the surface.[18] Interestingly, although the POM is adsorbed in one specific site, this does not mean that the interactions between POM and surface occur *via* this site. In fact, POM can be considered as a μ_4-bridging ligand, where the four terminal oxygens are interacting with the surface (not considering the bridging oxygens). By way of an example, when a POM is adsorbed on bridge, terminal oxygens are on top of silver atoms.

Finally, due to the symmetry of the surface, different rotations of the POM for a given active site are also considered. POM rotations or orientations on the surface are labeled by the orientation angle (α), which is the angle between the crystallographic [110] direction (which matches the direction defined by the metal – metal distance) and the direction defined by the two O_b, colored in cyan in Figure 2.8, furthest from the surface.

The vacuum space for the slab unit cell is 22.89 Å, which is equivalent to 11 metal layers. In order to ensure that with this height the slab does not interact with its replication along z-axis, we computed the local potential along the Z-axis for

obtaining the work function for Ag(111) being Φ_{Comp} = 4.53 eV. Considering that Φ_{Exp} = 4.46 ± 0.02,[19] we prove that the vacuum space is adequate.

We evaluated the number of metal layers necessary for a good description of the adsorption. Hence, we computed the relative energies for $[\alpha\text{-}SiW_{12}O_{40}]^{4-}$ for two different adsorption sites, on-top and on bridge (T and B). A more detailed analysis of the adsorption sites is presented in following chapter. For both systems, we computed the relative energies for two different k-point meshes with a 4 and 6 metal layers slab. The results, presented in Appendix 2.1, show that the metal can be modelled with only four silver layers and with a 3x3x1 k-point mesh.

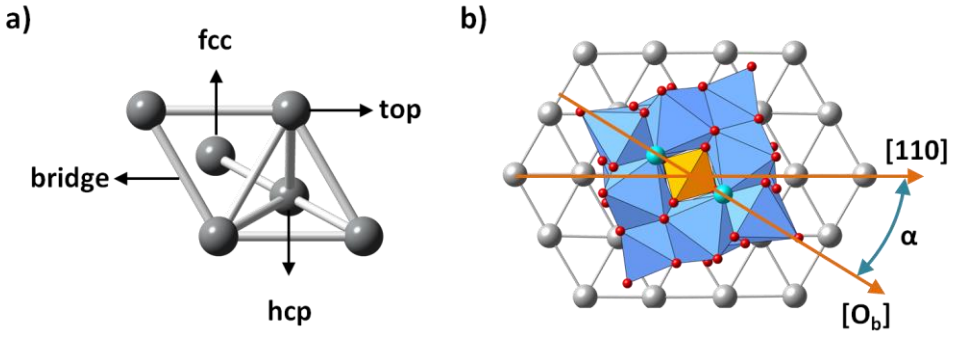

Figure 2.8 a) Representation of the different active sites for (111) fcc surface and b) graphical representation of the orientation angle (α).

To sum up, the way to identify each site is as follows: (i) Specify the adsorption orientation along the free POM's symmetry axis (C_3 and S_4). If only one adsorption orientation is allowed or considered, it is assumed by default and not specified. (ii) Indicate the active site where the POM is adsorbed. (iii) Add the orientation angle as a subindex of the active site. For example, if the POM is adsorbed *via* its S_4 symmetry axis in the hcp site with α = 30°, it will be labeled as S_4-hcp_{30}. If all checked sites are S_4 only hcp_{30} is specified.

(100) fcc surface

In 2001, the group led by A. A. Gewirth proposed a unit cell for the adsorption of α-$H_4SiW_{12}O_{40}$ on Ag(100) based on STM images and X-Ray reflectivity measurements. According to those measurements, they proposed the $\sqrt{13}x\sqrt{13}R33.69^o$ in Wood's notation, or the $\begin{pmatrix} 3 & 2 \\ -2 & 3 \end{pmatrix}$ Ag(100) in matrix notation. Their dimensions are $|\overrightarrow{a_2}| = |\overrightarrow{b_2}| = \sqrt{13} \cdot |\overrightarrow{a_1}| = 10.60$ Å (this unit cell has not been used for gold). The reader will notice that since the Wood's notation is used, the angle defined by $\overrightarrow{a_2}$ and $\overrightarrow{b_2}$ and the angle defined by $\overrightarrow{a_1}$ and $\overrightarrow{b_1}$ is the same, and its value is 90°.

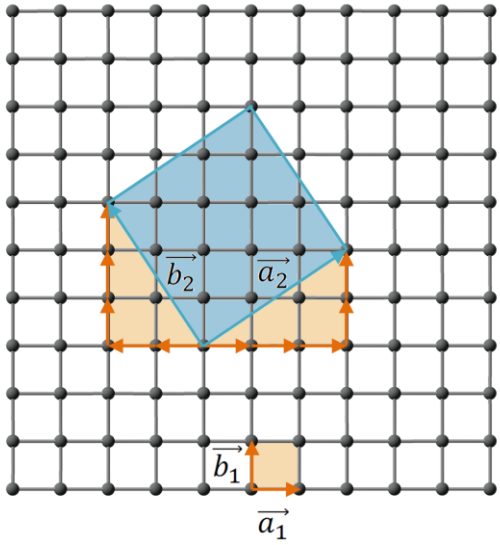

Figure 2.9 Representation of the proposed unit cell for Ag(100) for the highest coverage situation. The primitive unit cell is shown in orange, as well as the area defined for the lattice definition of the a_2 and b_2 vectors. The area of the "superstructure" is shown in blue.

However, the angle defined by $\overrightarrow{a_1}$ and $\overrightarrow{a_2}$ is 33.69°, which is specified in Wood's notation. The coverage for this unit cell is slightly higher than the highest coverage for the (111) surface. There are 13 metal atoms per layer, and the maximum coverage is therefore θ = 1/13 = 0.08.

In this cell, as with the (111) high coverage situation, the adsorption can only take place *via* the POM S_4 symmetry axis. The difference here is the active sites. For (100), only three active sites are considered: on top (T), hollow (H) and bridge (B). The aforementioned indications about the orientation angle are also considered in this case, as shown in Figure 2.10 b).

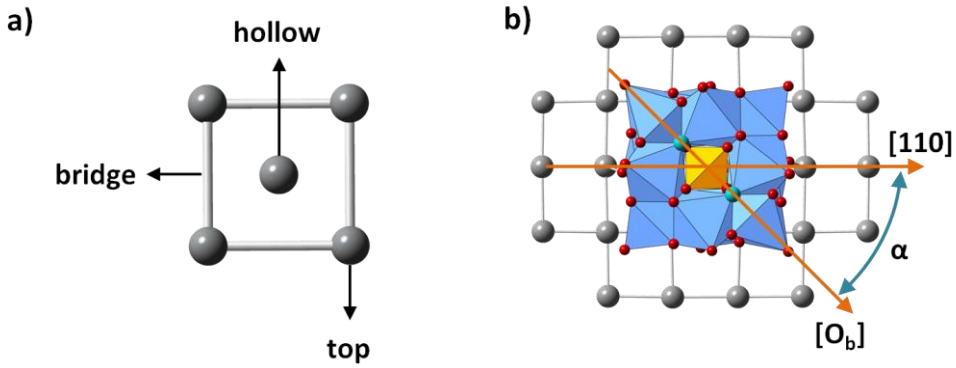

Figure 2.10 a) Representation of the different active sites for the Ag(100) surface and b) Graphical representation of the orientation angle (α).

We also calculated the work function for this cell, obtaining a value of Φ_{Comp} = 4.17 eV. Considering that experimental value Φ_{Exp} = 4.22 ± 0.04 eV, this surface is also well described.[19]

- *Low coverage*

In order to avoid direct interactions with POMs, we propose different superstructures that ensure no close contacts between adsorbates. In the case of the (111) surface, the chosen unit cell is the $\begin{pmatrix} 5 & 0 \\ 3 & 6 \end{pmatrix}$ in the matrix notation. The lengths of this unit cell are $|\overrightarrow{a_2}| = 3\sqrt{5} \cdot |\overrightarrow{a_1}|$ = 14.68 Å and $|\overrightarrow{b_2}| = 4 \cdot |\overrightarrow{a_1}|$ = 15.25 Å and the angle between $\overrightarrow{a_2}$ and $\overrightarrow{b_2}$ is 90° (see Figure 2.7 b). The number of atoms per layer is 30, meaning that the coverage for this superstructure is θ = 1/30 = 0.03. The C_3 orientation mode is allowed in this superstructure.

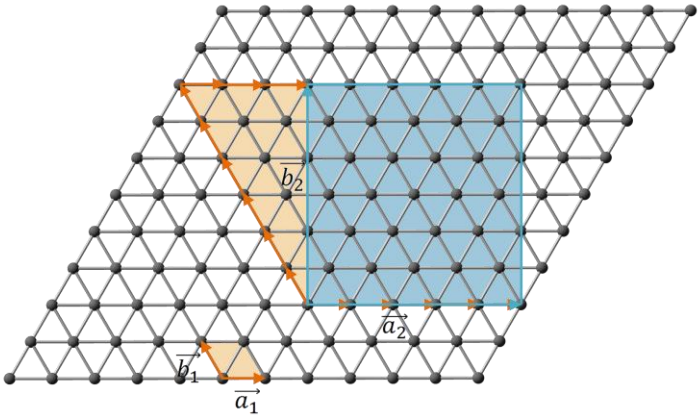

Figure 2.11 Proposed unit cell for Ag(111) in a low coverage situation.

For the (100) surface, the superstructure is the $4\sqrt{2}x4\sqrt{2}R45^o$ in Wood's notation or the $\begin{pmatrix} 4 & 4 \\ -4 & 4 \end{pmatrix}$ in matrix notation. The lengths are $|\overrightarrow{a_2}| = |\overrightarrow{b_2}| = 4\sqrt{2} \cdot |\overrightarrow{a_1}|$ = 16,64 Å and the angle defined by both axes is 90. The intersection between by $\overrightarrow{a_1}$ and $\overrightarrow{a_2}$ defines an angle of 45°. There are 32 atoms per layer in this superstructure, which involves a coverage of θ = 1/32 = 0.03 and the adsorption *via* C_3 is also allowed.

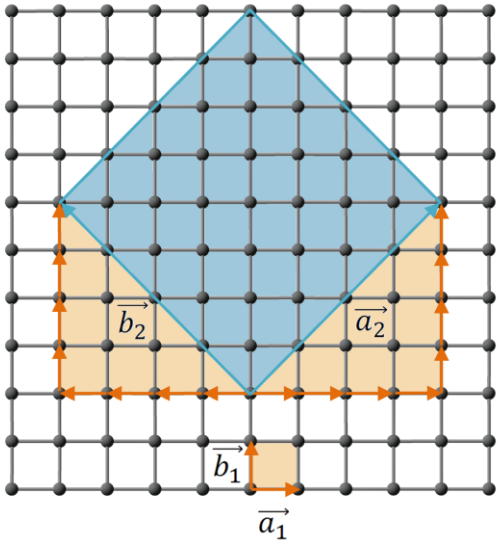

Figure 2.12 Proposed unit cell for Ag(100) in low coverage situation.

2.2.4. Model with counterions

With non-periodic methodologies, ionic species are modeled by simply indicating the charge of the system. In surface modeling, it is usually accepted that ionic species, like alkali metals, with little anions such as hydroxyl or cyanide can be treated as neutral species.[20] Since POMs are anions, the first attempt to model their adsorption on a surface therefore considers them as a neutral species.

However, the electronic structure of the POM is much more complex than a simple alkali metal or a single halogen atom. The charge of the POM is a consequence of the full occupation of the oxo-band, resulting in a large HOMO-LUMO gap between the oxo and metal bands. Logically, the neutral POM becomes a strong oxidant agent that wants to fill the oxo empty orbitals. This strength can overestimate the interaction between POM and surface.

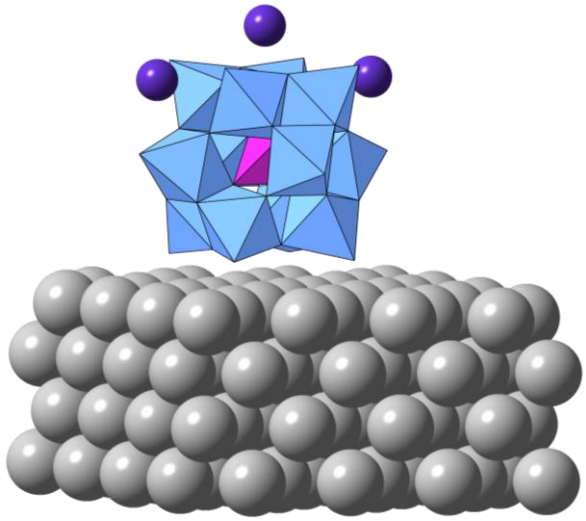

Figure 2.13 Ball-and-stick representation of a generic α-Keggin with counterions adsorbed on a metallic surface.

One way to occupy these orbitals without considering explicit electrons is to use counterions as reducing agents. This model is especially important when the charge of the POM is relatively large, since the corresponding neutral specie is extremely oxidant. Of course, this model has its advantages and disadvantages, which are discussed in further chapters.

2.3. DL_POLY

As the authors state on their website: "*DL_POLY is a classical molecular dynamics simulation package developed at the Daresbury Laboratory by W. Smith, T.R. Forester and I.T. Todorov*".[21] This package allows simulation of various molecular species such as atomic systems, molecules, polymers, macromolecules, metals, alloys or covalent solids. DL_POLY works with a classic force field that includes different features: non-bonded atom-atom potentials, covalent related bonding (typical bond, angles, dihedrals and inversions), Coulombic and Lennard-Jones potentials, and metallic potentials. Finally, DL_POLY also allows work in a box with different periodic boundary conditions for a better accommodation of the system.

2.3.1. Molecular Dynamics in the context of this thesis

Before discussing the specific computational details used, it is worth starting with the main reason for using DL_POLY. POMs are anions, as pointed out above. Their computational study therefore somehow requires consideration of the solvent, especially if we want to reproduce their electronic structure. There are two main strategies for including these effects in our calculations: using a continuum model or explicit solvent molecules. VASP has not implemented the continuum model, so the only way to introduce these effects is by explicit solvent molecules and/or counterions.

The strategy followed to introduce the solvent and counterions is to use molecular dynamic simulations, obtaining a random distribution of water molecules and counterions surrounding the adsorbed POM. After the simulation, we extracted a set of geometries from the trajectories that include the first solvation sphere and the corresponding counterions. From these snapshots, we recalculated the electronic structure using VASP, considering the embedding effects of the solvent and cations. A more in-depth explanation of the entire strategy is given in Chapter 4.

2.4 Modelling POMs on a surface in solution

In order to better understand some of the computational parameters used, it is first necessary to introduce how we set up the system. The first step in performing a molecular dynamics calculation is to set up an initial configuration. In our case, we used the Packmol package, developed at the State University of Campinas, Brazil for this propose.[22] It packs various types of molecules in different regions of the space, allowing different kind of cells to be set up. Although is quite simple to build up the geometry, the chemical sense that the system must have is also important.

Suppose that we have an electrochemical system, with two different electrodes immersed in an aqueous solution with different types of charged electrolytes. Without applying any potential, the different electrolytes will be in contact on the electrode's surface, establishing chemical or physical bonds and generating the so-called surface charge or Inner Helmholtz plane (IHP). Because of electrostatic interactions, electrolytes with opposite charges approach the layer, not directly interacting with it, and are more influenced by thermal motion than being firmly anchored. This second layer is called the diffuse layer or Outer Helmholtz Plane (OHP), and both layers are known as the Electrical Double Layer, or Double Layer for short (See Figure 2.14).

The height of the cell must ensure that the Double Layer can be reproduced. If we consider the high coverage situation, where only one POM is adsorbed in a very narrow unit cell, the required height of the cell would be too much large. We therefore decided to duplicate the unit cell in the high coverage situation because it has a wider box, and the height is twice the width of the box. Because of the duplication, four POMs are considered in the system.

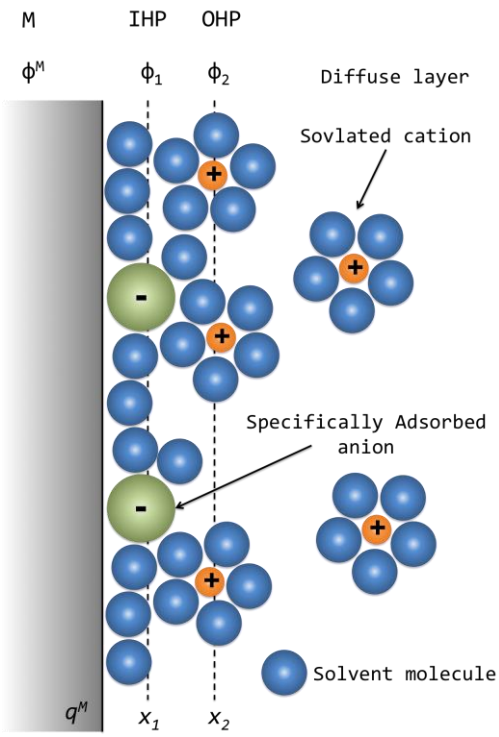

Figure 2.14 Schematic representation of the Electrical Double Layer, assuming that the adsorbed species are anions.[23]

For high coverage situations, the cells we are working with are based on experimental measurements. In the experiments, the counterions for POM were protons, from the acid media. Unfortunately, working with protons and polyoxometalates is not a simple task. Hence, we decided to change from protons to potassium and cesium atoms, assuming that the difference in the Van der Waals radium of alkaline metals would not dramatically affect the results.

Considering these dimensions, we had to calculate the number of water molecules that had to be included in the box for a density of approximately 1 $g \cdot cm^{-3}$. We subtracted the volume of the surface and the volume of the POMs from the overall volume of the cell, assuming that POM was a sphere of radium equal to 5.5 Å. We neglected the volume of the counterions. Finally, 461 water molecules are included to simulate the solvent in the box.

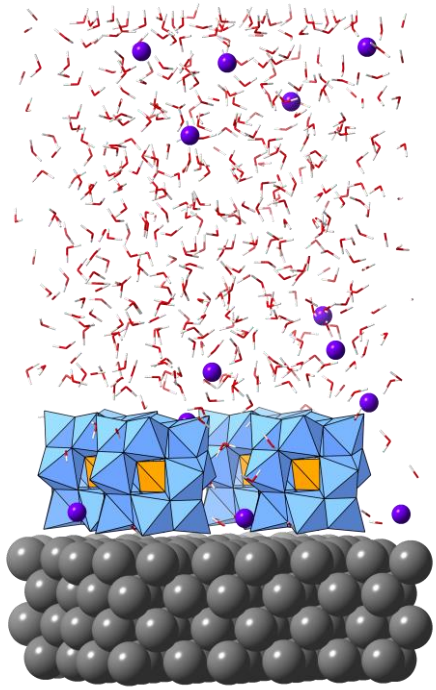

Figure 2.15 Polyhedral and ball-and-stick representation of the model used to perform Molecular Dynamic situations: the surface (grey balls); the polyoxometalates (blue and orange polyhedron); counterions (in violet) and water molecules (red and white sticks). This model is used to perform the MD simulations.

2.3.2. Basic computational details

All calculations were performed using the Canonical Ensemble (NVT ensemble) that keeps the number of species, the volume and the temperature constant. We set the initial pressure to 1 atm and the temperature to 298 degrees K. The average temperature is kept constant throughout the simulation using the Nosé-Hoover thermostat, which readjusts the temperature to 298 K degrees, every 0.01 ps.[24]

DL_POLY works by considering periodic boundary conditions. If a molecule were placed on the edge of the box it would have fewer neighbors than molecules embedded within the box. This would lead to inappropriate macroscopic properties that would distort the overall result. PBC means that if one molecule

leaves the box on one side, it will immediately appear on the opposite site, and the number of molecules remains constant.

In our simulations, surface, POMs, solvent and counterions are not treated in the same way. Both POMs and surface are considered as frozen bodies and thus no specific parameters for the intramolecular potential functions in the force field are required. When modeling water molecules, we selected the TIP3P model, which considers the experimental geometry.[25] Water is treated as a rigid body meaning that is allowed to move freely in the box, but not its bonds. Hence, we also specify no parameter for the intramolecular potential functions.

The intermolecular potential functions include both the electrostatic (long-range terms) and the Van der Waals (short-range) potentials. The charges of the system are computed by means of AIM Bader Charges obtained from VASP calculations. The electrostatic interactions are evaluated using the Ewald Summation.[26] This algorithm works in the real and the reciprocal space to reduce computational costs, and it is known to be one of the best techniques for evaluating these interactions. The Ewald summation is controlled by three different parameters: (i) the convergence parameter α, which controls the accuracy of this term, (ii) the real space cut-off which sets from which we neglect the electrostatic interactions (r_{cut}) and (iii) the largest reciprocal space vector (k_{max}). The r_{cut} is set to 9.25 Å and instead of being directly specified; the other two parameters are obtained by means of another tag, which is the Ewald precision, set to $1 \cdot 10^{-5}$.

The short-range potential describes the Van der Waals (VdW) interactions between the different atom types. We considered the interaction of atomic species pairs using the Lennard-Jones potential (LJ), although it is possible to evaluate other short-range interactions. The mathematical description of LJ potential is

$$\mathbf{U}(\mathbf{r_{ij}}) = \mathbf{4}\boldsymbol{\epsilon_{ij}}\left[\left(\frac{\boldsymbol{\sigma_{ij}}}{\mathbf{r_{ij}}}\right)^{\mathbf{12}} - \left(\frac{\boldsymbol{\sigma_{ij}}}{\mathbf{r_{ij}}}\right)^{\mathbf{6}}\right] \qquad \textbf{Equation 2.1}$$

$$\boldsymbol{\sigma_{ij}} = \frac{\mathbf{1}}{\mathbf{2}}(\boldsymbol{\sigma_{ii}} + \boldsymbol{\sigma_{ij}}) \qquad \textbf{Equation 2.2}$$

$$\boldsymbol{\epsilon_{ij}} = (\boldsymbol{\epsilon_{ii}} \cdot \boldsymbol{\epsilon_{jj}})^{\frac{\mathbf{1}}{\mathbf{2}}} \qquad \textbf{Equation 2.3}$$

where $\boldsymbol{\epsilon_{ij}}$ represents the depth of the potential well for a given pair of atomic species and σ_{ij} the interatomic distance at which the inter-particle potential is 0.

Table 2.4 shows the various LJ parameters, all of which are obtained from the literature.[27] Note that we distinguish between the oxygen atoms belonging to the POM and those belonging to the water, since they are chemically different. Although VdW potential is important for a good description of the system, their influence is minimized when it is compared with the electrostatic interactions.[27a] Based on that statement, tungsten and phosphorus use the corresponding alkaline LJ parameters. By extension, we applied the tungsten LJ parameters to molybdenum and we did so for aluminium and silicon, which are also described as regards their corresponding alkaline.

Table 2.4 Lennard-Jones molecular parameters for all the different atomic species

	ε (kJ·mol^{-1})	σ (Å)
Ag	19.0608	2.955
P/Si/Al	1.0264	3.000
W/Mo	0.9250	2.340
O	0.8975	3.170
OW	0.6502	3.166
HW	0.0000	0.000
K	0.4187	3.332

The explanation is that all these species are fully oxidized and it has been assumed that their parameters are equivalent to their corresponding alkaline cations of the same period. In addition, all these species are surrounded by oxo ligands and they are not directly interacting with water, meaning that the error made in this assumption should be minimal. Finally, the crossed terms are obtained using the Lorentz-Berthelot mixing rules, as described in Equation 2.2 and Equation 2.3.[26]

2.3.3. Steps for a simulation

After obtaining the initial configuration, which is explained in section 2.4, the user must follow these steps in order to obtain correct macroscopic properties of the system. These steps are:

- *Minimization*

The initial configuration has a random distribution of species that does not have to be an equilibrium configuration. In order to achieve a better distribution when starting the simulations, we minimize the geometry allowing molecules to move at very low temperatures (about 1 K degree) to ensure that their next position is not placed on a trajectory of collision against another molecule. Reducing the temperature is also combined with very small time-steps, also in order to avoid trajectories of collision between different molecules.

- *Equilibration*

This phase is aimed at leading the system to an equilibrium state in which its macroscopic properties like temperature, pressure and energy fluctuate slightly around an average value without substantially changing. Hence, water molecules and counterions can reach a more natural position with regard to each other and to the POM and the surface. The equilibration protocol is 300 ps in the NVT canonical ensemble.

- *Production Run*

This phase enables enough information to be obtained to compute the macroscopic properties or evaluating the behavior of the species being simulated. The duration of the production run can vary depending on the phenomenon we want to evaluate. In the context of this thesis, the production run aims: (i) to evaluate the behavior of the counterions and (ii) to have a large number of different geometries in which counterions and water molecules are distributed in different ways. In all cases, the production runs lasted 20 ns, with a time-step of 1 fs.

2.3.4. Tools for analysis: Distribution function

Our main goal when using MD simulations is not only to obtain a “random” distribution of water molecules surrounding the POM, but also to find out how the counterions are distributed in the system. We used several distribution functions to analyze this behavior.

- *Counterions trajectories*

The distance plot is a representation of the variation in the distance between two different centers against the simulation time. In this case, we represent the position of one atom time along the Z-axis against the simulation time. This type of representation is called trajectory graphic and it has been applied for counterions. It is useful for analyzing the residence time in different regions and determining different interaction zones with respect to the adsorbed polyoxometalates.

- *Linear distribution function (LDF)*

The linear distribution function is a cumulative function that describes the probability of one counterion being at a given location along the Z-axis. This function is obtained from the aforementioned trajectories, and it is normalized to the number of counterions present in the simulation. It therefore gives the number of counterions by integrating a specific area. This function allows us to distinguish the different regions where counterions are distributed.

- *Surface distribution function (SDF)*

Whereas LDF gives back the distribution of counterions along the z-axis, the SDF gives the probability of finding the counterions in a section delimited from z to z+Δz in the other two directions of the space: the x-axis and y-axis. Although LDF is a normalized function, SDF is not, but it is also useful for evaluating the mobility of the counterions in a section of the box.

- *Radial distribution function*

The radial distribution function (RDF or g(*r*)) is a pair correlation function that describes how the density of particular atomic specie varies as a function of the distance from a reference point, which in our case is another atomic specie. One of the advantages of this function is that it can be experimentally measured using X-Ray or neutron diffraction studies, allowing a comparison between experimental and computational results.

2.5 Geometry extraction: his2vasp

Once trajectories and counterion's behavior have been studied, we take an undetermined number of snapshots from the trajectories. We wrote down a code called His2vasp for executing this task. It extract several snapshots from the trajectories, divides them to obtain one POM per cell and writes down an *.xyz and a POSCAR file (geometry file for VASP) for the adsorbed POM with water molecules surrounding them, as well as counterions for balancing the charge. The code also enables the unit cell to be cut, *i.e.* once the cell is divided into the four original unit cells, the code asks for the height cut-off and returns a geometry with only the solvent molecules and counterions that are below this height.

This code was specially developed for our system (duplication of a cell with an adsorbed POM), and therefore cannot be generally applied to any system. In addition, the code is only able to divide the original structure into four different substructures, which are practically equivalent to each other. If the original system is a 3x3 cell instead of a 2x2 cell, the code will not be suitable for dividing the cell either.

The code works linearly, according to the following steps:

```
> Initiation parameters
```

- First, it looks for the different atomic species found in the MD simulation, determining the number of atoms per atomic specie and the total number of atoms.
- It recovers information about the dimensions of the unit cell.
- It determines the total number of geometries written in the HISTORY file, which is the trajectory OUTPUT file.
- It determines the parameters that allow the program to jump within the HISTORY file to search for a specific geometry.

```
> Inbox panel
```

- The program asks the user for (i) the charge of the POM, (ii) the height at which the cell should be cut, and (iii) how frequently geometries have to be extracted.

> Working code

- Once the code finds the geometry to extract, it reads the atom type and its coordinates.
- The code divides the geometry into four different regions and distributes the atoms depending on their coordinates. Water molecules are distributed by the position of the oxygen atoms, and hydrogens are placed accordingly.
- Vectors are reorganized to put together the different atomic types and are centered with the last metal layer established as the coordinates' origin.

- The code will only write down the geometries that fulfill these conditions:
  - The geometry must have a number of counterions equal to the formal charge of the POM.
  - These counterions must be placed below the cut off introduced by the user.
- If the geometry fulfills the characteristics, the program writes down an *.xyz file with the whole geometry, another *.xyz file with the cut geometry and a POSCAR file with the cut geometry.

The entire working code is repeated until the end of the trajectory file is reached.

Appendix Chapter 2
Theoretical Models and Methods

Appendix 2.1 Energy differences (in eV) for the $SiW_{12}O_{40}$ adsorbed on the √13x√13R33.69° Ag(100) superstructure (with four- and six-metal layers) in two different sites, the H_0 and the T_0.

	3x3x1	5x5x1
4L	0.39	0.42
6L	0.41	0.40

The energetic differences between H_0 and T_0 remain constant; we either increase the number of k-points or the number of metal layers. These results clearly indicate that it is correct to calculate these systems only using 4 metal layers and a Monkhorst-Pack scheme of 3x3x1 k-points.

Appendix 2.2 The unit cell: Matrix notation and Wood's notation

In the case of cubic cells, the name of the different planes matches the normal crystallographic direction for the plane under study. Hence, the (100) plane is the plane in which the [100] crystallographic direction is normal to that plane, and the same is true for the (111) plane.

The primitive unit cell (PUC) is the minimum representation of the surface that can be replicated in the two directions of the space. For the (100) fcc metals, the PUC is a square unit cell where the lattice length of the vectors $|\overrightarrow{a_1}|$ and $|\overrightarrow{b_1}|$ are equal, and their length is related to the cell parameter according to the formula:

$$|\overrightarrow{\mathbf{a_1}}| = |\overrightarrow{\mathbf{b_1}}| = \frac{\sqrt{\mathbf{2}}}{\mathbf{2}} \cdot \mathbf{a_o} \qquad \textbf{Equation 2.4}$$

Another important parameter is the separation between consecutive layers. In the case of fcc metals, the height is straightforward for the (100) surface, since it is half of the cell parameter:

$$\boldsymbol{h_{(100)} = \frac{1}{2} \cdot a_o}$$ **Equation 2.5**

For the (111) fcc metal surface, the PUC is an hexagonal unit cell where $|\overrightarrow{a_1}|$ and $|\overrightarrow{b_1}|$ are also equivalent, but the angle between the two lattice vectors is 120° instead of 90°. The height between layers is obtained by the relation:

$$\boldsymbol{h_{(111)} = \frac{\sqrt{3}}{3} \cdot a_o}$$ **Equation 2.6**

Although it is the minimum representation of one surface, PUC is usually too little for modelling different phenomena such as reconstruction, adsorption or reactivity. It is necessary to define a *superstructure or supercell*, which is the real unit we are going to deal with. Superstructure lattices are labelled as $\overrightarrow{a_2}$ and $\overrightarrow{b_2}$.

- Wood's Notation

This notation can only be applied when the angle α_1 (defined by $\overrightarrow{a_1}$ and $\overrightarrow{b_1}$) and the angle α_2 (defined by $\overrightarrow{a_2}$ and $\overrightarrow{b_2}$) is the same. Wood's notation expresses two labels: first, the proportional relation between $\overrightarrow{a_1}$ and $\overrightarrow{a_2}$ and between $\overrightarrow{b_1}$ and $\overrightarrow{b_2}$, and second, the angle defined by $\overrightarrow{a_1}$ and $\overrightarrow{a_2}$. We take as example the superstructure for Ag(100) in a high coverage situation. $\overrightarrow{a_2}$ is $\sqrt{13}$ times $\overrightarrow{a_1}$; $\overrightarrow{b_2}$ is $\sqrt{13}$ times $\overrightarrow{b_1}$ and the angle defined by $\overrightarrow{a_1}$ and $\overrightarrow{a_2}$ is 33.69°. Wood's notation will therefore label this superstructure as $\sqrt{13}x\sqrt{13}R33.69^o$.

Let us now suppose a superstructure in which $\overrightarrow{a_2}$ is 2 times $\overrightarrow{a_1}$; $\overrightarrow{b_2}$ is 2 times $\overrightarrow{b_1}$ and the angle defined by $\overrightarrow{a_1}$ and $\overrightarrow{a_2}$ is 0°. In this case, Wood's notation would be 2x2R0°. However, when the angle is 0°, it is usually neglected and it is only labeled as 2x2.

- Matrix Notation

Matrix notation is more general than Wood's notation, and there are no restrictions on its use. It specifies the relation between primitive unit cell and the superstructure lattice vectors by means of a matrix, where

$$\left.\begin{aligned}\overrightarrow{a_2} &= G_{11}\overrightarrow{a_1} + G_{12}\overrightarrow{b_1}\\ \overrightarrow{b_2} &= G_{21}\overrightarrow{a_1} + G_{22}\overrightarrow{b_1}\end{aligned}\right\} \rightarrow \begin{pmatrix}\overrightarrow{a_2}\\ \overrightarrow{b_2}\end{pmatrix} = \begin{pmatrix}G_{11} & G_{12}\\ G_{21} & G_{22}\end{pmatrix} \cdot \begin{pmatrix}\overrightarrow{a_1}\\ \overrightarrow{b_1}\end{pmatrix}$$

Following the case of the superstructure for Ag(100) in high coverage, $\overrightarrow{a_2} = 3 \cdot \overrightarrow{a_1} + 2 \cdot \overrightarrow{b_1}$ and $\overrightarrow{b_2} = -2 \cdot \overrightarrow{a_1} + 3 \cdot \overrightarrow{b_1}$. Hence, the matrix notation would represent this superstructure as $\begin{pmatrix}3 & 2\\ -2 & 3\end{pmatrix}$.

References Chapter 2
Computational Details and Models

[1] (a) G. Kresse, J. Furthmuller, *Comput. Mater. Sci.* **1996**, *6*, 15-50; (b) G. Kresse, J. Furthmuller, *Phys. Rev. B: Condens. Matter* **1996**, *54*, 11169-11186; (c) G. Kresse, J. Hafner, *Phys. Rev. B: Condens. Matter* **1993**, *48*, 13115-13118; (d) G. Kresse, J. Hafner, *Phys. Rev. B: Condens. Matter* **1994**, *49*, 14251-14269.

[2] J. P. Perdew, J. A. Chevary, S. H. Vosko, K. A. Jackson, M. R. Pederson, D. J. Singh, C. Fiolhais, *Phys. Rev. B: Condens. Matter* **1992**, *46*, 6671-6687.

[3] H. J. Monkhorst, J. D. Pack, *Phys. Rev. B: Condens. Matter* **1976**, *13*, 5188-5192.

[4] A. D. Vita, M. J. Gillan, *J. Phys.: Condens. Matter* **1991**, *3*, 6225.

[5] M. Methfessel, A. T. Paxton, *Phys. Rev. B: Condens. Matter* **1989**, *40*, 3616-3621.

[6] P. E. Blöchl, *Phys. Rev. B: Condens. Matter* **1994**, *50*, 17953-17979.

[7] (a) G. H. F. Diercksen, S. Wilson, *Methods in Computational Molecular Physics*, Plenum, New York, **1983**; (b) C. Moler, I. Shavitt, *Numerical algorithms in chemistry: algebraic methods. [Workshop, August 9-11, 1978]*, **1978**.

[8] (a) D. M. Wood, A. Zunger, *J. Phys. A: Math. Gen.* **1985**, *18*, 1343-1359; (b) P. Pulay, *Chem. Phys. Lett.* **1980**, *73*, 393-398.

[9] (a) M. P. Teter, M. C. Payne, D. C. Allan, *Phys. Rev. B: Condens. Matter* **1989**, *40*, 12255-12263; (b) D. M. Bylander, L. Kleinman, S. Lee, *Phys. Rev. B: Condens. Matter* **1990**, *42*, 1394-1403.

[10] B. Martorell, A. Clotet, *J. Phys. Chem. C* **2008**, *113*, 950-964.

[11] R. F. W. Bader, *Atom in Molecules: A Quantum Theory*, Oxford University Press, Oxford, **1990**.

[12] G. Henkelman, A. Arnaldsson, H. Jonsson, *Comput. Mater. Sci.* **2006**, *36*, 354-360.

[13] R. Hoffmann, *Solids and Surfaces: A Chemist's View of Bonding in Extended Structures*, Wiley-VCH, New York, **1988**.

[14] J. M. Maestre, X. Lopez, C. Bo, J. M. Poblet, N. Casan-Pastor, *J. Am. Chem. Soc.* **2001**, *123*, 3749-3758.

[15] (a) J. Liu, Y. Li, E. Wang, D. Xiao, L. Fan, Z. Zhang, Y. Wang, *J. Mol. Struct.* **2007**, *837*, 237-244; (b) L. Yuan, C. Qin, X. Wang, Y. Li, E. Wang, *Dalton Trans.* **2009**, 4169-4175; (c) F.-F. Jian, X. Wang, J. Wang, H.-L. Xiao, R.-R. Zhuang, *Polyhedron* **2010**, *29*, 886-896.

[16] (a) S. Elliot, *Physics of Amorphous Materials*, 2nd revised edition ed., **1990**; (b) J. R. Hook, H. E. Hall, *Solid State Pysics*, 2nd Edition ed., Wiley, **1995**.

[17] (a) M. H. Ge, B. X. Zhong, W. G. Klemperer, A. A. Gewirth, *J. Am. Chem. Soc.* **1996**, *118*, 5812-5813; (b) L. Lee, J. X. Wang, R. R. Adžić, I. K. Robinson, A. A. Gewirth, *J. Am. Chem. Soc.* **2001**, *123*, 8838-8843.

[18] C. M. Teague, X. Li, M. E. Biggin, L. Lee, J. Kim, A. A. Gewirth, *J. Phys. Chem. B* **2004**, *108*, 1974-1985.

[19] M. Chelvayohan, C. H. B. Mee, *J. Phys. C* **1982**, *15*, 2305-2312.

[20] (a) F. Ample, A. Clotet, J. M. Ricart, *Surf. Sci.* **2004**, *558*, 111-121; (b) E. M. Karp, C. T. Campbell, F. Studt, F. Abild-Pedersen, J. K. Nørskov, *J. Phys. Chem. C* **2012**, *116*, 25772-25776.

[21] W. Smith, T. R. Forester, *J. Mol. Graphics Modell.* **1996**, *14*, 136-141.
[22] L. Martínez, R. Andrade, E. G. Birgin, J. M. Martínez, *J. Comput. Chem.* **2009**, *30*, 2157-2164.
[23] A. J. Bard, L. R. Faulkner, *Electrochemical methods: fundamentals and applications*, 2nd Edition ed., John Wiley & Sons, Inc., USA, **2001**.
[24] (a) S. Nosé, *J. Chem. Phys.* **1984**, *81*, 511-519; (b) S. Nosé, *Mol. Phys.* **1984**, *52*, 255-268; (c) W. G. Hoover, *Phys. Rev. A* **1985**, *31*, 1695-1697.
[25] W. Jorgensen, *J. Chem. Phys.* **1983**, *79*, 926-935.
[26] M. P. Allen, D. J. Tildesley, *Computer Simulation of Liquids*, Clarendon Press, Oxford, **1989**.
[27] (a) X. Lopez, C. Nieto-Draghi, C. Bo, J. B. Avalos, J. M. Poblet, *J. Phys. Chem. A* **2005**, *109*, 1216-1222; (b) F. Leroy, P. Miro, J. M. Poblet, C. Bo, J. B. Avalos, *J. Phys. Chem. B* **2008**, *112*, 8591-8599; (c) H. Heinz, R. A. Vaia, B. L. Farmer, R. R. Naik, *J. Phys. Chem. C* **2008**, *112*, 17281-17290.

UNIVERSITAT ROVIRA I VIRGILI
COMPUTATIONAL MODELLING OF POLYOXOMETALATES ADSORBED ON METALLIC SURFACES
Xavier Aparicio Anglès
Dipòsit Legal: T. 1525-2013

Chapter 3
Infrared studies on silver surfaces

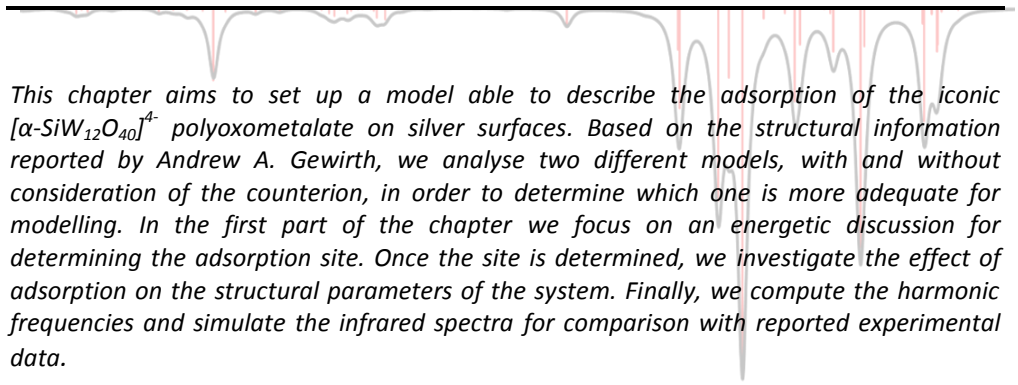

This chapter aims to set up a model able to describe the adsorption of the iconic $[\alpha\text{-}SiW_{12}O_{40}]^{4-}$ polyoxometalate on silver surfaces. Based on the structural information reported by Andrew A. Gewirth, we analyse two different models, with and without consideration of the counterion, in order to determine which one is more adequate for modelling. In the first part of the chapter we focus on an energetic discussion for determining the adsorption site. Once the site is determined, we investigate the effect of adsorption on the structural parameters of the system. Finally, we compute the harmonic frequencies and simulate the infrared spectra for comparison with reported experimental data.

UNIVERSITAT ROVIRA I VIRGILI
COMPUTATIONAL MODELLING OF POLYOXOMETALATES ADSORBED ON METALLIC SURFACES
Xavier Aparicio Anglès
Dipòsit Legal: T. 1525-2013

3.1. Introduction

The engineering of POM-based materials requires an understanding of the interaction between the POM and the matrix. It allows us to move beyond the self-assembly process and attempt to control the interaction between surface and POMs. Indeed, the large number of POM structures in combination with different matrix materials, either organic or inorganic, opens the door to an uncountable number of possible new materials.[1]

In order to understand these systems is absolutely necessary to elucidate the nature of the interaction between the POM and surface. It was in this context when between 1996 and 1997, A. A. Gewirth and his group proposed different models for the structure of α-$H_4SiW_{12}O_{40}$ (HSiW) monolayers on both Ag(100) and Ag(111).[2] These models were obtained by means of Scanning Tunnelling Microscopy (STM) techniques. STM images revealed that, despite their negative charge, POMs tend to adsorb in a high coverage situation.

Another important aspect is the nature of the surface. Several studies revealed that on inert materials like gold or graphite, POMs weakly interact with the surface,[3] whereas on silver surfaces these interactions are stronger.[4] Indeed, in 2001 Gewirth *et al*. indicated that the interaction between POM and silver surface had a strong covalent contribution. These conclusions were obtained from combining STM images with X-Ray Specular Reflectivity measurements, which allowed them to obtain, as an example, silver - terminal oxygen distances of about 2.06 Å.[5]

In order to study with more detail this strong interaction between POMs and surface they sought to use infrared and Raman spectroscopy. They conclude that the interaction with the surface was occurring through POM's bridging oxygen atoms. Furthermore, they proposed a model for the behaviour of the molecule as a function of the potential.[6] Cyclic voltammograms also suggested that $[\alpha\text{-}SiW_{12}O_{40}]^{4-}$ (SiW) could be spontaneously reduced once it is adsorbed on silver surfaces.

3.2. Motivation and objectives

Indeed, the systematic study of the adsorption of SiW on silver surfaces represents a perfect starting point for the theoretical study of these systems. However, from a theoretical point of view, the modeling of the adsorption of POMs on surfaces is a very complex task due to: (i) the periodic nature of the surface; (ii) the size of the adsorbate, which is the polyoxometalate in this case; (iii) the anionic nature of the POM itself; and (iv) the computational demand of this kind of calculations.

Considering all these issues and the data reported for the adsorption of α-$H_4SiW_{12}O_{40}$ on silver surfaces, the aim of this chapter is to present a model with the ability to properly describe the adsorption properties of the anion on this surface. We will consider the unit cells on the two low index surfaces, (100) and (111) proposed by Gewirth and co-workers, as well as other unit cells involving lower coverages. In addition, we will test two different models: the first one considers only the polyoxometalate and the surface and the second one also considers counterions directly linked to the POM. The experimental data will serve to determine the ability of the different models to reproduce experimental results.

In this chapter, we will focus our attention on structural and spectroscopic data, as this information is readily available. The most important part of the chapter is devoted to the infrared spectroscopy, thus the title "*Infrared studies on silver surfaces*". Electrochemical behaviour will be treated in following chapters.

The main goals of this chapter are summarized in the following points:

- ✓ To determine the most favourable active site for the adsorption of α-$SiW_{12}O_{40}$ on Ag(100) and Ag(111) in high and low coverage situations and to compare the geometric results with the experimental data.
- ✓ To evaluate which deposition orientation is favoured: C_3 or S_4 at low coverage regime.
- ✓ To evaluate the nature of the interaction between the POM and the silver surface.
- ✓ To analyse how the adsorption affects the structural integrity of the POM.
- ✓ To calculate the harmonic frequencies of the POMs placed on the most favourable active sites to determine whether they are local minima in the Potential Energy Surface (PES).

- ✓ To describe the vibrational normal modes (VNM) in terms of the different "functional groups" present.
- ✓ To simulate the IR spectrum and compare it with experimental data.
- ✓ To compare results obtained with and without the inclusion of counterions, thereby determining which model is most appropriate in modelling structural properties.

3.3. Computational details

Calculations were carried out using the Perdew-Wang 91 exchange correlation functional[7] and the Projector Augmented Wave (PAW) method for the description of electron-ion interactions.[8] Geometries were optimized to self-consistency with a convergence criterion of $1 \cdot 10^{-5}$ eV and 0.02 eV·Å^{-1} for the electronic and ionic part respectively. The reciprocal space was defined by the 3x3x1 Monkhorst Pack scheme.[9] During optimization, we allowed the POM and the two silver layers closest to the adsorbate to relax.

For computing vibrational frequencies and simulating the infrared spectrum, we enhanced the accuracy of the structure by optimizing the geometries with $1 \cdot 10^{-6}$ eV convergence criteria for the electronic part. Vibrational frequencies were numerically obtained under the harmonic approach, computing the energy gradients for two displacements (0.02 Å) of each atom belonging to the POM unit. IR intensities were calculated from the dipole moment at each displacement using the IRIAN external code.[10] IR spectra were simulated using a lorentzian function with a bandwidth of 1 cm^{-1} and a resolution path of 1 cm^{-1}.

3.4. Adsorption sites

In this first part of the chapter we discussed the relative energies of different adsorption modes of the α-$SiW_{12}O_{40}$ (SiW) on Ag(100) and Ag(111) in different coverage situations.

3.4.1. Ag(100) silver surface

The adsorption of α-$SiW_{12}O_{40}$ on Ag(100) in a high coverage situation (HC) takes place on the $\begin{pmatrix} 3 & 2 \\ -2 & 3 \end{pmatrix}$ unit cell. In this unit cell, only the adsorption *via* the improper S_4 symmetry axis of the POM can be considered due to the size of the cell. Therefore, adsorption orientation was omitted for labelling the adsorption site. Three adsorption sites: on-top (T), hollow (H) and bridge (B) were explored. For each adsorption site, the initial POM orientation was set at different angles (0 and 45 degrees, and also 90 degrees for the Hollow site).

During the optimization, $O_d \cdots O_d$ contacts between neighboring POMs were maximized up to 3.60 Å. As a consequence, the orientation of POMs with respect to the surface changed. As shown in Table 3.1, only those sites with an initial orientation angle different than 0^o suffered reorientation. The lowest energy arrangement corresponds to the POM in hollow site, with an orientation angle of 37 degrees. The site that presents the highest relative energy with respect to H_{37} is the H_0 site, at 10.3 kcal·mol^{-1}. The rest of the sites are found in a range of 5.0 kcal·mol^{-1}, indicating that all of them are thermodynamically accessible.

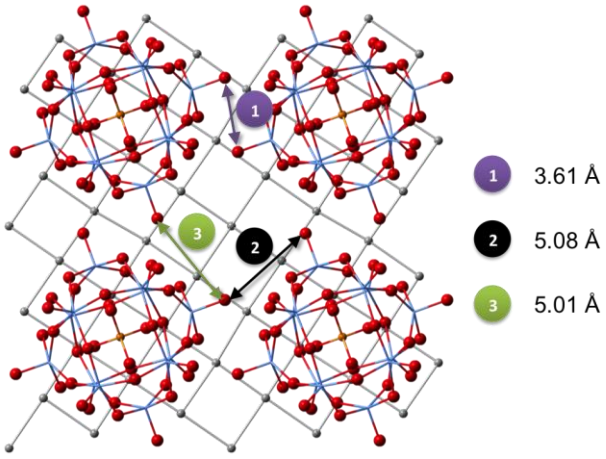

Figure 3.1 Ball-and-stick representation of the 2x2 unit cell for the H_{37} active site in the high coverage situation.

The group of A. A. Gewirth used STM images and X-Ray Specular Reflectivity to determine the POM's adsorption site. They proposed that SiW_{12} would be placed

on a hollow site, with the four terminal oxygens on top of silver surface atoms. Indeed, our results agree with the adsorption site but differ in the orientation angle. This disagreement can be easily explained by considering that in Gewirth's work did not consider repulsion between neighbouring POMs when they adjusted the experimental data. As we considered periodic boundary conditions, these interactions were included in the calculations.

It is worth mentioning that this unit cell involves the highest possible coverage for SiW, but it is not the only possible arrangement. In order to study the adsorption when no interactions among adsorbed POMs exist, we chose the squared $\begin{pmatrix} 4 & 4 \\ -4 & 4 \end{pmatrix}$ unit cell, whose dimensions are 16.64 Å. In this system, distance between POM's terminal oxygen are found between 6.01 and 6.08 Å. Moreover, this superstructure allows us to evaluate the adsorption *via* the C_3 POM symmetry axis, whose study was not possible in the previous HC unit cell.

Table 3.1 Relative energies for $SiW_{12}O_{40}$ adsorbed on Ag(100) in high and low coverage.

	High Coverage			Low Coverage	
Ads. orient.	α_o	α_f	ΔE (kcal·mol^{-1})	α_f	ΔE (kcal·mol^{-1})
S_4	H_{45}	H_{37}	0.0	H_{45}	0.0
	T_{45}	T_{20}	1.9	H_{30}	7.3
	B_{90}	B_{90}	2.7	B_{90}	8.4
	B_0	B_0	3.1	B_0	9.7
	T_0	T_0	4.5	T_0	9.8
	B_{45}	B_{32}	5.0	B_{45}	14.0
	H_0	H_0	10.3	H_0	21.5
	-	-	-	T_{45}	28.7
C_3	-	-	-	B_{17}*	32.8

* The orientation for adsorption *via* C_3 was made considering tungsten and the bridging oxygen not bonded to that tungsten of the upper region of the POM.

When adsorption takes place *via* the S_4 POM symmetry axis, it not only interacts with the surface through four O_d terminal oxygens but also with two O_b and two O_c

bridging oxygens. In contrast, in C_3 adsorption orientation only three O_d oxygens interact with the surface, as well as three O_b or O_c oxygen triads, as depicted in Figure 3.3. Therefore, it is important to state which triad is facing the surface in this orientation. We only considered the O_c-C_3 adsorption orientation, as O_c oxygens are closer to the surface than O_b.

For this coverage situation we studied the same adsorption sites we did for high coverage situation, including the S_4-H_{30} and the C_3–B_{17} active site. After optimization, no reorientation is observed, indicating that the driving force of reorientation is the repulsion between neighboring POMs. For this reason we also calculated the S_4-H_{30} site, closely related with the preferential site at high coverage (H_{37}). Actually, the most probable adsorption site is S_4-H_{45} followed by S_4-H_{30} (7.3 kcal·mol^{-1}). The energetic ordering of S_4 adsorption sites remains approximately similar to that found for high coverage, with the exception of S_4-T_{45}, which is remarkably high in energy in this case (28.7 kcal·mol^{-1}). Actually, this site suffers a major reorientation at high coverage, from 45 to 20 degrees, as a consequence of the electrostatic repulsions, not observed at low coverage.

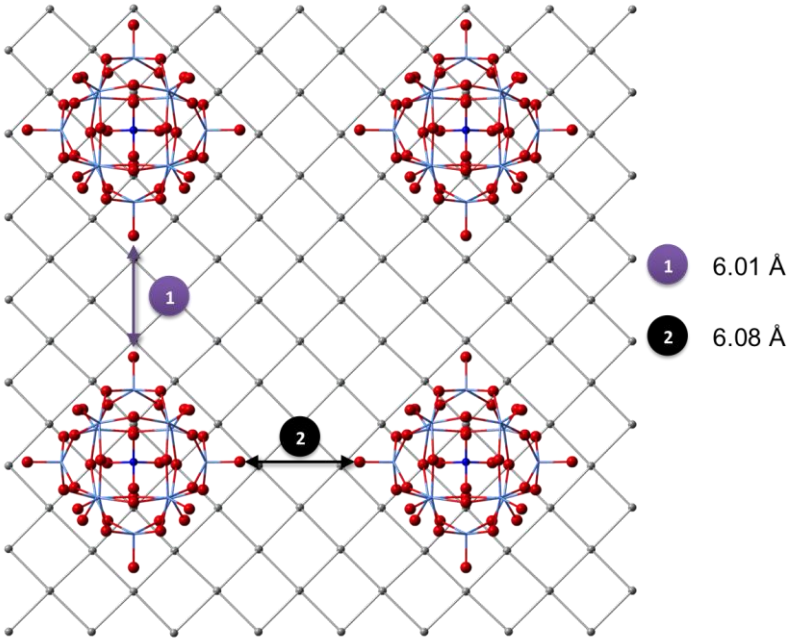

Figure 3.2 Ball-and-stick representation of the 2x2 unit cell for the H_{45} active site for the low coverage situation.

Another conclusion arising from Table 3.1 is that the energy window among all S_4 sites is enlarged. In surface science it is well known that the larger differences in relative energies are, the more covalent the bond between adsorbate and surface becomes. Hence, this energy gap would indicate a more covalent interaction between POM and surface when the coverage decreases. However, from this argument only, the ionic or covalent nature of the interaction could not be revealed.

Finally, adsorption *via* C_3 is found at 32.8 kcal·mol^{-1}. This high relative energy clearly reflects that this adsorption orientation is less favorable than the S_4. Therefore, the possibility of finding POM units adsorbed on Ag(100) *via* C_3 can be dismissed.

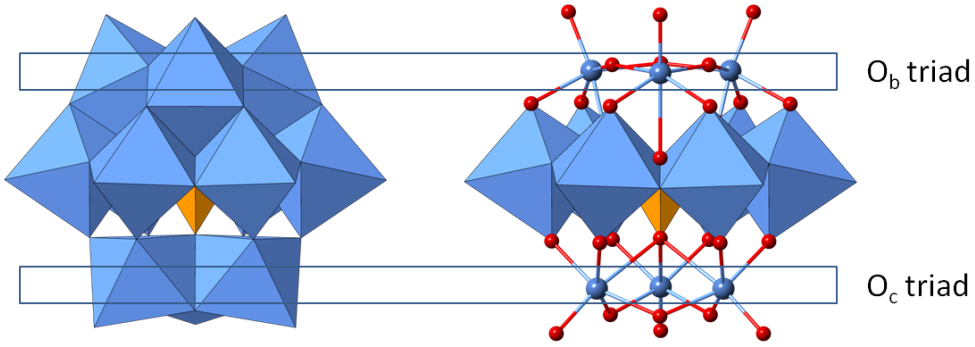

Figure 3.3 Polyhedral and ball-and-stick representation for SiW along it C_3 symmetry axis, in which it is represented the two different triads (O_b and O_c) that can be faced onto the surface.

The high energy of the adsorption *via* C_3 can be rationalized by considering the number of oxygen contacts. As mentioned previously, it is worth noting that when the adsorption takes place *via* the S_4 symmetry axis, eight oxygen atoms are in direct contact with the surface, whereas for the C_3 there are only six (see Figure 3.4). Hence, there is a relationship between the number of oxygen contacts and the preference in the orientation of the POM, at least in the case of α-Keggin anions on Ag(100): the larger the number of oxygen contacts are, the more stable the adsorption mode is.

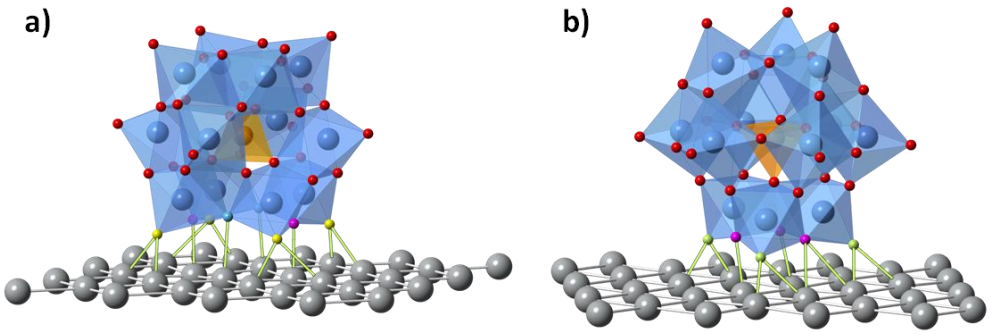

Figure 3.4 Representation of the adsorption *via* a) S_4 and b) C_3 POM symmetry axes. Notice the number of oxygen-silver contacts reflexed in the yellow colored bonds: 8 oxygen-silver contacts for S_4 deposition orientation and 6 oxygen-silver contacts for C_3 deposition orientation.

To quantitatively compare both coverage situations, it is necessary to determine the adsorption energy (E_{ads}), which is defined as:

$$E_{ads} = E_{system} - E_{POM} - E_{slab}$$

where E_{system} is the energy of the whole system, E_{POM}, the energy of the neutral POM in the gas phase and E_{slab} the energy of the clean surface. Since "neutral" POM in the gas phase is not stable, E_{ads} would be overestimated. It seems appropriate to bring the energy reference to the ionic asymptote. The resulting energy is the so-called Ionic Binding Energy (IBE) and it is defined as:

$$E_{IBE} = E_{system} - E_{POM(n-)} - E_{slab} - n \cdot \Phi$$

where $E_{POM(n-)}$ is the energy of the anionic POM in the gas phase, n is the formal charge of the POM, and Φ is the slab workfunction. Notice that $E_{slab} - n \cdot \Phi$ is an approximation to the energy of the cationic slab.

In order to compare the effectiveness of the interaction at different coverages, it would be useful to divide the IBE by the surface area (IBE-a). The values for IBE-a are collected in Table 3.2. The main conclusion arising from these results concerns the high is the major efficiency of the interaction at high coverage. The energy range for high coverage is found between -2.34 and -1.94 eV·nm^{-2}, whereas for low coverage is between -1.38 and -0.80 eV·nm^{-2}. In conclusion, POMs seems to be better accommodated by the surface, as they get closer.

Table 3.2 Ionic Binding Energy per area (IBE-a), in $eV \cdot nm^{-2}$, for SiW on Ag(100) for different coverage situations.

	High Coverage		Low Coverage	
Ads. orient.	α_f	IBE-a	α_f	IBE-a
S_4	H_{37}	-2.34	H_{45}	-1.38
	T_{20}	-2.27	H_{30}	-1.26
	B_{90}	-2.24	B_{90}	-1.24
	B_0	-2.22	B_0	-1.22
	T_0	-2.15	T_0	-1.22
	B_{32}	-2.17	B_{45}	-1.16
	H_0	-1.94	H_0	-1.04
	-	-	T_{45}	-0.93
C_3	-	-	B_{17}	-0.86

3.4.2. Ag(111) silver surface

The group of Gewirth also proposed a unit cell and the corresponding active site for the adsorption of SiW on the Ag(111) surface. The unit cell, $\begin{pmatrix} 4 & 1 \\ 1 & 4 \end{pmatrix}$, also involves the maximum packing allowed for Ag(111). Furthermore, only adsorption *via* the S_4 symmetry axis is possible. We analysed all different active sites: top (T), bridge (B), hollow-fcc (fcc) and hollow-hcp (hcp) considering two starting orientations at 0 and 30 degrees. Technically, we should have also considered initial α values of 60 and 90 degrees but - although not being strictly symmetric - we considered that the differences with respect to 0 and 30 degrees are insignificant.

Finally, we also studied a larger unit cell for Ag(111) defined as the $\begin{pmatrix} 5 & 0 \\ 3 & 6 \end{pmatrix}$ cell for modelling a lower coverage situation. The dimension of this cell also ensures that neighbouring POMs are not directly interacting and permits adsorption *via* the C_3 symmetry axis of the POM. We studied the same active sites with identical starting orientation angles, as well as the C_3 adsorption orientation.

Table 3.3 summarises the results obtained for both coverage situations. Regarding the S_4 adsorption orientation, all sites are found in a narrow range of energies: 11

kcal·mol^{-1} for HC and 8 kcal·mol^{-1} for LC. For both cases, B_{30}, B_0, fcc_0, and hcp_0 are found in a range of only 5 and 2 kcal·mol^{-1}, depending on the coverage, indicating that none of them can be ruled out as possible adsorption site. The lowest energetic site in both cases is the bridge site, in agreement with that proposed by Gewirth for this surface.

On Ag(111) the difference between both coverages comes from the orientation angle, *i.e.* the repulsion between adsorbates. As was observed for Ag(100), repulsion is only important in high coverage, provoking slight reorientations up to 8 degrees in some cases. This difference is also observed in the most probable site, B_{22}, for high coverage and B_0 for low coverage. IBE-a values also reveal that the high coverage situation is favourable compared to low coverage. The difference of approximately 1.2 eV·nm^{-2} is clear evidence of that.

Finally, the C_3-B_{17} adsorption orientation is the most unstable site for low coverage, as in the case of Ag(100). However, its relative energy to B_0 is only 17 kcal·mol^{-1}, half of that for Ag(100) (33 kcal·mol^{-1}). Tentatively, this energetic difference could be associated to the topology of the surface, which is hexagonal for (111) silver surface *vs.* the squared topology observed for Ag(100).

Table 3.3 Relative energies (E_{rel}), Ionic Binding Energy per area (IBE-a) and orientation angles ($\alpha_{o/f}$) computed for all analysed active sites in the Ag(111) surface. α_o and α_f are expressed in degrees; E_{rel} are expressed in kcal·mol^{-1} and IBE-a in eV·nm^{-2}.

	High coverage situation				Low coverage situation		
	α_o	α_f	E_{rel} (kcal·mol^{-1})	IBE-a (eV·nm^{-2})	α_f	E_{rel} (kcal·mol^{-1})	IBE-a (eV·nm^{-2})
S_4	B_{30}	B_{22}	0.0	-2.77	B_0	0.0	-1.50
	fcc_0	fcc_8	4.3	-2.60	B_{30}	1.3	-1.47
	hcp_0	hcp_7	4.5	-2.59	fcc_0	1.7	-1.46
	B_0	B_8	5.3	-2.56	hcp_0	1.8	-1.46
	T_{30}	T_{29}	6.1	-2.53	T_{30}	2.7	-1.44
	fcc_{30}	fcc_{29}	8.1	-2.46	hcp_{30}	4.8	-1.41
	hcp_{30}	hcp_{30}	9.1	-2.42	fcc_{30}	4.8	-1.40
	T_0	T_6	10.7	-2.35	T_0	8.0	-1.34
C_3	-	-	-	-	fcc_9	17.1	-1.16

In conclusion, our model and methods have been able to satisfactorily reproduce the adsorption site of SiW on Ag(100) and Ag(111) surfaces, for the unit cell that involve the highest possible coverage. Concurrently, we have also introduced the first neighbour interactions (considering periodic boundary conditions), allowing us to observe reorientation of the adsorbate, occurring in order to minimize the repulsions. Considering a lower coverage, reorientation is not observed since adjacent POMs are not interacting. Finally, we have also investigated the possibility POM adsorption *via* the C_3 symmetry axis, a possibility that has been rejected, as its relative energy is too high to be considered for both low index surfaces.

3.5. Geometric analysis

Due to the great number of active sites in different surfaces and coverages we computed, only the geometric parameters for the preferred adsorption sites in each surface and coverage - H_{37}, H_{45}, B_{22}, and B_0 - were examined. Table 3.4 presents a collection of average distances for the aforementioned active sites in comparison to the computed distances for the free POM and available experimental values relating its adsorption on silver surfaces. To unravel whether the adsorption orientation has a different impact in the POM's structure, results for C_3 orientations are also summarized in Appendix 3.1.

Upon adsorption, the POM loses its T_d symmetry. The direct consequence of this symmetry breaking is that W atoms become inequivalent and we are forced to distinguish between them. The way we differentiate them is through their relative position with respect to the surface, *i.e.* how far are they placed regarding surface. As presented in Figure 3.5, we distinguish between them W-down (W_d), the closest to the surface, W-equatorial (W_e), found in an intermediate position, and W-up (W_u), furthest from the surface.

Adsorption induces some geometric changes in the POM structure, especially in the region that is directly interacting with the surface, although the overall structure isn't altered significantly. Besides the distortion that the POM suffers, other distances such as the Ag-O_x and Si-Ag distances are also important for determining whether the model we are proposing is adequate in describing geometry.

Ag-O distances are strongly dependent on the active site and the orientation of the POM on the surface. For example, O_d atoms for H_{37} point on a bridge site slightly displaced toward the on-top position, whereas for H_{45} they are all located precisely at bridge position. Consequently, Ag-O_d distances are larger for H_{45} than for the H_{37} site. Considering all the sites, the range of Ag-O_x distances is found between 2.20 and 2.50 Å (with the exception of Ag-O_b distance of 3.03 Å for the B_0 site).

Geometrical parameters do not seem to be dependent on the coverage or the surface. The experimental Ag-O_x distances for SiW, reported by the group of Gewirth only for Ag(100) in high coverage situation are found in the same range for the bridging oxygens and in a shorter range for terminal oxygens (2.06 Å *vs.* our computed values of 2.20 – 2.50 Å). Recall that these values are extrapolated, derived from the X-Ray specular reflectivity for H_0 site.

Furthermore, computed Ag-O_x distances are significantly larger than literature values of 2.15 Å for the atomic oxygen atoms on Ag(111).[11] This result is not unexpected, as O_d interacting oxygen atoms become Ag-O-W bridging atoms upon adsorption. Ag-O_x distances, however, fall within the expected range when we compare them with typical bond distances observed in extended architectures based on POMs and silver coordination complexes.[12] When silver-organic units and POMs are linked through non-covalent interactions, the Ag-O distances are larger: ranging from 2.74 Å to 2.85 Å.[13] Consequently, the relatively short silver-oxygen distances suggest a possible covalent interaction *via* eight Ag-O contacts.

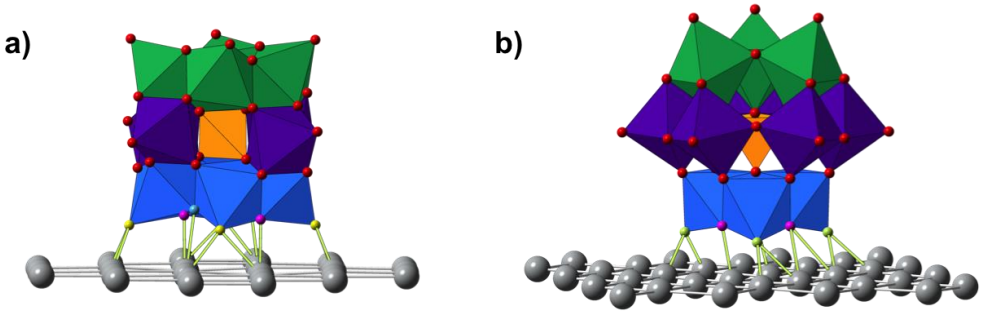

Figure 3.5 Polyhedral representation of the adsorbed SiW on Ag(100) *via* a) S_4 and b) C_3 adsorption orientations. Tungsten-down atoms (W_d) are shown in blue, equatorial tungsten atoms (W_e) in purple, and tungsten-up atoms (W_u) in green.

Table 3.4 Average distances (in Å) for the most stable sites on Ag(100) and Ag(111) at high and low coverage. Experimental values in parentheses.

		Ag(100)		Ag(111)		
type		High cov. H_{37}	Low cov. H_{45}	High cov. B_{22}	Low cov. B_0	Ref.
Ag	O_b	2.44 (2.43)[b]	2.50	2.50	3.03	
	O_c	2.20 (2.23)[b]	2.22	2.34	2.40	
	O_d	2.20 – 2.29 (2.06)[b]	2.36 – 2.54	2.35 – 2.46	2.39 – 2.44	
Si	Ag	5.53 (4.90)[a]	5.51	5.48	5.53	
	O_a	1.62 – 1.64	1.63 – 1.66	1.62 – 1.66	1.62 – 1.65	(1.64)
O_a	W_u	2.48	2.46	2.47	2.46	(2.39)
	W_e	2.35 – 2.52	2.35 – 2.51	2.34 – 2.54	2.34 – 2.51	
	W_d	2.27	2.29	2.26	2.27	
O_b	W_u	1.92 – 1.97	1.92 – 1.96	1.91 – 1.96	1.92 – 1.96	(1.94)
	W_e	1.88 – 2.02	1.89 – 2.01	1.88 – 2.01	1.88 – 2.01	
	W_d	1.87 – 2.02	1.85 – 2.00	1.83 – 1.99	1.85 – 1.96	
O_c	W_u	1.93 – 1.97	1.93 – 1.97	1.92 – 1.97	1.92 – 1.97	(1.93)
	W_e	1.88 – 2.01	1.89 – 2.00	1.88 – 2.01	1.88 – 2.00	
	W_d	1.87 – 2.02	1.88 – 2.00	1.87 – 2.02	1.87 – 2.03	
O_d	W_u	1.70	1.71	1.71	1.71	(1.74)
	W_e	1.71	1.72	1.71	1.71	
	W_d	1.80	1.80	1.81	1.80	

[a] Si-Ag distance obtained from X-Ray Specular Reflectivity data.[5]

[b] Ag-O distances obtained by extrapolation from Si-Ag distances

Another parameter that provides information about the POM-surface distance is the Si-Ag distance, which has been determined to be 4.90 ± 0.02 Å using X-Ray Specular Reflectivity for Ag(100) in high coverage situation.[5] Computational results provide a distance of 5.50 Å, 0.6 Å longer than that derived experimentally, independent of the surface or the coverage. The same behaviour is observed in the W_x-O_y distances: regardless of the coverage and the surface, distances are

approximately the same in all four different sites showed in Table 3.4. In conclusion, the interaction between SiW and Ag is the same in all coverage situations and on all surfaces.

W_x-O_y distances suffer distortion after adsorption, an effect most pronounced in the region of the POM closest to the surface, with deviations of about ± 0.1 Å. The bridging bonds closest to the surface follow an alternating sequence of short/long bonds, similar to the distortion observed in molybdates.[14] This alternating bond length distortion is obviously less pronounced in the distal moieties of the anion. It is worth mentioning that the rather weak W-O_a bond contracts or elongates depending on the proximity of the internal O_a oxygen to the surface. These distortions seem to be conditioned by the distortion of the external $W_{12}O_{36}$ unit.

Finally, for the C_3 adsorption mode, distortions are also related to the proximity of atoms (and bonds) to the surface. As shown in Appendix 3.1, distortions are not significantly different from the ones observed for S_4 adsorption mode. W_d-O_d also elongates 0.1 Å with respect to $W_{e/u}$=O_d indicating the formation of a Ag-O_d-W_d bridge bond. The other distances reveal distortions similar to those found in the S_4 adsorption orientation. In conclusion, adsorption induces the same kind of distortion, regardless of orientation.

3.6. Frequency analysis and infrared spectrum

Minimized structures reported in previous sections correspond to stationary points on the Potential Energy Surface (PES). In order to ensure they are true minima of the PES, it is necessary to carry out frequency calculations. Unfortunately, each calculation is high time demanding, so it is prohibitive to analyse all the aforementioned sites.

Indeed, in all coverage situations and with all surfaces we found various possible arrangements and, in addition, structure distortion was also similar in all cases (with little exceptions). In light of this information, we decided to analyse the frequencies for the lowest energy adsorption sites for each surface and coverage combination. For Ag(111) we also computed the IR of two additional near-degenerate sites to discern the effects of several domains contributing to the IR. Finally, we computed the IR spectrum of the C_3-site in order to determine

whether vibrational spectroscopy can discern between the two adsorption orientations.

After simulating each infrared spectrum, we assigned the Vibrational Normal Modes (VMM) to the corresponding frequencies. Although each VNM is indeed the assignment of the corresponding fundamental band, we translated this information in terms of the movements associated with various "functional groups". Due to the high symmetry (T_d) of the isolated POM, the assignment of frequencies should not be an arduous task. However, when POM is adsorbed onto the surface, the symmetry of the whole system is lost (C_{2v} or C_1), with only a few symmetry elements such as C_2 or σ retained. This symmetry lowering has two main consequences: first, all fundamental bands are IR-active; second, motions of different "functional groups" are not as well separated as they are in the isolated molecule. For these reasons, we only assigned those frequencies higher than 300 cm^{-1} with an associated intensity higher than 10 $km \cdot mol^{-1}$.

3.6.1. Hollow 37 – Ag(100) high coverage situation

The frequencies and their corresponding intensities and assignments are listed in Table 3.5. No negative frequencies were found in the frequency analysis, which indicates that these sites correspond to true minima on the Potential Energy Surface.

Higher frequencies are associated with both symmetric and asymmetric stretches of $W_{e/u}=O_d$ above 950 cm^{-1}. The rest of the frequencies appear below this value, in agreement with the fact that terminal oxygens are doubly bonded to the tungsten, whereas the rest show a single bond. At 951 cm^{-1} the second most intense band of the spectra appears, also associated with the stretching of the $W_e=O_d$ functional group, but also coupled with the asymmetric stretching of the $Si-O_a$ bonds, and also with the symmetric stretching of the $W_e-O_{b/c}-W_u$ bonds. In fact, both symmetric and asymmetric $Si-O_a$ stretching covers a region between 950 and 800 cm^{-1}, and they are present in the bands at 951, 891, 855, 835, and 821 cm^{-1}. In the same way, $W_x-O_{b/c}-W_y$ stretching appears between 950 and 800 cm^{-1}, and it is also found in the aforementioned bands.

Table 3.5 Selected vibrational frequencies (ω) in cm^{-1}, associated intensities (I) in $km \cdot mol^{-1}$, and assignments for $SiW_{12}O_{40}$ adsorbed on Ag(100) in the H_{37} site.

ω	I	Assignment
1035	35	$\upsilon_s(W_u=O_d)$
1015	92	$\upsilon_{as}(W_e=O_d)$
1009	42	$\upsilon_s(W_e=O_d)$
951	249	$\upsilon_{as}(Si\text{-}O_a)$; $\upsilon_{as}(W_e=O_d)$; $\upsilon_s(W_e\text{-}O_{b/c}\text{-}W_u)$
917	29	$\upsilon_{as}(W_x\text{-}O_{b/c}\text{-}W_y)^a$
891	62	$\upsilon_s(W_x\text{-}O_{b/c}\text{-}W_y)^a$; $\upsilon_{as}(Si\text{-}O_a)$; $\upsilon_s(Ag\text{-}O_d\text{-}W_d)$
855	25	$\upsilon_s(Si\text{-}O_a)$; $\upsilon_{as}(W_e\text{-}O_b\text{-}W_x)^a$; $\upsilon_s(Ag\text{-}O_d\text{-}W_d)$
835	329	$\upsilon_s(Ag\text{-}O_d\text{-}W_d)$; $\upsilon_s(Ag\text{-}O_c\text{-}W_d)$; $\upsilon_s(Si\text{-}O_a)$
821	188	$\upsilon_s(W_x\text{-}O_b\text{-}W_e)^a$; $\upsilon_s(Si\text{-}O_a)$
735	14	$\upsilon_{as}(Ag\text{-}O_d\text{-}W_d)$
530	16	$\delta(Si\text{-}O_a)$; $\delta(W_{d/u}\text{-}O_c\text{-}W_{e/u})$; $\delta(W_d\text{-}O_c\text{-}W_d)^b$
521	11	$\delta(Si\text{-}O_a)$; $\delta(W_d\text{-}O_c\text{-}W_d)$;^{b} $\delta(W_u\text{-}O_c\text{-}W_u)$
514	14	$\delta(W_x\text{-}O_c\text{-}W_y)$;^{a} $\delta(Si\text{-}O_a)$
379	43	$\delta(W_x\text{-}O_{b/c}\text{-}W_y)^a$

υ_s = symmetric stretching; υ_{as} = asymmetric stretching; δ = bending.

[a] x and y labels mean that no specific tungsten atom is involved in the movement.

[b] This movement causes $\upsilon(Ag\text{-}O_c)$

The most intense band in the spectrum is found at 835 cm^{-1} where, despite the coupling with $Si\text{-}O_a$ stretching, the assignment of this band is primarily related to the stretching of O_d terminal and silver surface atoms. This $Ag\text{-}O_d\text{-}W_d$ stretch appears in the bridging oxygen region instead of appearing with the terminal oxygens (above 1000 cm^{-1}). This fact, in addition to the elongation that the $W_d=O_d$ bonds suffer, only reinforces the idea that a covalent $Ag\text{-}O_d\text{-}W_d$ bond has been formed. This stretch also appears between 850 and 700 cm^{-1}, slightly below the region of the $W_x\text{-}O_{b/c}\text{-}W_y$ stretching, but lower in intensity.

Below 700 cm^{-1} there are only two noticeable bands, defined by four different VNM. The bands at 530, 521, and 514 are primarily a result of the bending of $Si\text{-}O_a$ bond and $W_x\text{-}O_c\text{-}W_y$ bonds. The specific $W_d\text{-}O_c\text{-}W_d$ bending generates a displacement of the oxygen with respect to the surface, which can be also

associated to the Ag-O_c stretching. Finally, the band at 379 cm^{-1} is described by the bending of the W_x-$O_{b/c}$-W_y bonds.

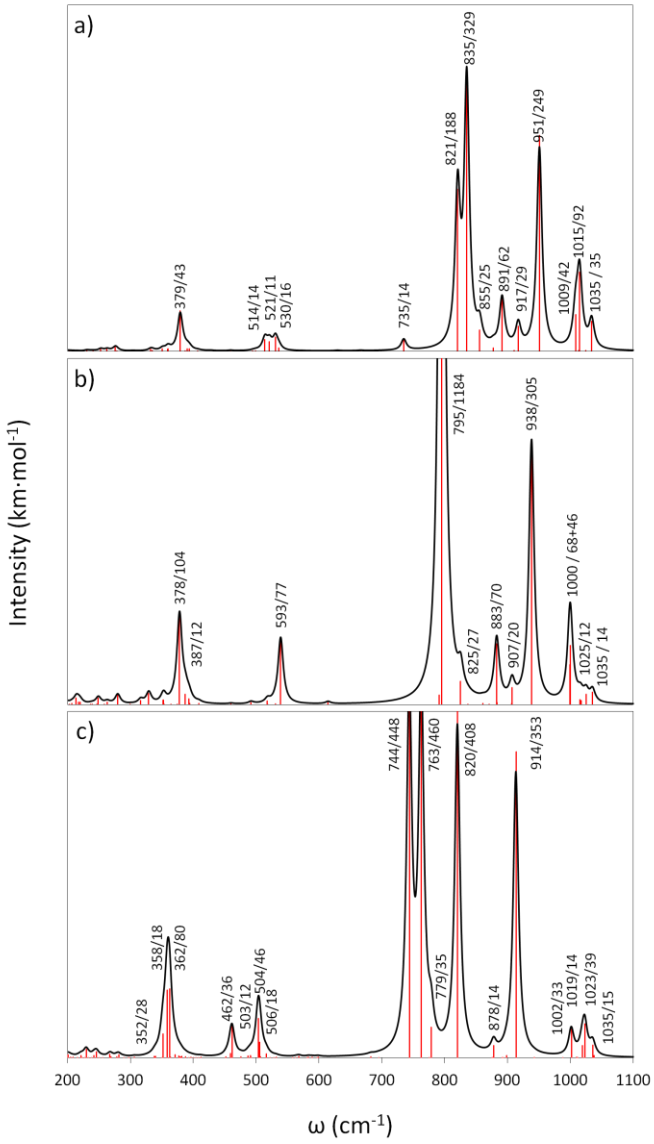

Figure 3.6 Simulated infrared spectrum for $SiW_{12}O_{40}$ adsorbed on Ag(100) surface: a) S_4-H_{37} site for high coverage; b) S_4-H_{45} site for low coverage; c) C_3-B_{17} site for low coverage. Intensity scale from 0 to 400 km·mol^{-1} for all spectra.

3.6.2. Hollow 45 – Ag(100) low coverage situation

The frequency analysis for H_{45} adsorption site also reveals that it is a minimum on the PES, as no imaginary frequencies are obtained. The description of the VNM is quite similar to that ascribed to the high coverage situation (see Table 3.6), though a ubiquitous shift to lower frequencies was observed, indicating a weaker interaction. Above 940 cm^{-1} we find both symmetric and asymmetric $W_{e/u}=O_d$ stretches. Si-O_a stretching appears between 940 and 820 cm^{-1}, and W_x-$O_{b/c}$-O_y between 940 and 790 cm^{-1}. Finally, between 600 and 350 cm^{-1} W_x-$O_{b/c}$-O_y and Si-O_a bending are the predominant functional group motions describing the VNM.

Table 3.6 Selected vibrational frequencies (ω) in cm^{-1}, associated intensities (I) in $km \cdot mol^{-1}$, and assignments for $SiW_{12}O_{40}$ adsorbed on Ag(100) in the H_{45} site.

ω	I	Assignment
1035	14	2 $\upsilon_s(W_e=O_d)$
1025	23	$\upsilon_s(W_u=O_d)$
1000	68 + 46	$\upsilon_{as}[1\ \upsilon(W_e=O_d) + 2\ \upsilon_s(W_u=O_d)]$
938	305	υ_{as}(Si-O_a); $\upsilon_s(W_e=O_d)$; $\upsilon_s(W_e$-O_b-$W_d)$
907	20	υ_{as}(Si-O_a); $\upsilon_s(W_e$-$O_{b/c}$-$W_{u/d})$
883	70	υ_s(Si-O_a); $\upsilon_s(W_e$-$O_{b/c}$-$W_{u/d})$
825	27	υ_s(Si-O_a); $\upsilon_s(W_x$-O_c-$W_y)$;[a] υ_s(Ag-O_d-W_d)
795	1184	υ_s(Ag-O_d-W_d); $\upsilon_s(W_x$-$O_{b/c}$-$W_y)$
791	11	υ_{as}(Ag-O_d-W_d); $\upsilon_{as}(W_x$-$O_{b/c}$-$W_y)$
593	77	$\delta(W_d$-O_c-$W_d)$;[a] $\delta(W_{e/u}$-O_c-$W_u)$; δ(Si-O_a)
387	12	$\delta(W_d$-O_b-$W_d)$;[b] $\delta(W_x$-$O_{b/c}$-$W_y)$
378	104	$\delta(W_x$-$O_{b/c}$-$W_y)$

υ_s = symmetric stretching; υ_{as} = asymmetric stretching; δ = bending.

[a] x and y labels mean that no specific tungsten atom is involved in the movement.

[b] This movement causes υ(Ag-O_c)

[c] This movement causes υ(Ag-O_b)

As in the high coverage situation, the most intense band, at 795 cm^{-1}, is related to the Ag-O_d-W_d stretches. The difference of 40 cm^{-1} between the band in high and

low coverage can be attributed to the absence of coupling with the Si-O_a symmetric stretching and the weaker interaction (larger Ag-O_d distances) with the surface. Regardless of these differences, the zones defined in the high coverage situation are the same in the low coverage situation, despite of some minimal displacements.

3.6.3. C_3 – Ag(100) low coverage situation

We previously showed the C_3 adsorption orientation is remarkably less favourable than the S_4. The aim of this section is to determine whether it is possible to discern between both adsorption orientations using IR spectroscopy. The first thing to highlight is that no negative frequencies are reported, so adsorption site in question, the C_3-B_{17} also represents a relative minimum in the PES.

The description of IR regions does not deviate significantly from the S_4 orientation. Above 1000 cm^{-1}, VNM are mainly described by υ($W_{e/u}$=O_d). Between 920 and 740 cm^{-1}, both symmetric and asymmetric stretching υ(W_x-$O_{b/c}$-W_y) and υ(Si-O_a) are governing this region. υ(Ag-O_d-W_d) stretching frequencies appear from 800 to 740 cm^{-1}, all of them coupled with υ(W_x-$O_{b/c}$-W_y) and υ(Si-O_a). Finally, δ(W_x-$O_{b/c}$-W_y), and consequently υ(Ag-$O_{b/c}$), are found between 500 and 350 cm^{-1}.

Minimal region displacements are observed when varying the POM adsorption orientation. However, the region where the Ag-O_d-W_d stretching appears is clearly shifted to lower frequencies with respect to the S_4 orientation. This observation can be rationalized in two ways. On one hand, the number of W_d-O_d-Ag contacts is lower (6 contacts *vs.* 8 contacts when POM is adsorbed *via* S_4), which has a direct impact on the position and intensity of the bands. On the other hand, the formal site in which these oxygens are interacting is not the same. In the case of H_{37} (high coverage), two of the four oxygen atoms are placed on top whereas the other two are on bridge. For H_{45} (low coverage) all terminal oxygens are on bridge. However, for the C_3-B_{17} adsorption mode, one of the oxygen atoms is placed on hollow and the other two on bridge.

Table 3.7 Selected vibrational frequencies (ω) in cm^{-1}, associated intensities (I) in $km \cdot mol^{-1}$, and assignments for $SiW_{12}O_{40}$ adsorbed on Ag(100) in the C_3–B_{17} site.

ω	I	Assignment
1035	15	$\upsilon_s(W_{u/eq}=O_d)$
1023	39	$\upsilon_s(W_{u/eq}=O_d)$
1019	14	$\upsilon_{as}(W_u=O_d)$; $\upsilon_s(W_{eq}=O_d)$
1002	33	$\upsilon_s(W_{u/eq}=O_d)$
914	353	$\upsilon_s(Si\text{-}O_a)$; $\upsilon_s(W_d\text{-}O_b\text{-}W_{eq})$
878	14	$\upsilon_s(Si\text{-}O_a)$; $\upsilon_s(W_d\text{-}O_b\text{-}W_{eq})$
820	408	$\upsilon_s(Ag\text{-}O_d\text{-}W_d)$; $\upsilon_s(W_{eq}\text{-}O_c\text{-}W_u)$; $\upsilon(Si\text{-}O_a)$
779	35	$\upsilon_s(Ag\text{-}O_d\text{-}W_d)$; $\upsilon_s(W_x\text{-}O_{b/c}\text{-}W_y)$[a]
763	460	$\upsilon_s(Ag\text{-}O_d\text{-}W_d)$; $\upsilon_s(W_x\text{-}O_{b/c}\text{-}W_y)$;[a] $\upsilon(Si\text{-}O_a)$
744	448	$\upsilon_s(Ag\text{-}O_d\text{-}W_d)$; $\upsilon(Si\text{-}O_a)$
506, 504, 503[b]	18, 46, 12	$\delta(W_d\text{-}O_c\text{-}W_d)$;[c] $\delta(W_{eq}\text{-}O_{b/c}\text{-}W_u)$
462	36	$\delta(W_d\text{-}O_c\text{-}W_d)$;[c] $\delta(W_d\text{-}O_b\text{-}W_{eq})$
362, 358, 352	80, 78, 28	$\delta(W_d\text{-}O_b\text{-}W_d)$;[d] $\delta(W_{eq}\text{-}O_{b/c}\text{-}W_{eq})$

υ_s = symmetric stretching; υ_{as} = asymmetric stretching; δ = bending.

[a] x and y labels mean that no specific tungsten atom is involved in the movement.

[b] All three frequencies have the same assignment

[c] This movement causes $\upsilon(Ag\text{-}O_c)$

[d] This movement causes $\upsilon(Ag\text{-}O_b)$

It is well established that frequencies associated to the stretching of an adsorbed species with respect the surface are strongly related with the adsorption site. Hence, $\upsilon_H < \upsilon_B < \upsilon_T$ which means that the higher the number of terminal oxygens placed on top, the higher the frequency will be. In conclusion, both factors explain why these frequencies appear at lower values in the C_3 orientation.

Finally, in the region below 500 cm^{-1} there are two bands for adsorption *via* the S_4 axis, whereas when the adsorption occurs *via* C_3, three bands appear. Therefore, the number of strong bands in the region between 750 – 850 cm^{-1} and the number of bands below 500 cm^{-1} can be considered the fingerprints of these systems. It

can be concluded, then, that IR technique is able to distinguish between both S_4 and C_3 adsorption orientations on the Ag(100) surface

3.6.4. Ag(111) surface, high coverage situation.

No negative frequencies were found for the calculated systems, and consequently all of them are relative minima in the PES. The description of the functional group regions is almost identical to the description of the (100) surface for all the sites. Above 940 cm^{-1} we find the $W_{e/u}=O_d$ stretch, and in the region between 1000 and 800 cm^{-1} we find the Si-O_a stretching. The W_x-$O_{b/c}$-W_y stretches are found between 1000 and 800 cm^{-1}, and the Ag-O_d-W_d stretching approximately between 850 and 700 cm^{-1}. Finally, both Si-O_a and W_x-$O_{b/c}$-W_y bends are found between 500 and 380 cm^{-1}. Specific assignments for all spectra are available in the appendix of this chapter.

Contrary to the Ag(100) surface, for which no experimental data were available, Gewirth reported an exhaustive work regarding the infrared reflection-absorption spectra of $[SiW_{12}O_{40}]^{4-}$ on a Ag(111) surface at different potentials. The technique that they employed was Polarized Infrared Reflection-Absorption Spectroscopy (PM-IRRAS). The technique allows for the determination of an IR spectrum for adsorbed species discriminating those found beyond 1 μm from the chemisorbed ones (in this specific case).[6] Therefore, for this surface we can compare these results with our simulated spectrum, and thus determine whether our model is appropriate for reproducing the IR spectrum, and consequently, the structural parameters.

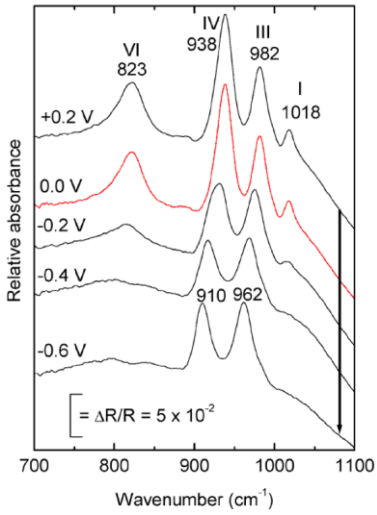

Figure 3.7 Experimental PM-IRRAS for Ag(111) in 1 mM α-$SiW_{12}O_{40}^{4-}$ + 0.1 M $HClO_4$ at various potentials from positive to negative potential-going step. This spectrum has been taken from reference: *"Vibrational Spectroscopy of a Keggin Polyoxometalate on Metal Electrode Surfaces"*, paper published in *J. Phys. Chem. B* in 2004 by Gewirth *et al.*[6] In red the spectrum relative to 0 V potential has been highlighted. Frequencies listed in this figure belong to the assignation at +0.2 V potential.

In Figure 3.7 the IRRAS spectra at 0 V (no potential difference is applied in this case) shows 4 different bands, at 1018, 982, 938 and 823 cm^{-1}. The simulated spectrum for B_{22} (shown in the top-left part of Figure 3.8) presents three bands placed at 1002, 940, and 815 cm^{-1}, instead of 4. Although the number of bands does not match, the positions of existing bands agree to within 16 cm^{-1}.

Experimental band assignment is according to those derived from VNM analysis, despite the band at 815 cm^{-1}. Gewirth *et al.* assigned this band to υ_{as}(W-O_c-W), whereas we assigned this band to Ag-O_d-W_d stretching. This disagreement can be accounted for by considering that, on one hand, no bond between POM and surface was taken into account. Therefore, W_d=O_d stretches were all assigned above 1000 cm^{-1}, and Ag-O stretching was placed below 200 cm^{-1}.

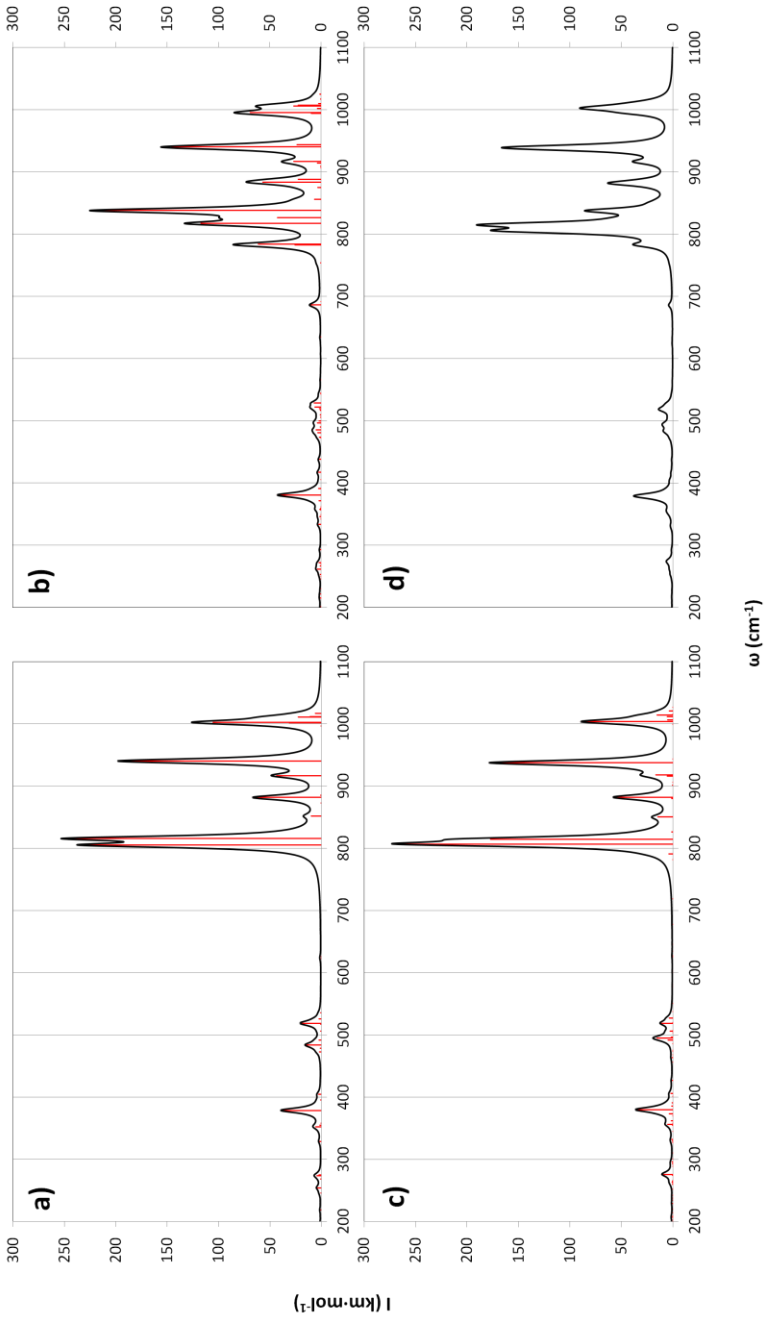

Figure 3.8 Infrared spectra for $SiW_{12}O_{40}$ adsorbed on Ag(111) in a) B_{22}, b) hcp_7, c) T_{30} and, d) IR spectrum resulting from averaging the previous spectra.

In contrast, our assignment indicates that, since Ag-O bonds are formed, the bond order for W=O decreases and the whole "functional group" Ag-O-W should appear in the O bridge "stretching region", between 950 and 750 cm^{-1}. On the other hand, this band is the most sensitive to the potential sweep. As the potential becomes more negative, this band loses intensity until disappearing. This fact agrees with our band assignment, as the anions are expected to desorb at negative potential.

However, we cannot explain the absence of the band placed at 982 cm^{-1}. Under experimental conditions, the spectrum is built up from contributions from different domains, *i.e.* different regions where either the coverage or the adsorption site can be different. Hence, we decided to expand frequency analysis to two more adsorption sites: hcp_7 and T_9. This election is not trivial: b_{22} is the lowest in energy adsorption site, followed by fcc_8, hcp_7, B_8, and T_9 (see Table 3.3 for further information). Fcc_8 and fcp_7 are nearly degenerated, presenting the same kind of oxygen-silver contacts (2 bridge and 2 on-top). For this reason we decided to compute only one infrared spectrum for both hollow sites. B_8 involves the same adsorption site and presents almost the same kind of oxygen-silver contacts found in B_{22} (although the relative orientation is not the same) so we discarded this site. Finally, T_9 presents a different adsorption site and different contacts than B_{22}.

As shown in Figure 3.8, the shape of IR spectra for hcp_7 and T_{30} is rather similar to B_{22}. It is worth mentioning that in the specific case of hcp_7, instead of having one band centred at approximately 810 cm^{-1}, it presents three bands close to 810 cm^{-1} (838, 817, and 783 cm^{-1}). All of them appear in the expected region and the variation of the exact value depends on the nature of the interaction between terminal oxygen and surface atoms. An average spectrum has been also simulated, revealing that the shape does not change dramatically with respect to the first spectrum we calculated, the B_{22}.

The band at 980 cm^{-1} does not appear in any spectra, so the contribution of different domains is clearly not responsible of this band. It is most likely to be due to the surrounding environment that has not been considered in our model. In fact, Rocchiccioli and Deltcheff carried out an exhaustive study regarding infrared spectroscopy for several POMs.[15] One of the conclusions of this work was that the region between 900 and 1000 cm^{-1} is very sensitive to counterions effects. Thus, as

our model does not consider either the effect of the solvent or of the counterions, it is understandable that this region is not well described.

3.6.5. Ag(111) surface, low coverage situation.

For Ag(111) we also performed frequency analysis at low coverage for B_0 and C_3-fcc_9 adsorption sites. Both are true minima on the PES, as no negative frequencies are found. The regions defined in both spectra, depicted in Figure 3.9, are similar to those determined in Ag(100).

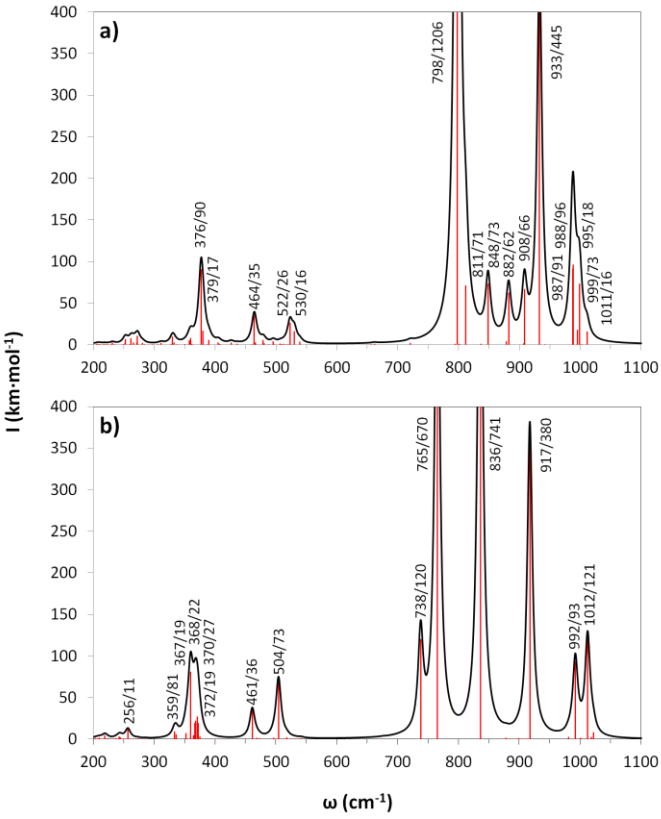

Figure 3.9 Simulated infrared spectrum for $SiW_{12}O_{40}$ adsorbed on a) B_0 and b) C_3–fcc_9 adsorption sites at low coverage for Ag(111) surface.

Starting with B_0, whose frequencies are listed in Appendix 3.2, the region where $W_{e/u}=O_d$ stretching appears is above 930 cm^{-1}; between 940 and 880 cm^{-1} we find the Si-O_a stretching, and between 910 and 800 cm^{-1} the W_x-$O_{b/c}$-W_y stretchings. From 880 to 790 cm^{-1} the Ag-O_d-W_d stretching appears, and finally, the bending related to the Si-O_a and the W_x-$O_{b/c}$-W_y functional groups are below 500 cm^{-1}. In this spectrum we find at 379 cm^{-1} the W_u-O_c-W_u wagging, a movement that has not been observed in this region for any of the analysed sites.

Focusing now with the C_3–fcc$_9$ adsorption orientation, above 990 cm^{-1} we find the $W_{e/u}=O_d$ stretching; between 920 and 730 cm^{-1} the Si-O_a and the W_x-$O_{b/c}$-W_y stretching; between 880 and 790 cm^{-1} the Ag-O_d-W_d stretching and below 500 cm^{-1} the Si-O_a and W_x-$O_{b/c}$-W_y bending. Comparing the B_0 and the C_3-fcc$_9$ for this surface and coverage, we realize that below 500 cm^{-1} there are three bands for both systems, in contrast to what we saw for Ag(100). This means that it is not possible to differentiate both adsorption orientations in this region.

In addition, neither the regions nor the shape of the spectra significantly differ from the results obtained for the Ag(100) surface. The regions are rather similar and the orientation-dependant frequency shifting is also observed for this surface.

3.7. Model with counterions

The previous model had been able to describe the adsorption site, the structural parameters and also to reproduce quite acceptably the infrared spectra. However, this model was not able to reproduce a specific region - between 900 and 1000 cm^{-1} - since it is influenced by the interaction of the POMs with the counterions. Consequently, it seems necessary to include the counterions in the model.

Although reproducing the aforementioned aspects, exclusion of the counterion requires that the POM is considered not as an anion, but as a neutral specie. Neutral POMs are unstable, both in gas phase and in solution, as they want to fill the empty oxygen orbitals; they present exaggerated oxidant strength that is overestimated. On the other hand, the silver surface is a reducing agent that can transfer electrons with no effort to the adsorbate, apart from being very reactive with oxygen. Hence, it is necessary to evaluate how the presence of counterions

can correct the POM oxidant strength and, at the same time, how this affects the energies, structural parameters, frequencies, and the IR spectrum.

In the experiments, the POMs counterions were protons, which, from a computational point of view, are tricky to deal with, essentially because they can be directly bonded to the POM. Instead of protons we decided to use potassium as counterions. Potassium cations are not supposed to be directly bonded to POMs, so calculations should be easier (*a priori*).

Another aspect that must be considered is where counterions are located. The most likely situation is that K^+ ions are surrounding the POM but not in a specific region. Because of that, we have investigated two different positions: close to the O_b triads and close to the O_c triads. Three tungsten atoms define these triads, as shown in Figure 3.10; O_b or O_c label depends on the oxygen type that is bonding to those tungsten atoms.

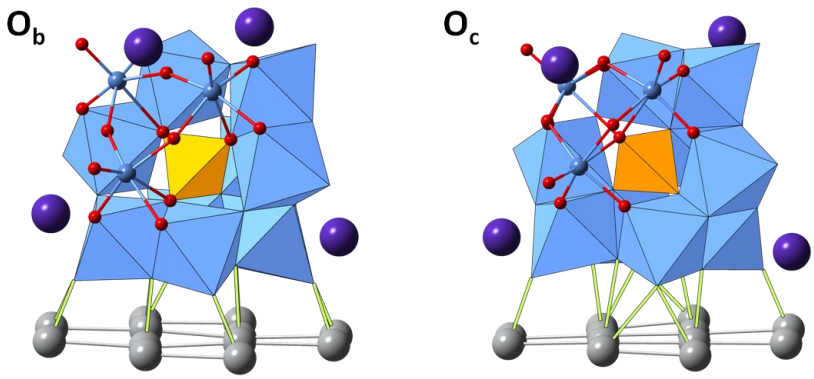

Figure 3.10 Schematic representation of counterions allocated on O_b and O_c triads.

Firstly, we have analysed where the counterions are most likely to be found for the isolated POM. K^+ ions prefer to be allocated on the O_b triads rather than being close to the O_c triads, by the data in Table 3.8. Independently, we investigated both adsorption situations to see whether this energy difference increases or decreases on the adsorption occur.

Table 3.8 Relative energy (E_{rel}) in kcal·mol^{-1}, adsorption energy (E_{ads}) in eV, and orientation angles (α_f) in degrees computed for $K_4SiW_{12}O_{40}$ on the Ag(100) surface.

α_f	E_{rel}	E_{ads}
O_b	0.0	-
O_c	13.7	-
$O_b - T_2$	0.0	-2.18
$O_c - T_1$	5.4	-1.95
$O_c - H_{32}$	10.8	-1.72
$O_b - H_{36}$	10.9	-1.71
$O_b - H_{10}$	11.2	-1.70
$O_c - H_0$	19.0	-1.36

We only analysed the case involving the Ag(100) surface in a high coverage situation for some specific sites: H_{37}, T, and H. Counterions, POM and silver layer in contact with the POM were allowed to relax in all calculations. Our results show that the presence of K^+ does not significantly alter the relative orientation of the POM with respect to our previous results. However, we do observe a change in the relative energies, with the T active site being preferred instead of H_{37}. The energy range also increases to 19.0 kcal·mol^{-1}. In addition, counterions prefer to be found close to O_b triads, as observed in the non-adsorbed POM, with the exception of H_{37} in which both arrangements are nearly degenerated.

Another advantage of considering counterions is that we can now evaluate meaningful adsorption energies, which are reported in Table 3.8. When we consider the POM with counterions we are in fact correcting the POM's oxidation state. That is, POM is technically reduced and its charge is compensated for counterions. In this situation, its energetic reference is better than the neutral POM in gas phase and E_{ads} is therefore a better approximation to the interaction energy between the POM and the surface. Adsorption is favoured since the E_{ads} are about -2 eV and their values are comparable to the IBE-a, given in both Table 3.1 and Table 3.3. We can understand that IBE-a seems to be a good approximation for describing the E_{ads} when energetic references are not adequate.

Table 3.9 Average distances (in Å) for top active sites of $K_4SiW_{12}O_{40}$ on Ag(100) surface. POM reference distances referred to the isolated POM with counterions.

type		$O_b - T_2$	$O_c - T_1$	Reference
Ag[a]	O_b	3.47 – 3.51	3.40 – 3.42	2.43 [b]
	O_c	2.79	2.68	2.23 [b]
	O_d	2.41 – 2.52	2.37 – 2.42	2.06 [b]
	K	3.61	4.00	
Si	Ag	6.23	6.09	4.90 [c]
	O_a	1.64 – 1.65	1.64 – 1.65	1.64
O_a	W_u	2.33 – 2.46	2.37 – 2.43	2.37
	W_e	2.36 – 2.41	2.36 – 2.39	
	W_d	2.29 – 2.40	2.31 – 2.38	
O_b	W_u	1.88 – 1.97	1.90 – 1.96	1.94
	W_e	1.92 – 1.96	1.92 – 1.94	
	W_d	1.89 – 1.97	1.89 – 1.96	
	K	2.72 – 2.98	2.80*	
O_c	W_u	1.90 – 1.98	1.93 – 1.97	1.93
	W_e	1.92 – 1.95	1.94 – 1.96	
	W_d	1.90 – 1.97	1.91 – 1.99	
	K	-	2.65 – 3.12	
O_d	W_u	1.72 – 1.75	1.72 – 1.75	1.74
	W_e	1.73	1.73	
	W_d	1.74 – 1.77	1.74 – 1.76	
	K	2.71 – 2.77	2.80 – 3.71	

[a] The four O_d oxygens are placed on-top, as well as the two O_c oxygens. In contrast, the O_b oxygens are placed on the bridge site.
[b] Si-Ag and Ag-O distances are reported for the H_{37} adsorption site in the Ag(100) high coverage situation.
[c] Si-Ag distance is obtained by using X-Ray Specular Reflectivity and Ag-O distances are obtained from extrapolation, considering the restrictions that Si-Ag distance imposes.
* After optimization, K^+ atoms close to the surface moves from the O_c triads to the closest O_b oxygen, which explains this distance value.

We also analysed the role of counterions in the distortion induced by the adsorption. As reflected in Table 3.9 and starting from the top of the table, the heteroatom (Si) is found between 0.5 and 0.7 Å further to the surface with respect to no counterions situation. It is also evident that the Ag-O_x distances have increased by approximately 0.1 Å in all cases. Therefore, in the Ag-O_d-W_d "functional group", since the Ag-O_d bond has gotten weaker, the W_d-O_d bond has become stronger, and thus the W_d-O_d distance has slightly decreased.

The fact that POMs are further from the surface can be easily explained. Counterions correct the overestimated POM oxidant strength and therefore, the interaction between surface and adsorbate becomes weaker. Consequently, the POM has slightly moved away from the surface.

In the model with lacking counterions, the adsorption itself was responsible for the alternating long/short bond arrangement whereas now, the counterions are responsible. The oscillation in bond distances do not reveal any relation to how far from the surface the tungsten atoms are. In fact, all distortions are about the same order.

Counterions are found to be between 2.7 and 3.1 Å from the POM. These divergences depend on whether the counterion is close to the surface or not. Those close to the surface are found at 2.7 – 2.8 Å from the silver surface on a top position and in both cases, close to an O_b oxygen, regardless of the triad where they were firstly placed.

Finally, we analysed the frequencies and simulated the infrared spectra for O_b-T_{20}. Regarding firstly the frequency analysis, as shown in Table 3.10, counterions are not involved in any of the active VNM and they do not influence the regions previously defined. $W_{e/u}$=O_d stretching appears above 870 cm^{-1}; Si-O_a stretches are found between 960 and 890 cm^{-1}; W-O-W stretching are between 920 and 700 cm^{-1}, and bending corresponding to the same moiety appears below 500 cm^{-1}. However, the region that corresponds to the Ag-O_d-W_d stretch found between 950 and 850 cm^{-1}. The movement that governs the region is, in fact, the W-O stretching so the stronger the bond becomes, the higher the frequency of the corresponding stretch.

Table 3.10 Selected vibrational frequencies (ω) in cm^{-1}, associated intensities (I), in $km \cdot mol^{-1}$, and assignments for $K_4SiW_{12}O_{40}$ (O_b) adsorbed on Ag(100) for high coverage situation in T_{20} site.

ω	I	Assignment
993	56	$\upsilon_s(W_u{=}O_d)$
963	7	$\upsilon_s(W_e{=}O_d) + \upsilon_s(Si{-}O_a)$
957	5	$\upsilon_s(W_e{=}O_d)$
932	11	$\upsilon_s(W_u{=}O_d) + \upsilon_s(Si{-}O_a)$
920	27	$\upsilon_s(Ag{-}O_d{-}W_d) + \upsilon_s(W_u{=}O_d)$; $\upsilon_s(W_d{-}O_{b/c}{-}W_e)$
890	7	$\upsilon_s(Si{-}O_a)$; $\upsilon_{as}(Ag{-}O_d{-}W_d)$
867	25	$\upsilon_s(Ag{-}O_d{-}W_d) + \upsilon_s(W_x{-}O_{b/c}{-}W_y)$; $\upsilon_s(W_u{=}O_d)$
785	7	$\upsilon_{as}(W_x{-}O_{b/c}{-}W_y)$
694	25	$\upsilon_{as}(W_x{-}O_{b/c}{-}W_y)$
514	5	$\delta(W_x{-}O_c{-}W_y)$

υ_s = symmetric stretching; υ_{as} = asymmetric stretching; δ = bending.

[a] x and y labels mean that no specific tungsten atom is involved in the movement.

Although the regions are not significantly affected by the presence of counterions, the shape of the spectrum is affected dramatically. As shown in Figure 3.11, the intensity of the entire spectrum is significantly lower than in the previous model. The intensity is related to the dipolar moment of the molecule. The system here does not present a strong dipolar moment, as it was when counterions where not considered, spectrum intensity is clearly affected. Besides, the most intense band appears at 1000 cm^{-1} instead of 800 cm^{-1}, and the second most intense peak appears at 920 cm^{-1}.

After all this analysis carried out considering counterions, neither the active site, the most representative distances, nor the IR spectrum are consistent with the experimental data reported by Gewirth and co-workers. We agree that introducing K atoms allows us correcting the issue we had with the charge of the POM. However, in order to properly describe the charge, solvent molecules and counterions should be considered explicitly.

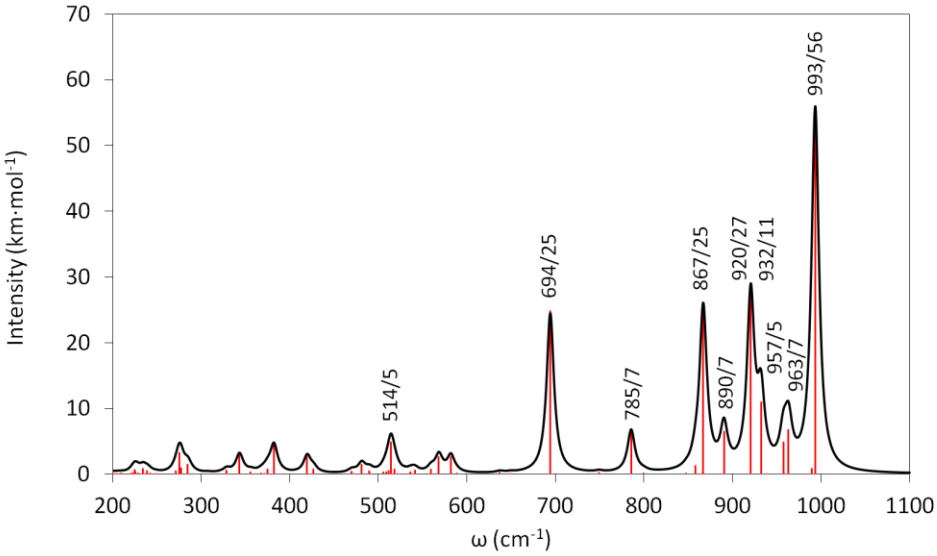

Figure 3.11 Simulated infrared spectrum for $K_4SiW_{12}O_{40}$ adsorbed on Ag(100) surface for T_{20} active site.

3.8. Conclusions

In this chapter, we have proposed different models for computing the adsorption of $SiW_{12}O_{40}$ on Ag(100) and Ag(111) surfaces, considering different unit cells (or coverage situations). Our analysis in this chapter is only concerned with the structural and spectroscopic parameters. We distinguish our results depending on the model we employed: namely whether or not counterions were considered.

> Not considering counterions

- ✓ We have been able to reproduce the adsorption site for the unit cell that involved a high coverage situation and corrected the proposed orientation angle, considering the POM-POM repulsion.
- ✓ For those superstructures with no experimental information, we have proposed the active site where the POM could be adsorbed.
- ✓ We have discarded the possibility of finding the α-Keggin anion adsorbed *via* its proper C_3 symmetry axis.

- ✓ Upon the adsorption, terminal POM terminal oxygen atoms establish covalent bonds with the silver surface atoms. This induces a decrease in W=O bond order, and the shift of the corresponding bands in the infrared spectrum.
- The adsorption also induces a structural rearrangement, reflected in the long/short W-O bond alternating sequence, which is more evident in the region close to the surface.
- ✓ We have confirmed that the adsorption on low energetic sites represent local minima on the Potential Energy Surface.
- ✓ We simulated the infrared spectra for the sites where vibrations were determined previously, and adequately reproduced the experimental spectrum.
- ✘ We were unable to reproduce the region of the spectra between 900 and 1000 cm^{-1}, as this region is heavily influenced by the counterions.

> Considering counterions

- ✓ We have corrected the overestimated oxidant strength of the neutral POM.
- ✘ We were unable to reproduce the adsorption site for Ag(100) in the high coverage situation.
- ✘ We could not reproduce both the Ag-O and the Si-Ag distances reported in the work of A. A. Gewirht.
- ✘ We could not reproduce the infrared spectra while considering explicit counterions in the model.

In light of these results, it can be concluded that our model is unable to adequately reproduce experimental data when counterions are explicitly included in the representation of an adsorbed POM. On the other hand, the model with lacking counterions seems to work rather well for reproducing the structural data.

Appendix Chapter 3
Infrared studies on silver surfaces

Appendix 3.1 Average distances (in Å) for the C_3 orientation modes on Ag(100) and Ag(111) surfaces.

type		Ag(100) C_3	Ag(111) C_3
Ag[a]	O_b	-	-
	O_c	2.25 – 2.84	2.27 – 2.30
	O_d	2.29 – 2.46	2.31 – 2.39
Si	Ag	5.88	5.89
	O_a	1.63 – 1.70	1.62 – 1.71
O_a	W_u	-	-
	W_e	2.36	2.36
	W_d	2.32	2.31
O_b	W_u	1.92	1.92
	W_e	1.92 – 2.05	1.92 – 2.05
	W_d	1.83	1.83
O_c	W_u	1.97	1.97
	W_e	1.89 – 1.93	1.88 – 1.93
	W_d	2.02	2.02
O_d	W_u	1.71	1.71
	W_e	1.72	1.72
	W_d	1.82	1.82

[a] The divergence in these distances is a result of where oxygen atoms are placed onto the surface. For Ag(100), O_d are placed 2 on bridge and 1 on top and for O_c, 1 on-top and 2 on hollow whereas for Ag(111) there are 2 O_d on bridge and 1 on fcc and 3 O_c on-top.

Appendix 3.2 Selected vibrational frequencies (ω) in cm^{-1}, associated intensities (I) $km \cdot mol^{-1}$ and assignments for $SiW_{12}O_{40}$ adsorbed on Ag(111) in different sites, adsorption modes and coverages. In order, B_{22}, hcp and top_{30} sites regarding the adsorption in high coverage situation, followed by B_0 and C_3 deposition orientation for low coverage situation. For all frequency tables, x and y labels related to tungsten atoms mean that no specific tungsten atom is involved in the movement.

- *B_{22} – Ag(111) high coverage situation*

ω	I	Assignment
1011	11	$\upsilon_{as}(W_u=O_d)$
1011	23	$\upsilon_{as}(W_u=O_d)$
1002	106	$\upsilon_s(W_{eq}=O_d)$; $\upsilon_s(W_{eq}=O_d)$; $\upsilon_{as}(Si\text{-}O_a)$
1001	31	$\upsilon_s(W_{eq}=O_d)$; $\upsilon_s(W_{eq}=O_d)$
940	228	$\upsilon_{as}(Si\text{-}O_a)$; $\upsilon_{as}(W_{eq}\text{-}O_d)$
916	44	$\upsilon_{as}(W_x\text{-}O_{b/c}\text{-}W_y)$; $\upsilon_{as}(Si\text{-}O_a)$
881	72	$\upsilon_s(W_x\text{-}O_{b/c}\text{-}W_y)$; $\upsilon_{as}(Si\text{-}O_a)$
851	10	$\upsilon_s(Si\text{-}O_a)$; $\upsilon(W_x\text{-}O_{b/c}\text{-}W_y)$
815	254	$\upsilon_s(Si\text{-}O_a)$; $\upsilon(W_x\text{-}O_{b/c}\text{-}W_y)$
805	231	$\upsilon_s(Ag\text{-}O_d\text{-}W_d)$
518	22	$\delta(W_x\text{-}O_c\text{-}W_y)$
483	16	$\delta(W_d\text{-}O_c\text{-}W_d)^a$; $\delta(Si\text{-}O_a)$
378	46	$\delta(W_x\text{-}O_{b/c}\text{-}W_y)$

υ_s = symmetric stretching; υ_{as} = asymmetric stretching; δ = bending.

[b] This movement causes $\upsilon(Ag\text{-}O_c)$.

- *Hcp_7 – Ag(111) high coverage situation*

ω	I	Assignment
1007	23	$\upsilon_s(W_{e/u}=O_d)$
1006	27	$\upsilon_{as}(W_{e/u}=O_d)$
995	69	$\upsilon_s(W_e=O_d)$; $\upsilon_s(W_d-O_b-W_e)$; $\upsilon_s(Si-O_a)$
994	10	$\upsilon_{as}(W_{e/u}=O_d)$; $\upsilon_s(Si-O_a)$
943	24	$\upsilon_{as}(Si-O_a)$; $\upsilon_{as}(W_u=O_d)$
940	146	$\upsilon_{as}(Si-O_a)$; $\upsilon_s(W_d-O_{b/c}-W_e)$
917	27	$\upsilon_s(W_{e/u}-O_{b/c}-W_{d/u})$; $\upsilon_s(Si-O_a)$; $\upsilon_s(Ag-O_d-W_d)$
887	23	$\upsilon_s(W_{e/u}-O_{b/c}-W_{d/u})$; $\upsilon_s(Si-O_a)$
883	57	$\upsilon_s(W_{e/u}-O_{b/c}-W_{d/u})$; $\upsilon_s(Si-O_a)$
838	225	$\upsilon_s(Ag-O_d-W_d)$; $\upsilon_s(Si-O_a)$; $\upsilon_s(W_x-O_{b/c}-W_y)$
826	43	$\upsilon_{as}(W_x-O_c-W_y)$; $\upsilon_{as}(Si-O_a)$
817	117	$\upsilon_{as}(W_x-O_{b/c}-W_y)$; $\upsilon_s(Si-O_a)$
783	61	$\upsilon_s(Ag-O_d-W_d)$; $\upsilon_{as}(W_x-O_{b/c}-W_y)$
782	26	$\upsilon_{as}(Ag-O_d-W_d)$; $\upsilon_{as}(W_x-O_{b/c}-W_y)$; $\upsilon_{as}(Si-O_a)$
686	11	$\upsilon_{as}(Ag-O_d-W_d)$; $\upsilon_{as}(W_x-O_{b/c}-W_y)$
380	44	$\delta(W_d-O_c-W_e)$; $\delta(W_{e/u}-O_{b/c}-W_{e/u})$

- *T_{30} – Ag(111) high coverage situation*

Ω	I	Assignment
1013	15	$\upsilon_s(W_{e/u}=O_d)$
1003	96	$\upsilon_s(W_{e/u}=O_d)$
937	210	$\upsilon_s(W_e=O_d)$; $\upsilon_s(W_d-O_{b/c}-W_e)$; $\upsilon_s(Si-O_a)$
917	17	$\upsilon_s(W_x-O_{b/c}-W_y)$
882	63	$\upsilon_s(Si-O_a)$; $\upsilon_s(W_x-O_b-W_y)$
850	15	$\upsilon_s(Si-O_a)$; $\upsilon_s(W_x-O_c-W_y)$; $\upsilon_s(Ag-O_d-W_d)$
814	117	$\upsilon_s(Si-O_a)$; $\upsilon_s(W_x-O_c-W_y)$
806	273	$\upsilon_s(Ag-O_d-W_d)$
518	12	$\delta(W_u-O_c-W_u)$; $\delta(W_d-O_c-W_e)$
495	16	$\delta(Si-O_a)$; $\delta(W_d-O_c-W_d)$;[a] $\delta(W_x-O_c-W_y)$
379	41	$\delta(W_x-O_{b/c}-W_y)$

υ_s = symmetric stretching; υ_{as} = asymmetric stretching; δ = bending.

[a] This movement causes $\upsilon(Ag-O_c)$.

- *B_0 – Ag(111) low coverage situation*

ω	I	Assignment
1011	16	$\upsilon_s(W_u{=}O_d)$
999	73	$\upsilon_s(W_{u/e}{=}O_d)$
995	18	$\upsilon_{as}(W_{u/e}{=}O_d)$
988	96	$\upsilon_{as}(W_{u/e}{=}O_d)$
987	91	$\upsilon_{as}(W_{u/e}{=}O_d)$
933	445	$\upsilon_s(Si\text{-}O_a)$; $\upsilon_{as}(W_e{=}O_d)$
908	66	$\upsilon_s(W_{d/u}\text{-}O_{b/c}\text{-}W_e)$
882	62	$\upsilon_s(Si\text{-}O_a)$; $\upsilon_s(W_{d/u}\text{-}O_b\text{-}W_e)$
848	73	$\upsilon_s(Si\text{-}O_a)$; $\upsilon_s(W_{d/u}\text{-}O_c\text{-}W_e)$
881	71	$\upsilon_s(Ag\text{-}O_d\text{-}W_d)$; $\upsilon_s(Si\text{-}O_a)$; $\upsilon_s(W_{d/e}\text{-}O_c\text{-}W_e)$
798	1206	$\upsilon_s(Ag\text{-}O_d\text{-}W_d)$; $\upsilon_{as}(W_{d/u}\text{-}O_{b/c}\text{-}W_u)$
530	16	$\delta(Si\text{-}O_a)$; $\delta(W_d\text{-}O_c\text{-}W_e)$
522	26	$\delta(W_u\text{-}O_c\text{-}W_{u/e})$
464	35	$\delta(Si\text{-}O_a)$; $\delta(W_d\text{-}O_c\text{-}W_d)$
379	17	$\omega(W_u\text{-}O_c\text{-}W_u)$; $\delta(W_{u/e}\text{-}O_{b/c}\text{-}W_{d/e})$
376	90	$\delta(W_x\text{-}O_{b/c}\text{-}W_y)$

- *C_3 – Ag(111) low coverage situation*

ω	I	Assignment
1012	121	$\upsilon_s(W_u{=}O_d)$
992	93	$\upsilon_s(W_e{=}O_d)$
917	380	$\upsilon_s(W_d\text{-}O_b\text{-}W_e)$; $\upsilon_s(Si\text{-}O_a)$
836	741	$\upsilon_s(W_e\text{-}O_c\text{-}W_u)$; $\upsilon_s(Si\text{-}O_a)$
765	670	$\upsilon_s(Ag\text{-}O_d\text{-}W_d)$; $\upsilon_s(W_d\text{-}O_b\text{-}W_e)$; $\upsilon(Si\text{-}O_a)$
738	120	$\upsilon_s(Ag\text{-}O_d\text{-}W_d)$; $\upsilon(Si\text{-}O_a)$
504	73	$\delta(W_d\text{-}O_c\text{-}W_d)$;[a] $\delta(Si\text{-}O_a)$
461	36	$\delta(W_{d/e}\text{-}O_c\text{-}W_{d/e})$; $\delta(Si\text{-}O_a)$
372	19	$\delta(W_e\text{-}O_{b/c}\text{-}W_u)$; $\delta(W_u\text{-}O_b\text{-}W_u)$
370, 368, 367[b]	27, 22, 19	$\delta(W_{d/e}\text{-}O_{b/c}\text{-}W_{u/e})$; $\delta(W_u\text{-}O_b\text{-}W_u)$
359	81	$\delta(W_d\text{-}O_b\text{-}W_e)$; $\delta(W_e\text{-}O_{b/c}\text{-}W_e)$

υ_s = symmetric stretching; υ_{as} = asymmetric stretching; δ = bending; ω = wagging.

[a] This movement causes $\upsilon(Ag\text{-}O_c)$

[b] These frequencies all have the same assignment

Chapter 3
Infrared studies on silver surfaces

[1] (a) D. E. Katsoulis, *Chem. Rev.* **1998**, *98*, 359-388; (b) H. N. Miras, J. Yan, D.-L. Long, L. Cronin, *Chem. Soc. Rev.* **2012**, *41*, 7403-7430; (c) A. Proust, B. Matt, R. Villanneau, G. Guillemot, P. Gouzerh, G. Izzet, *Chem. Soc. Rev.* **2012**, *41*, 7605-7622.

[2] (a) M. H. Ge, A. A. Gewirth, W. G. Klemperer, C. G. Wall, *Pure Appl. Chem.* **1997**, *69*, 2175-2178; (b) M. H. Ge, B. X. Zhong, W. G. Klemperer, A. A. Gewirth, *J. Am. Chem. Soc.* **1996**, *118*, 5812-5813.

[3] (a) B. Keita, L. Nadjo, *Surf. Sci. Lett.* **1991**, *254*, L443-L447; (b) S. Dong, B. Wang, *Electrochim. Acta* **1992**, *37*, 11-16; (c) B. A. Watson, M. A. Barteau, L. Haggerty, A. M. Lenhoff, R. S. Weber, *Langmuir* **1992**, *8*, 1145-1148; (d) B. Keita, L. Nadjo, *J. Electroanal. Chem.* **1993**, *354*, 295-304; (e) S. Liu, Z. Tang, Z. Shi, L. Niu, E. Wang, S. Dong, *Langmuir* **1999**, *15*, 7268-7275; (f) L. Cheng, S. Dong, *J. Electrochem. Soc.* **2000**, *147*, 606-612; (g) J.-P. Tessonnier, S. Goubert-Renaudin, S. Alia, Y. Yan, M. A. Barteau, *Langmuir* **2013**, *29*, 393-402.

[4] L. Lee, A. A. Gewirth, *J. Electroanal. Chem.* **2002**, *522*, 11-20.

[5] L. Lee, J. X. Wang, R. R. Adžić, I. K. Robinson, A. A. Gewirth, *J. Am. Chem. Soc.* **2001**, *123*, 8838-8843.

[6] C. M. Teague, X. Li, M. E. Biggin, L. Lee, J. Kim, A. A. Gewirth, *J. Phys. Chem. B* **2004**, *108*, 1974-1985.

[7] J. P. Perdew, J. A. Chevary, S. H. Vosko, K. A. Jackson, M. R. Pederson, D. J. Singh, C. Fiolhais, *Phys. Rev. B: Condens. Matter* **1992**, *46*, 6671-6687.

[8] P. E. Blöchl, *Phys. Rev. B: Condens. Matter* **1994**, *50*, 17953-17979.

[9] H. J. Monkhorst, J. D. Pack, *Phys. Rev. B: Condens. Matter* **1976**, *13*, 5188-5192.

[10] B. Martorell, A. Clotet, *J. Phys. Chem. C* **2008**, *113*, 950-964.

[11] Y. Wang, L. L. Jia, W. N. Wang, K. N. Fan, *J. Phys. Chem. B* **2002**, *106*, 3662-3667.

[12] H. An, Y. Li, E. Wang, D. Xiao, C. Sun, L. Xu, *Inorg. Chem.* **2005**, *44*, 6062-6070.

[13] Y.-Q. Lan, S.-L. Li, K.-Z. Shao, X.-L. Wang, Z.-M. Su, *Dalton Trans.* **2008**, 3824-3835.

[14] L. K. Yan, X. Lopez, J. J. Carbo, R. Sniatynsky, D. C. Duncan, J. M. Poblet, *J. Am. Chem. Soc.* **2008**, *130*, 8223-8233.

[15] C. Rocchiccioli-Deltcheff, M. Fournier, R. Franck, R. Thouvenot, *Inorg. Chem.* **1983**, *22*, 207-216.

Chapter 4
Solvated POM on silver surface

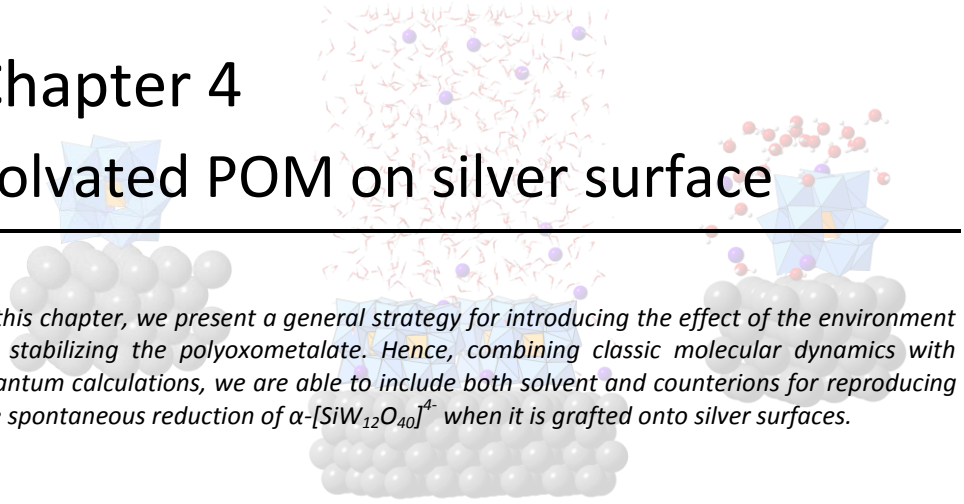

In this chapter, we present a general strategy for introducing the effect of the environment for stabilizing the polyoxometalate. Hence, combining classic molecular dynamics with quantum calculations, we are able to include both solvent and counterions for reproducing the spontaneous reduction of α-$[SiW_{12}O_{40}]^{4-}$ when it is grafted onto silver surfaces.

UNIVERSITAT ROVIRA I VIRGILI
COMPUTATIONAL MODELLING OF POLYOXOMETALATES ADSORBED ON METALLIC SURFACES
Xavier Aparicio Anglès
Dipòsit Legal: T. 1525-2013

4.1. Introduction

For ionic species, the presence of surrounding field is crucial for guaranteeing their stability, as the field lowers orbital energies. Because of that, polyoxometalates are only stable in condensed phases, like in solution or solid state.[1] Interactions between solvent and solute as well as crystal field in solid state are responsible of this stabilization.

From a computational point of view, the presence of the solvent involves different aspects. One of them is the aforementioned fact that the presence of solvent corrects the orbital energies, yet not all orbitals must be stabilized in the same way. In order to understand it, the relation q/m, in which q is the charge of the POM and m the number of metallic centers, becomes an important tool.[2]

When q/m relation is low, *i.e.* below 0.8, this stabilization hardly alters the ordering of the Molecular Orbitals (MO). As a consequence, those properties derived from this order (electronic structure, basicity, geometric parameters, etc.) can be well described in gas phase.[3] If this relation is higher than this 0.8, aside from correcting the energies, the ordering is also corrected when the environment is considered.[2, 4] q/m relation is more accurately described in Chapter 5.

On the other hand, for describing reactivity or electrochemical behavior of POMs, both MO ordering and energies must be corrected introducing solvent effects.[3b, 5] As a matter of fact, they were not properly described until implementation of these solvent models.

Although in past years solvent modeling proved difficult, nowadays these effects are included routinely in calculations. Two of the most important methods for describing the solvent are the well-known *conductor-like screening model* (COSMO),[6] and the *Polarizable Continuum Model* (PCM).[7] The fundamental idea behind both methods is to define a cavity around the atoms. Outside this cavity, we can modify the dielectric constant in order to simulate the effect of the solvent and counterions. Regarding those computational packages that work with periodic boundary conditions, introduction of this methodology is extremely recent and only few works have been published at the moment.[8]

Miró *et al.*[9] proved that the effect of these methodologies is comparable to include both explicit solvent molecules and the corresponding counterions. By

means of Molecular Dynamics Simulations, they obtained a random distribution of water molecules and counterions surrounding a POM, from which they calculated the electronic structure of the whole system. Results were unequivocal; COSMO was able to reproduce the electronic structure obtained by the aforementioned calculations. These results also suggested that if it is not possible to include solvent effects by means of COSMO or other similar strategies, explicit water molecules and counterions could be used in order to model the environment.

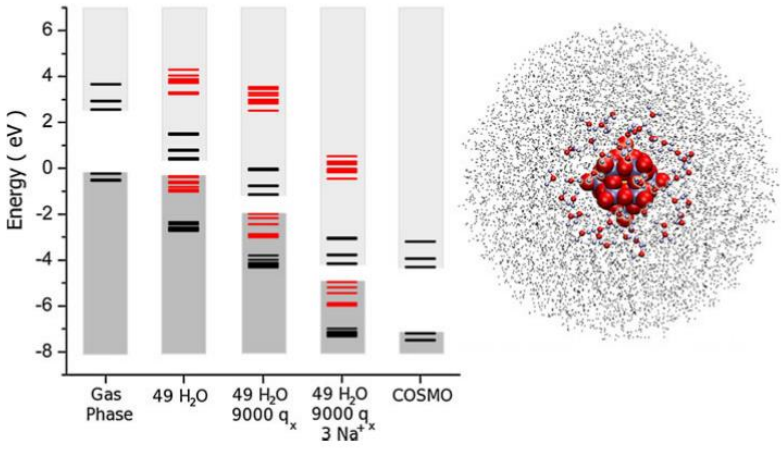

Figure 4.1 Energies for the highest occupied and lowest empty levels for different POM–water models. Black levels of the Keggin anion; red levels of the water molecules; dark grey occupied levels; light grey empty levels. The right-hand view shows the Keggin anion surrounded by explicit water: the first solvation sphere and the point charges. Reproduced from ref. 9 with permission.

4.2. Motivation and Objectives

Besides reporting both structural and spectroscopic data about the adsorption of $[\alpha\text{-}SiW_{12}O_{40}]^{4-}$ on a silver surface, the group of A. A. Gewirth also conducted an exhaustive electrochemical study regarding this system. However, the results obtained were controversial. Cyclic voltammagrams concerning adsorbed SiW_{12} show the absence of the voltammetric wave at -0.2 V *vs.* Ag/AgCl electrode.[10] Several hypotheses exist to explain this fact. First, after several cycles, the POM could have been destroyed, passivating the surface. Another hypothesis states that this voltammetric wave could have been anodically shifted beyond the

potential of the Ag dissolution. On the other hand, it has been pointed out that the absence of this wave could be attributed to the spontaneous reduction of the adsorbed POM.[10a] Off all the possibilities, the picture that seems to be more probable is the latter, concerning the spontaneous reduction. Unfortunately, neither of these possibilities could be experimentally determined. It is at this point that computational modeling of the adsorbed POM can help answering this question.

The inclusion of solvent in our model is then necessary. The correct description of charge transfer requires the correct placement of the POM's orbitals. However, VASP has not implemented any package that allows the inclusion of solvation effects by changing the environment's dielectric constant. Consequently, the only option that we have is to explicitly introduce both the solvent and counterions in the calculations.

Hence, this chapter is devoted to improving the model regarding the POM adsorption on metal surface by introducing both solvent and counterions. For obtaining the distribution of water molecules surrounding the POM, as well as the counterion's disposition, we will use Classic Molecular Dynamic calculations. After analyzing counterion behaviour, we will obtain new structures from which we will calculate the electronic structure of the adsorbed POM and thus determine whether spontaneous reduction has occurred or not.

Hence, the objectives for this chapter are to:

- ✓ Design a strategy for introducing both water and counterions into our calculations.
- ✓ Analyze how the counterions behave in the presence of adsorbed POMs.
- ✓ After including the environment in our calculations, determine the electronic structure of the adsorbed POM on a silver surface.
- ✓ Conclude if the POM is spontaneously reduced when it is adsorbed on the silver surface or not.

4.3. Computational details

Molecular dynamic calculations initial configurations were set up using Packmol code.[11] We carried out three independent production runs in which both surface

and polyoxometalate were frozen. Water molecules were described using the rigid TIP3P model.[12] The electrostatic contributions were determined using the Ewald summation in the reciprocal space that was described following a 6x6x12 scheme with a convergence factor of 0.309 $Å^{-1}$. Short-range interactions were described using Lennard Jones potential, whose parameters were obtained from the literature[13] and the crossed terms calculated using the Lorentz-Berthelod mixing rules.[14] For both electrostatic and Lennard Jones potentials, the cut off was set at 0.24 Å. Finally, all simulations were carried out under the Canonical Ensemble (NVT), rebalancing the temperature each 0.01 ps using the Nosé-Hoover thermostat.[15] Equilibration and production runs were performed using a time step of 1 fs, lasting 300 ps for equilibration and 20 ns for each production run.

The electronic structure of the adsorbed $[\alpha\text{-}SiW_{12}O_{40}]^{4-}$ including solvent and counterions was computed using VASP to self-consistency using the Blocked Davidson Iteration Scheme (DAV)[16] with a convergence parameter of $1 \cdot 10^{-6}$ eV. A 3x3x1 Monkhorst Pack Scheme was used for determining the k-points mesh in the reciprocal space.[17] Finally, from the charge density, Bader AIM charges were obtained using the Henkelman algorithm.[18]

4.4. Electronic structure of $SiW_{12}O_{40}$ on silver surfaces

The Fermi Level (E_F) is the frontier that determines which bands are filled with electrons and which are empty. Therefore, if we are dealing with the possibility of a spontaneous reduction, POM LUMO orbitals should be placed below to this level.

If we only consider the SiW_{12} and the surface, the Density of States (DOS) displayed in Figure 4.2.a) indicated that the system is conductor, since no discontinuity was observed near E_F, placed at 0 eV. On Figure 4.2 from b) to e) we could observe the projections of different orbitals. Figure 4.2 b) and c), the projection of silver *d* orbitals, *i.e.* Ag(d) band, revealed that conduction takes place through silver. Regarding POM bands, O(p) was at -1.64 eV, below the E_F, whereas W(d) was 1.50 eV above. These results suggested that we should supply 1.50 eV for placing an electron to the POM, which disagrees with its expected spontaneous reduction.

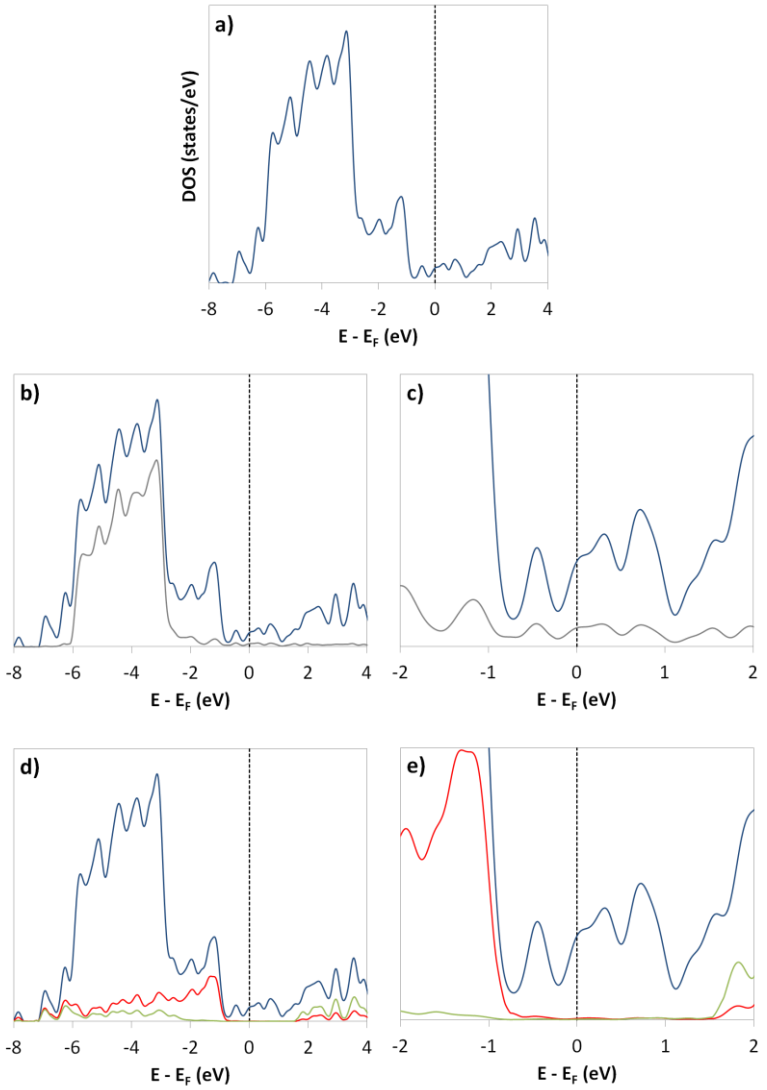

Figure 4.2 a) Density of States, in blue, for $SiW_{12}O_{40}$ on Ag(100); b) Projected Density of States for Ag(d) states, in gray; c) 700% extension of b); d) Projected Density of States for W(d) states, in green; O(p)-POM states, in red; e) 700% extension of d).

Bader AIM charges revealed that POM allocates 2.9 electrons, coming from the first silver layer. These 2.9 electrons are practically allocated in the inner SiO_4 moiety (2.8 electrons) whereas only a residual 0.1 electrons reside in the external $W_{12}O_{36}$ capsule. Although this charge distribution was a clear example of the clathrate formulation of the POM, in which the anionic $[SiO_4]^{4-}$ unit is encapsulated

by the neutral $W_{12}O_{36}$ cage as $[SiO_4]^{4-}@W_{12}O_{36}$,[19] it could not explain the spontaneous reduction of POM.

Interpretation of these results leads to the conclusion that the POM transfers one electron to the surface, indicating that it acts as a reducing agent instead of exhibiting the expected oxidant behavior. However, this conclusion is incongruous with the experimental results that point out the possibility of spontaneous POM reduction.

Indeed, as explained in Chapter 3, this model overestimates the oxidant strength of the POM, which is treated as neutral species in the gas phase. In conclusion, although the model works fairly well in reproducing the geometric and the spectroscopic data, it fails when we try to describe the electronic structure and, consequently, electrochemical properties.

In order to correctly describe the polyoxometalate, environmental effects should be included, both solvent and counterions. However, there is no direct way to introduce both effects. Consequently, we must take the alternative approach of including them explicitly in our calculations. Classic Molecular Dynamic simulations provide a powerful tool for an atomistic description of the solvated systems, concretely for the solvation of polyoxometalates.[13b, 20]

4.5. General description of the strategy

We begin the procedure by selecting one of the arrangements for the adsorbed POM. For convenience, we decided to use the H_{37} active site in the Ag(100) surface obtained from the model lacking counterions. Recall that this site was the lowest in energy for SiW adsorbed on Ag(100) in high coverage situation. We set up an initial geometry with the 2x2 H_{37} unit cell, with the solvent and the counterions. The duplication of the unit cell is mainly devoted to computational requirements, as explained in Chapter 2.

Being faithful to the experiment, we should consider protons as counterions. Instead of that, we took K^+, since it is easier to deal with them. As the system includes four $[\alpha\text{-}SiW_{12}O_{40}]^{4-}$ POMs, silver surface, 16 K^+ as counterions and 461 water molecules to ensure a water density of $\approx 1\ g\cdot cm^{-3}$.

Both surface and POM are frozen during the production run, since the structural parameters were well reproduced with our previous model. We carried out three different production runs that lasted 20 ns, in order to have as many geometries as possible for computing the adsorbed POM with the environment effects.

After analyzing how counterions behave in this system, we extracted various snapshots randomly from the MD simulations. After extraction and division of the different geometries, (see section 4.7) we selected a set of different final configurations that we used for recalculating the electronic structure of the system, now considering the effects of the water molecules and also the counterions.

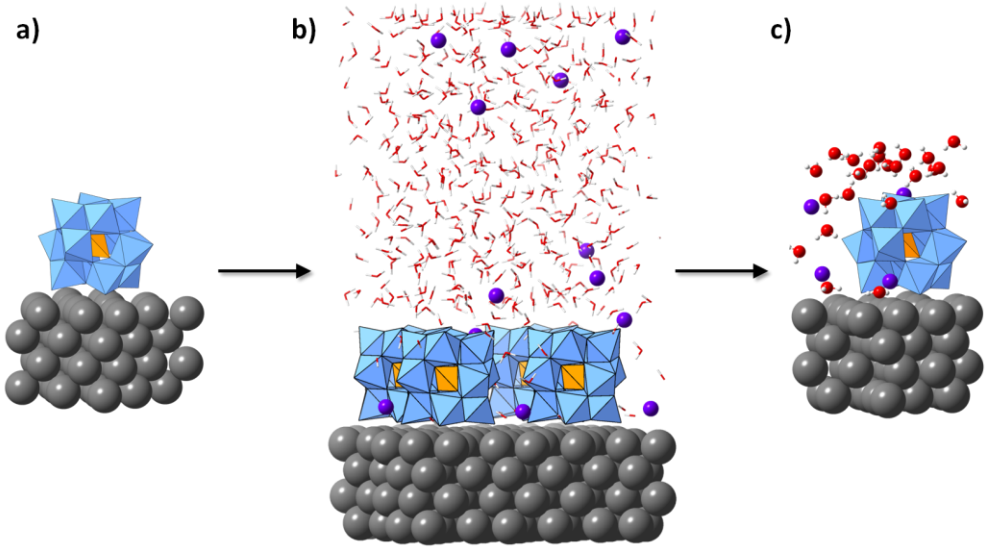

Figure 4.3 Graphical representation of the different steps in our strategy. Firstly, modeling the adsorption of the POM without counterions and solvent (a). Secondly, duplicate the cell and introduce both solvent and counterions (b). After performing molecular dynamics simulation, we extracted different snapshots and cut the cell for calculating the electronic structure of the system (c).

4.6. Counterion behaviour

Once minimization, equilibration and production runs are done, we focus on the counterion behavior with respect to the adsorbed polyoxometalates. We first evaluated the interaction between K^+ and H_2O molecules by means of the Radial

Distribution Function, g(*r*), plotted in Figure 4.4. The first peak is found at 2.75 Å, which is in good agreement with other reported values.[21] In our case, we delimitate the first solvation sphere at 3.65 Å, in which the integration of g(*r*) reveals the presence of 6 water molecules. The number of coordinated water is subject of much discussion in the literature since water molecules are weakly bonded to K^+, and they exchange rapidly between the bulk and, solvation spheres.[21]

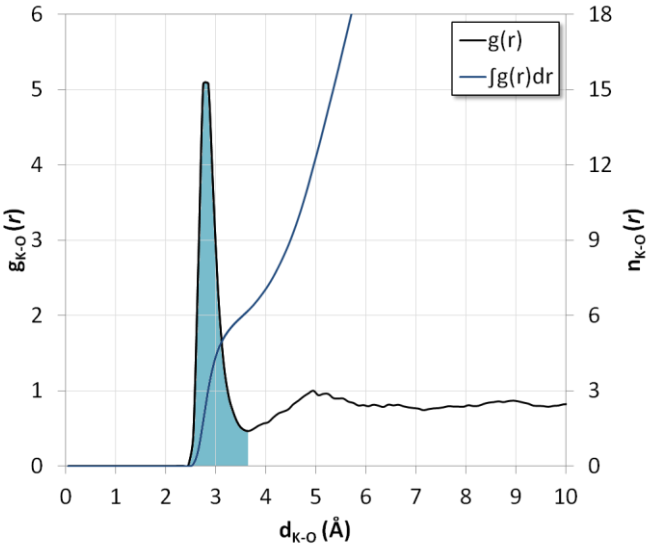

Figure 4.4 Radial distribution function between K^+ and O (water molecules), $g_{K\text{-}O}(r)$ and its integration $n_{K\text{-}O}(r)$. Blue colored region belongs to the first solvation sphere.

Concerning now the interaction between K^+ and adsorbed POMs, we are most interested in how cations move along the z-axis of the cell throughout the simulation. These trajectories are represented in Figure 4.5 (left side), corresponding to the three MD simulations. Notice in this figure that height is represented with respect to the origin of the cell and not with respect to the silver surface, which lies at 6.2 Å from the cell origin.

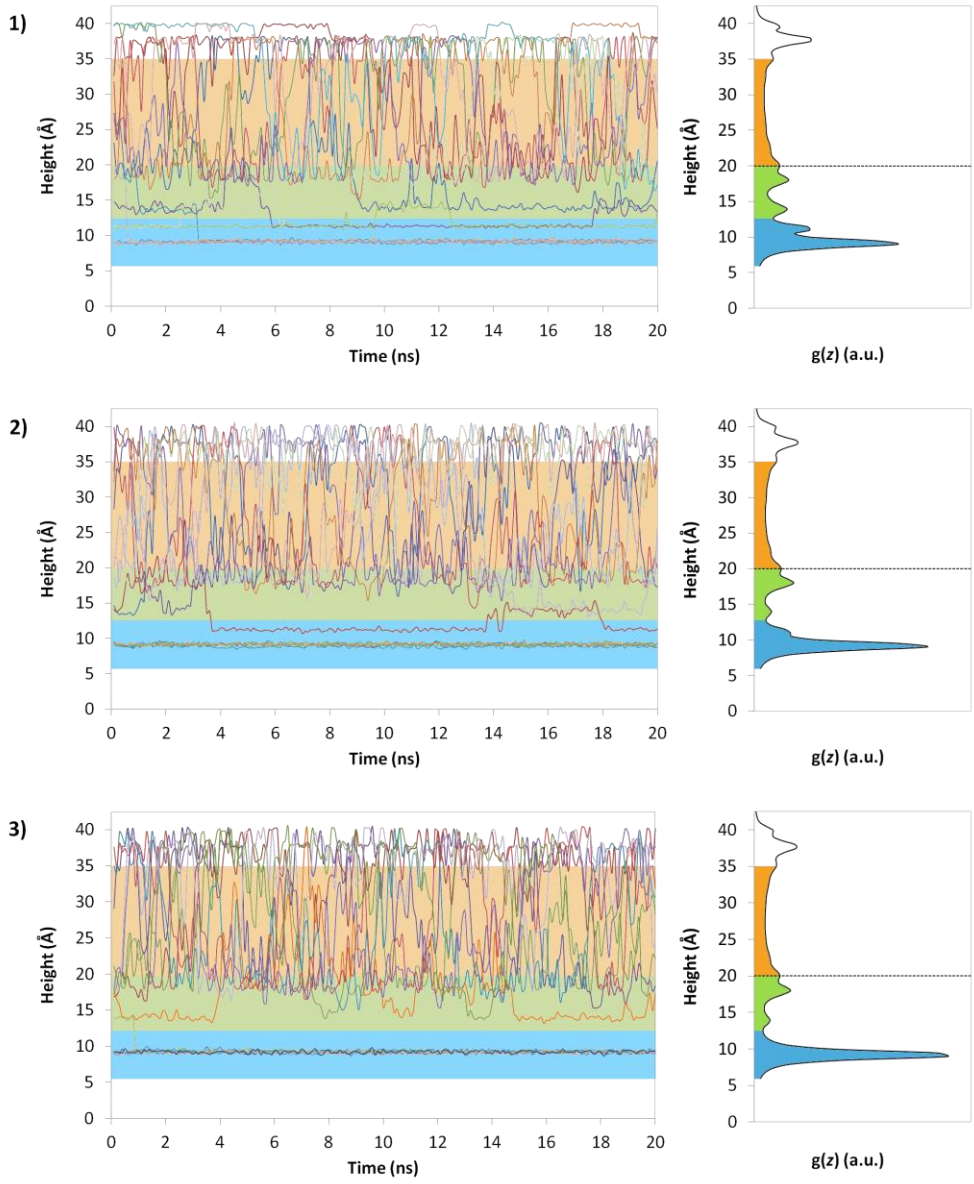

Figure 4.5 Trajectories for all the K^+ ions along the z-axis for a 20-ns-long simulation for production runs 1), 2), and 3). On the right of each trajectory, Linear Distribution Function g(*z*) derived from the trajectories. The different colors represent the different regions: *adsorption region* (blue); *intermediate region* (green); *bulk or bulk region* (orange).

Using the trajectories obtained from the simulations, we obtained the Linear Distribution Function g(*z*) for the K^+ along the z-axis. Both, trajectories and g(*z*) representations show the same behavior for all production runs. Regarding specifically the g(z) function, their analysis allows us to separate the whole cell in three different regions. These regions, represented by different colors in Figure 4.5, are:

- The *adsorption region*, colored in blue, which ranges from the metal surface up to 11.5 Å. In this region, cations are practically immobilized by the POM and the surface. The most intense peak appears at 8,9 Å from the cell origin or 2.7 Å from the surface. K^+ ions adsorbed on silver have been reported to be near 3.35 Å.[22] In this coverage situation, the free space that POMs leave on the surface is rather small and strongly influences the position of counterions.

  Besides being retained along z-axis, K^+ ions are also immobilized in its horizontal plane (x,y). Figure 4.6 a) represents the Surface Distribution Function, g(*x,y*) between 6 and 10 Å in height. g(*x,y*) clearly indicates that K^+ are not allowed to move in this plain. The presence of the surface and POMs, as well as the strong electrostatic interactions in this zone, prevents counterions from escaping into adjacent regions.

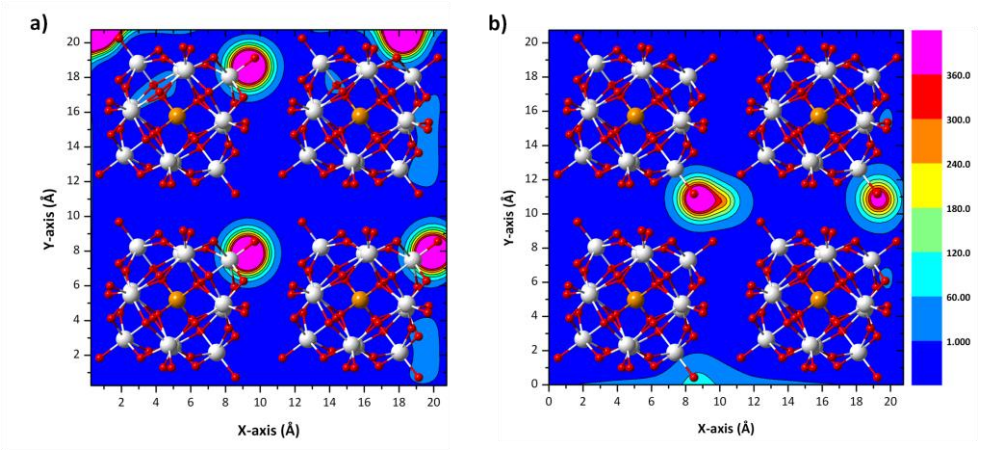

Figure 4.6 Surface Distribution Function g(*x,y*), in arbitrary units, for K^+ atoms in the adsorption region for simulation 1. a) from z_o = 6 Å to z_f = 10 Å; b) from z_0 = 10 Å to z_f = 12.5 Å.

In this region we also include those counterions found at 11.3 Å. This peak, which can be clearly observed in the first and also in the second g(*z*), is associated with K^+ ions linked to the surface *via* water molecules. Actually, they are interacting with the neighboring POM rather than interacting with the surface, but since their mobility is very limited, we include them in the adsorption region (see Figure 4.6 b)

- The *intermediate region*, colored in green, goes from 11.5 to 20 Å. Here, K^+ mobility is larger than in the *adsorption region*. Although not having geometrical constrains, electrostatic interactions keep counterions close to the polyoxometalate, which explain peaks at 13.4, 17.5 and 20.0 Å. These counterions are allowed to exchange with the solution, so this region can be viewed as the first solvation sphere of the POM.
  In Figure 4.7 it is clearly shown that the mobility in the horizontal plane is relatively larger compared to the *adsorption region*, although there are positions close to POMs where K^+ are preferentially found.

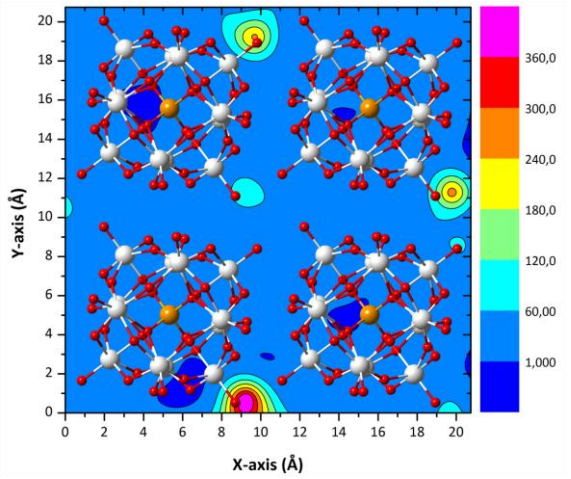

Figure 4.7 Surface Distribution Function g(*x*,*y*) in arbitrary units, for K^+ ions in the intermediate region for simulation 1. The Δz was 7.5 Å, from z_0 = 12.5 Å to z_f = 20 Å.

- The *bulk region*, colored in orange, ranges from 20.0 to 33.5 Å. In this region, K^+ cations move freely and are able to enter and exit the intermediate region for short periods of time.

Finally, at *ca.* 35.0, 37.5, and 39.5 Å there are three additional peaks related to artificial adsorption at the bottom of the replicated cell along the z-axis. These peaks are artifacts of the model since computational requirements bounds to replicate the unit cell along the z-axis. Consequently, the peaks near the bottom surface of the next cell have no real physical meaning, and they are not included in any region. Considering that in the bulk region counterions are not directly interacting with the polyoxometalate, we set the cut-off at 20 Å from the cell origin. That is that all water molecules and counterions placed beyond the cut-off were not considered for computing the electronic structure of the system.

4.7. Electronic structure with embedding effects

The various structures that we used were extracted from the three distinct MD trajectories at randomly chosen simulation times. From each snapshot we took, we had to cut the cell into four parts, because we previously quadruplicated the original H_{37} cell due to computational requirements. In each cell were found between 21 and 23 water molecules. In addition, in order to satisfy the electroneutrality of the system, we imposed that only structures with 4 K atoms will be selected. We also consider the minimum separation between water molecules to be 1 Å.

Geometries were classified depending on the region in which the K atoms were found. In addition, the intermediate region was divided in two regions that correspond to the two peaks found there. Hence, limits of each region and subregion were: *adsorption region* from 6 to 12.5 Å and the *intermediate region* from 12.5 to 15 Å and from 15 to 20 Å. Taking into account these considerations, three types of distributions were defined:

- **(3,1,0)**, with three K^+ cations in the adsorption region and one in the first peak of the intermediate region.
- **(2,2,0)**, with two K^+ in the adsorption region and two more in the first peak of the intermediate region.
- **(2,1,1)**, with two K^+ in the adsorption region, one K^+ in the first peak of the intermediate region and one K^+ in the second peak.

For each distribution we finally included 5 different structures. Then, single DFT calculations were performed and results were averaged per distribution.

4.7.1. Electronic structure

The inclusion of embedding effects only affects the adsorbate, and not the silver surface. Represented in Figure 4.8 are the whole DOS and PDOS for a randomly chosen geometry. It is worth mentioning that all extracted geometries showed almost identical DOS and PDOS. In the case of the Ag(d), its center without solvent effects is placed at -4.46 eV whereas when solvent is included, it remains at approximately the same energy values of -4.38 eV. These results are not unexpected, as the solvent is not directly interacting with the surface but instead with the polyoxometalate and the counterions.

Both the presence of counterions and solvent must be discussed separately. In our calculations, K^+ are considered as neutral atoms and not as formal cations. It is exactly what happened with the polyoxometalate: instead of calculating K^+ as an anion, we calculated it as neutral species. After optimizing the electronic structure, electrons are put in their correct positions. That is potassium atoms lose their extra electron in order to become cations and these electrons are driven into the polyoxometalate, resulting in an anion. Charge transfer lowers the band energy of the polyoxometalate with respect to E_F. As the silver surface is not significantly affected by their presence, we are in fact correcting the position of POM's orbitals against the silver bands. On the other hand and as expected, the presence of the solvent also stabilizes polyoxometalate bands, as it was observed for the free POM using continuum models for simulating the presence of the solvent.[9]

This stabilization can be clearly observed when we compare the position of the W(d) band with and without solvent (see Figure 4.2 and Figure 4.8 e)). When the environment is considered, the front of the band is placed 0.1 eV below E_F indicating that the stabilization of the electronic structure of the POM is about 1.6 eV. Equally, the position of the O(p) band is logically stabilized 1.6 eV as well. W(d) band position found below E_F indicates that this band is accepting electronic density. At this energy, DOS is composed from W orbitals as well as some contribution of the O p orbitals and also from the silver bands. Consequently, the surface is giving this charge to the SiW and, therefore, the POM is spontaneously

reduced when it is in contact with the silver surface. Finally, the bands that correspond to the water molecules are spread over the whole range of energies.

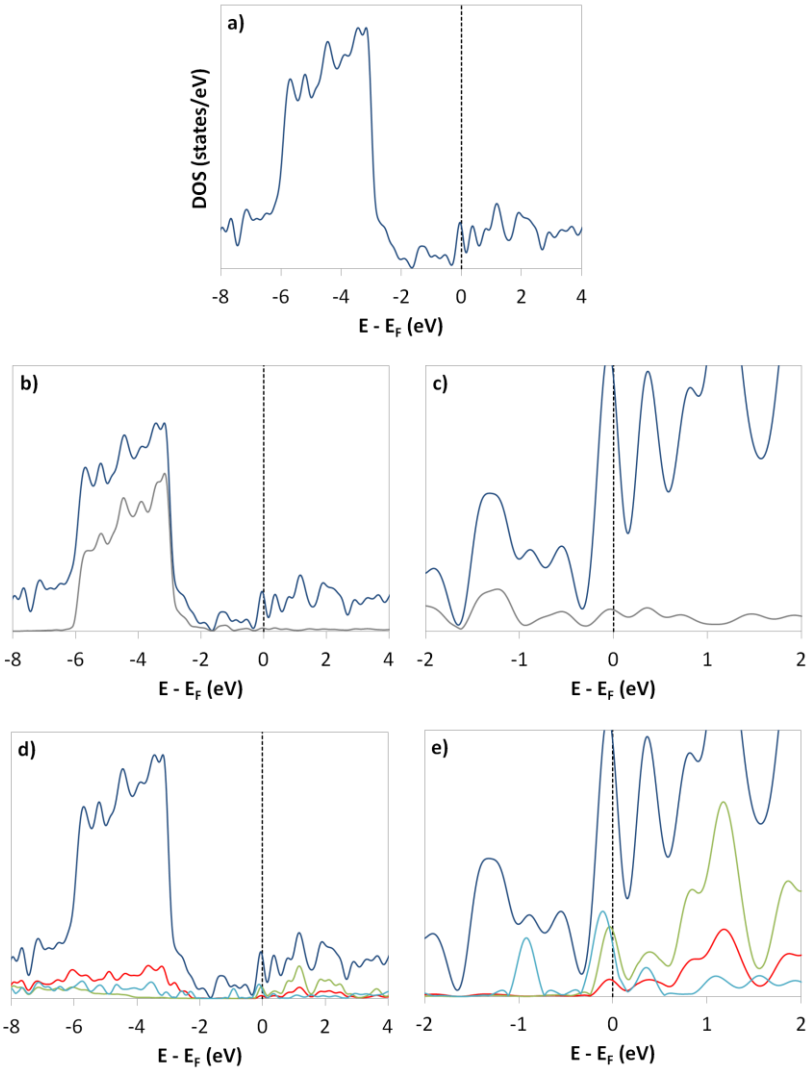

Figure 4.8 a) Density of States, in blue, for $SiW_{12}O_{40}$ on Ag(100) considering both H_2O and K; b) Projected Density of States for Ag(d) states, in gray; c) 700% extension of b); d) Projected Density of States for W(d) states, in green; O(p)-POM states, in red; H_2O (s,p) states, in cyan; e) 700% extension of d).

4.7.2. Bader AIM atomic charges

Charges computed using Bader's Atoms in Molecules approach are listed in Table 4.1. For all the computed structures, the charge of -2.8 e residing on the central SiO_4 unit is identical regardless of whether or not embedding is considered. However, the charge of the external $W_{12}O_{36}$ moiety is strongly modified by the presence of the environment and it differs in each structure. Thus, we analyzed the averaged charges.

In the case where we do not consider the solvent, the external oxotungstate unit only supports -0.1 electrons (e) whereas when the solvent is included, stabilization of the orbitals allows the POM to accept more charge density. In fact, the $W_{12}O_{36}$ subunit accepts -1.5 e, resulting in a global charge of -4.3 e on the polyoxometalate. The silver surface provides an average of around 2 e either considering the environment or not. This fact is in concordance with the electronic structure, since silver band is not affected by the presence of the environment. Among all the silver layers, the one in direct contact with the POM, Ag(1) on Table 4.1, transfers most part of this charge, between 1.8 and 1.9 electrons. Actually, as shown in Figure 4.9, this transfer is a local phenomenon since the greatest charge is found below the polyoxometalate, whereas the part of the surface not in direct contact transfers almost no charge.

Finally, the charge of the counterions corresponds to about 3 electrons, which means that each K atom has a net charge of 0.75 e. The total balance of the system entails that over the 21/23 water molecules reside about 0.8 electrons that should come from the counterions. Analysis of each water molecule does not show any preference for allocating this electron. According to PDOS, in Figure 4.8, below system's E_F, H_2O (sp) band presents a peak close to the W(d) peak. This explains why part of the charge is delocalized on the water bulk.

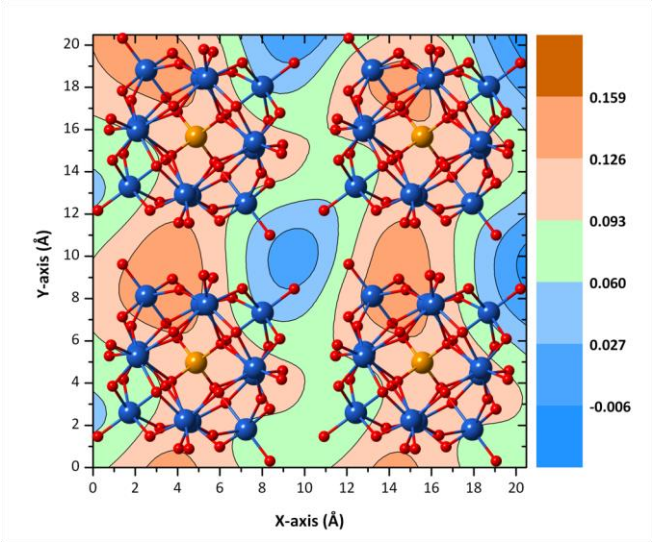

Figure 4.9 Charge distribution map corresponding to the silver layer in direct contact with the surface, Ag(1). In this plot is represented the charge distribution for the 2x2 unit cell, although the charges represented here belong to the 1x1 unit cell.

As the basis set we are using is delocalized on the entire cell, it becomes really hard to localize one electron on a specific atomic set. All water molecules present on the calculations belong to the solvation sphere of the Keggin anion, and the charge transferred to the solvated anion is 5.1 e approximately. This picture suggests that POM is spontaneously reduced after adsorption, which is in accordance with one of the possibilities proposed by Gewirth *et al*.[10a]

It is worth mentioning that Bader AIM charges are only representative when they are described for the fully relaxed system, which is not our case. In addition the Henkelmann algorithm introduces numerical errors when delimits the atomic regions, especially when plane waves are used. Therefore, although the charges we already mentioned would be in fully agreement with the electronic structure of the system, their values must not be considered as an evidence but as a supporting data.[18a]

Despite this, we are confident that the global picture arising from the analysis of Density of States fully agrees with the experiment, thus providing support to the validity of these results. Both the counterions and water molecules are necessary in describing the electronic structure of the system correctly. Previous analysis of

polyoxoanions in aqueous solution have shown that both water molecules and counterions stabilize the solute by roughly 50%.[9]

Table 4.1 Bader AIM charges for $SiW_{12}O_{40}$ on Ag(100) considering environment (water molecules and K) and not (n.e.).

Dist.		ΣH_2O	$SiW_{12}O_{40}$	$W_{12}O_{36}$	SiO_4	ΣK	Ag(1)[a]	Ag(2)[a]	Ag(3)[a]	Ag(4)[a]
	n.e.	-	-2.9	-0.1	-2.8	-	1.8	0.2	0.3	-0.3
(3,1,0)[b]	1	-1.4	-4.4	-1.6	-2.8	3.5	2.2	0.2	0.3	-0.3
	2	-0.7	-4.4	-1.6	-2.8	3.4	1.6	0.1	0.3	-0.2
	3	-1.2	-3.9	-1.1	-2.8	3.3	1.6	0.1	0.3	-0.2
	4	-1.2	-3.9	-1.1	-2.8	3.3	1.6	0.2	0.3	-0.2
	5	-1.4	-4.4	-1.6	-2.8	3.5	2.2	0.2	0.3	-0.3
	av	*-1.4*	*-4.2*	*-1.4*	*-2.8*	*3.4*	*1.8*	*0.2*	*0.3*	*-0.3*
(2,2,0)[b]	6	-0.1	-4.7	-1.8	-2.8	2.7	1.9	0.2	0.3	-0.3
	7	-1.2	-4.4	-1.6	-2.8	3.5	1.9	0.2	0.3	-0.3
	8	-0.1	-4.7	-1.8	-2.8	2.7	1.9	0.2	0.3	-0.3
	9	-0.6	-4.3	-1.5	-2.8	2.8	1.9	0.2	0.3	-0.3
	10	-0.4	-4.1	-1.3	-2.8	2.4	1.9	0.2	0.3	-0.3
	av	*-0.5*	*-4.4*	*-1.6*	*-2.8*	*2.9*	*1.9*	*0.2*	*0.3*	*-0.3*
(2,1,1)[b]	11	-0.7	-4.2	-1.4	-2.8	2.9	1.9	0.1	0.3	-0.3
	12	-0.7	-4.2	-1.4	-2.8	2.9	1.9	0.1	0.3	-0.3
	13	-1.4	-4.1	-1.3	-2.8	3.5	1.8	0.2	0.3	-0.2
	14	-0.8	-4.3	-1.4	-2.8	3.0	1.9	0.1	0.3	-0.3
	15	-0.4	-5.0	-2.2	-2.8	3.4	1.9	0.2	0.3	-0.3
	av	*-0.9*	*-4.4*	*-1.6*	*-2.8*	*3.2*	*1.9*	*0.2*	*0.3*	*-0.3*

[a] Ag(X), where X indicates the silver layer, 1 being the closest to the adsorbate.
[b] Numbers (n_1, n_2, n_3) identify the K^+ ions belonging to adsorption region, intermediate region and solution, respectively (see text for more details).

4.8. Conclusions

In this chapter we have described a general strategy for including environmental effects in the modeling of the polyoxometalate adsorption on metallic surfaces. The inclusion of solvent and counterion is crucial for an adequate description of the electronic structure and thus, the electrochemical properties between silver and the polyoxometalate. By using a Molecular dynamic simulation we have been able to include the environment and obtaining a good description for our model.

- ✓ We have set up a general strategy for including both solvent and counterions for stabilizing the orbitals of the polyoxometalate. The model lacking counterions showed to be adequate for describing the structure of the system. Based on these structures, we included the solvent and the counterions into the system simulating a silver electrode with adsorbed POMs on solution. From these trajectories, we obtained a set of different geometries from which we obtained the electronic structure of the system under the effect of the solvent and the counterions. Indeed, the model has proved to be able to reproduce experimental data reported for $[SiW_{12}O_{40}]^{4-}$ adsorbed on silver electrode.

- ✓ In solution, counterions are distributed in three different regions according to their mobility. Those potassium atoms that are closer to the surface and, therefore, directly interacting with the POMs are not able to exchange with solution. Counterions interacting with the upper part of the POM can exchange with the solution but they are still stuck close to the POM for short periods of time.

- ✓ When the solvent and the counterions are included in calculations, POM orbitals are stabilized with respect to silver band, which shows almost no changes by the presence of solvent. The stabilization of 1.6 eV permits the front of the W(d) band to reach the E_F, and consequently, the band is filled with electrons coming from the surface. Bader AIM charges also reflect the transfer from the surface, although extra charge is delocalized on the water molecules solvating the POM. In conclusion, the polyoxometalate is

spontaneously reduced by the surface after adsorption, which is a validation of our model.

References Chapter 4
Solvated POM on silver surfaces

[1] C. L. Hill, *Chem. Rev.* **1998**, *98*, 1-2.
[2] X. López, J. A. Fernández, S. Romo, J. F. Paul, L. Kazansky, J. M. Poblet, *J. Comput. Chem.* **2004**, *25*, 1542-1549.
[3] (a) A. J. Bridgeman, *Chem. Phys.* **2003**, *287*, 55-69; (b) X. Lopez, C. Bo, J. M. Poblet, *J. Am. Chem. Soc.* **2002**, *124*, 12574-12582; (c) A. Dolbecq, A. Guirauden, M. Fourmigue, K. Boubekeur, P. Batail, M.-M. Rohmer, M. Benard, C. Coulon, M. Salle, P. Blanchard, *J. Chem. Soc., Dalton Trans.* **1999**, *0*, 1241-1248.
[4] X. Lopez, J. A. Fernandez, J. M. Poblet, *Dalton Trans.* **2006**, 1162-1167.
[5] (a) A. Sartorel, M. Carraro, A. Bagno, G. Scorrano, M. Bonchio, *J. Phys. Org. Chem.* **2008**, *21*, 596-602; (b) L. Vilà-Nadal, J. P. Sarasa, A. Rodríguez-Fortea, J. Igual, L. P. Kazansky, J. M. Poblet, *Chemistry – An Asian Journal* **2010**, *5*, 97-104.
[6] (a) A. Klamt, *J. Phys. Chem.* **1995**, *99*, 2224-2235; (b) A. Klamt, V. Jonas, T. Bürger, J. C. W. Lohrenz, *J. Phys. Chem. A* **1998**, *102*, 5074-5085.
[7] S. Miertuš, E. Scrocco, J. Tomasi, *Chem. Phys.* **1981**, *55*, 117-129.
[8] (a) P. Zhang, J. S. Lian, Q. Jiang, *Phys. Chem. Chem. Phys.* **2012**, *14*, 11715-11723; (b) Z. Zuo, W. Huang, P. Han, *Appl. Surf. Sci.* **2012**, *258*, 3364-3367; (c) M. Cossi, *Chem. Phys. Lett.* **2004**, *384*, 179-184; (d) B. Delley, *Mol. Simul.* **2006**, *32*, 117-123.
[9] P. Miró, J. M. Poblet, J. B. Ávalos, C. Bo, *Can. J. Chem.* **2009**, *87*, 1296-1301.
[10] (a) C. M. Teague, X. Li, M. E. Biggin, L. Lee, J. Kim, A. A. Gewirth, *J. Phys. Chem. B* **2004**, *108*, 1974-1985; (b) L. Lee, A. A. Gewirth, *J. Electroanal. Chem.* **2002**, *522*, 11-20.
[11] L. Martínez, R. Andrade, E. G. Birgin, J. M. Martínez, *J. Comput. Chem.* **2009**, *30*, 2157-2164.
[12] W. Jorgensen, *J. Chem. Phys.* **1983**, *79*, 926-935.
[13] (a) H. Heinz, R. A. Vaia, B. L. Farmer, R. R. Naik, *J. Phys. Chem. C* **2008**, *112*, 17281-17290; (b) F. Leroy, P. Miro, J. M. Poblet, C. Bo, J. B. Avalos, *J. Phys. Chem. B* **2008**, *112*, 8591-8599; (c) X. Lopez, C. Nieto-Draghi, C. Bo, J. B. Avalos, J. M. Poblet, *J. Phys. Chem. A* **2005**, *109*, 1216-1222.
[14] M. P. Allen, D. J. Tildesley, *Computer Simulation of Liquids*, Clarendon Press, Oxford, **1989**.
[15] (a) W. G. Hoover, *Phys. Rev. A* **1985**, *31*, 1695-1697; (b) S. Nosé, *Mol. Phys.* **1984**, *52*, 255-268; (c) S. Nosé, *J. Chem. Phys.* **1984**, *81*, 511-519.
[16] (a) G. H. F. Diercksen, S. Wilson, *Methods in Computational Molecular Physics*, Plenum, New York, **1983**; (b) C. Moler, I. Shavitt, *Numerical algorithms in chemistry: algebraic methods. [Workshop, August 9-11, 1978]*, **1978**.
[17] H. J. Monkhorst, J. D. Pack, *Phys. Rev. B: Condens. Matter* **1976**, *13*, 5188-5192.

[18] (a) R. F. W. Bader, *Atom in Molecules: A Quantum Theory*, Oxford University Press, Oxford, **1990**; (b) G. Henkelman, A. Arnaldsson, H. Jonsson, *Comput. Mater. Sci.* **2006**, *36*, 354-360.

[19] J. M. Maestre, X. Lopez, C. Bo, J. M. Poblet, N. Casan-Pastor, *J. Am. Chem. Soc.* **2001**, *123*, 3749-3758.

[20] (a) T. Mitra, P. Miro, A. R. Tomsa, A. Merca, H. Bogge, J. B. Avalos, J. M. Poblet, C. Bo, A. Muller, *Chem.--Eur. J.* **2009**, *15*, 1844-1852; (b) A. Chaumont, G. Wipff, *J. Phys. Chem. C* **2009**, *113*, 18233-18243; (c) A. Chaumont, G. Wipff, *C. R. Chim.* **2012**, *15*, 107-117; (d) A. Chaumont, G. Wipff, *Eur. J. Inorg. Chem.* **2013**, *2013*, 1835-1853.

[21] A. Tongraar, K. R. Liedl, B. M. Rode, *J. Phys. Chem. A* **1998**, *102*, 10340-10347.

[22] A. Ignaczak, *J. Electroanal. Chem.* **2001**, *495*, 160-168.

Chapter 5
Effect of the charge and the metal

This chapter aims to test the strategy previously introduced by comparing different α-Keggin polyoxometalates. Concretely, we analysed how the charge of the adsorbate, as well as the nature of the metal center, affects the final result. The results obtained suggested that in this strategy an optimization of the full system, considering both solvent and counterions, is necessary for a correct description of the electronic structure and charges.

UNIVERSITAT ROVIRA I VIRGILI
COMPUTATIONAL MODELLING OF POLYOXOMETALATES ADSORBED ON METALLIC SURFACES
Xavier Aparicio Anglès
Dipòsit Legal: T. 1525-2013

5.1. Introduction

Keggin polyoxometalates in solution are easily reduced at weakly negative potentials or even slightly positive potentials.[1] This capacity is mainly derived from the electronic structure of the POM, which was revealed by López and coworkers.[2] The occupied orbitals belong to the oxo ligands whereas the unoccupied orbitals are mainly delocalized over the metal centers. Because of this delocalization, reduction hardly alters the geometry of the POM, explaining their facility for being reduced.

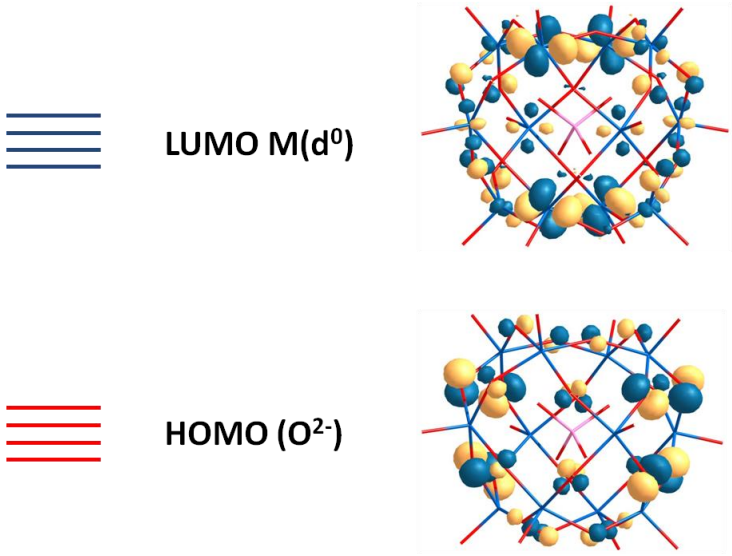

Figure 5.1 Representation for the HOMO and the LUMO orbitals of $[\alpha\text{-}PMo_{12}O_{40}]^{3-}$.

Orbital separation between the oxo and metal band is practically independent of the metal, the size, and the internal heteroatom. On the contrary, they strongly influence the electrochemical behavior of POMs. Consider now two of the main POM families: tungstates (XW) and molybdates (XMo). XMo show lower reduction potentials than XW, which can be related to the metal orbital energies. In this case, molybdenum orbitals are lower in energy, favoring overlap with the oxygen orbitals. One of the main consequences is that the HOMO-LUMO gap (HL gap) is smaller, explaining why molybdates are easier to reduce than tungstates.[3]

Concerning POM charge and size, their influences on the electrochemistry go in opposite directions. POM oxidant strength increases with size, while it decreases with increasing charge. These two last effects can be rationalized by means of the clathrate model. Indeed, polyoxometalates bear similarities to clathrate structures and often are formulated as an anion encapsulated inside a neutral cage. Hence, $[PW_{12}O_{40}]^{3-}$ and $[PMo_{12}O_{40}]^{3-}$ are formulated as $[PO_4]^{3-}@W_{12}O_{36}$ and $[PO_4]^{3-}@Mo_{12}O_{36}$, respectively.[4]

The effect of the size is associated to the external cage in which LUMO orbitals are stabilized as the number of metal atoms, *i.e.* the size, increases. On the contrary, when we include the anion and, therefore, the charge effect, these orbitals are rearranged to higher energies. Hence, the higher the charge is, the more unstable LUMO orbitals become. Both effects are balanced in the q/m relation, where q is the POM charge and m the number of metal centers.[5]

Indeed, the q/m relation allows explaining the electrochemical behavior of polyoxometalates, but in a qualitative manner. For example, the group of Prof. Pope indicated that for α-Keggin polyoxotungstates the reduction potential decreases 0.16 V per unit charge, but the q/m relation cannot give a numerical explanation for this variation.[6] Regardless, the theoretical models can explain the electrochemical properties of POMs in solution.

Table 5.1 Reduction potentials (in V) for three different α-Keggin polyoxotungstates.

	E_{red}
$[\alpha\text{-}AlW_{12}O_{40}]^{5-}$	-0.36
$[\alpha\text{-}SiW_{12}O_{40}]^{4-}$	-0.19
$[\alpha\text{-}PW_{12}O_{40}]^{3-}$	-0.02

These properties can be easily tuned by substitution of one or more metallic centers or by functionalization of the POM.[7] Therefore, their adsorption on a surface should also alter their electronic structure. We already know that silicotungstate acid is spontaneously reduced after adsorption on silver,[8] but no further data has yet been reported. It would be really interesting to know if the charge of the POM has an impact on phenomenon, as well as the metal.

Understanding their behavior on a surface could be an important key in developing new functional devices specifically designed for a concrete purpose.

5.2. Motivation and Objectives

The aim of this chapter is to carry out a systematic study in order to evaluate whether the metal – and charge – dependent behavior that the α-Keggin anion exhibits is also reproduced when it is adsorbed. The systems we studied were the $[\alpha\text{-}AlW_{12}O_{40}]^{5-}$, $[\alpha\text{-}SiW_{12}O_{40}]^{4-}$, $[\alpha\text{-}PW_{12}O_{40}]^{3-}$, and their homologous molybdates $[\alpha\text{-}SiMo_{12}O_{40}]^{4-}$ and $[\alpha\text{-}PMo_{12}O_{40}]^{3-}$. From this point onward, we will refer to these POMs as AlW, SiW, PW, SiMo, and PMo respectively.

This set of polyoxometalates will permit us to evaluate two different effects, both those of the charge and the metal. The main issue is that there is no information reported about their adsorption on the silver surface. Due to the different charge they have, they are likely to adsorb in different superstructures and coverages. However, in order to reduce the difference between all the systems, we assumed that all of them are adsorbed like SiW on Ag(100) at the highest coverage possible. For a better comparison, we also used the same counterion in all cases, K^+.

Thus, the objectives for this chapter are:

- To determine the lowest energy adsorption site for each POM on Ag(100).
- To evaluate post-adsorption polyoxometalate distortion.
- To observe how charge affects counterion behavior.
- To analyze the electronic structure of the systems.
- To evaluate the surface to POM charge transfer.
- To check if the behavior of the POMs in solution is the same as when they are adsorbed on silver surface.
- To determine if the strategy we designed can be applied to different POMs.

5.3. Computational Details

In this work we used both quantum mechanics and molecular dynamics simulations. All quantum mechanic calculations were done using the Perdew-Wang 91 exchange correlation functional[9] and the electron-ion interaction was described by means of the Projector Augmented Wave (PAW).[10] All geometries were optimized to self-consistency, setting the convergence parameters for the electronic and ionic optimization to $1 \cdot 10^{-5}$ eV and $2 \cdot 10^{-2}$ eV·Å^{-1}, allowing both the POM and the silver layer closest to the POM to relax. The reciprocal space was described using 5 k-points, obtained by the 3x3x1 Monkhorst Pack Scheme.[11] Finally, Bader AIM charges were obtained using the Henkelman algorithm.[12]

For molecular dynamic simulations we set up the initial configurations using the Packmol package.[13] For each POM-surface system we performed, at least, three independent simulations, with both POM and surface to be frozen and the solvent was described using the rigid TIP3P water model.[14] Concretely, for reproducing an approximate water density of 1 g·cm^{-3} we included 461 water molecules and the adequate number of counterions in order to keep the system neutral. Electrostatic interactions were computed using the Ewald summation in the reciprocal space, which was described using a 6 x 6 x 12 scheme and a convergence factor α of 0.309 Å^{-1}. Cut off for electrostatic and Lennard-Jones potentials was set to 0.24 Å. Lennard-Jones parameters were obtained from the literature,[15] and the cross terms were calculated using the Lorentz–Berthelod mixing rules.[16] All simulations were carried out under the Canonical Ensemble (NVT), using the Nosé-Hoover thermostat with a reequilibration time of 0.01 ps.[17] Equilibration and simulations were performed using a timestep of 1 fs, lasting 300 ps and 20 ns respectively. Radial Distribution Functions and 3D probability maps were obtained using VMD.[18]

5.4. Adsorption site and geometric discussion

For all systems, both polyoxotungstates and polyoxomolybdates, we only considered a limited number of active sites: the hollow site with starting orientations at 0 and 45 degrees (H_0 and H_{45}); the bridge site at 0 and 90 degrees (B_0 and B_{90}) and the on-top at 45 degrees (T_{45}). The election of these sites is not trivial: for SiW, H_{45}, T_{45}, B_0, and B_{90} correspond to those lowest in energy whereas

H_0 is the highest. In order to better analyze the effects of charge and metal on adsorption, we analyzed polyoxotungstates and polyoxomolybdates separately.

5.4.1. Energetic discussion

At this coverage, one of the most reliable effects of adsorption is the reorientation of the POM due to their mutual repulsion. Although the formal charge of the polyoxotungstates under study are different (from -5 to -3), POM's reorientation resulted independent of charge and metal type. Therefore, in Table 5.2, only a unique final orientation angle has been provided for each site.

The lowest energy site for SiW and PW was H_{37}, whereas for AlW it was found to be T_{20}, although H_{37} for AlW was only 2.2 kcal·mol^{-1} higher in energy than T_{20}. For all XW, and also for XMo, H_0 was the highest energetic site. Notice that for AlW, with the highest formal charge, H_0 is at 9.4 kcal·mol^{-1} above the lowest. This relative energy increases with the formal charge, being resulting in a 10.3 kcal·mol^{-1} difference for SiW and 18.8 kcal·mol^{-1} for PW. Although the range of energies defined by this site apparently depends on POM's formal charge, they are not found to be proportional. The rest of the sites are arranged differently depending on the POM's formal charge. Only H_0 active keeps being the most higher energy site for all cases.

Table 5.2 Relative energies (in kcal·mol^{-1}) for $[XM_{12}O_{40}]^{n-}$ (X= Al, Si, P; M= W, Mo; n=5, 4, 3) adsorbed on Ag(100) – H_{37}.

Adsorption Site	AlW	SiW	PW	SiMo	PMo
H_{37}	2.2	0.0	0.0	0.0	0.0
T_{20}	0.0	1.9	9.3	0.4	2.9
B_{90}	4.6	2.7	6.0	1.4	0.4
B_0	2.5	3.1	8.8	2.5	3.0
H_0	9.4	10.3	18.8	12.0	13.5

Molybdates and tungstates show similar behavior as shown in Table 5.2. Molybdates also presented different sites similarly arranged to polyoxotungstates in a narrow range of energies. For polyoxometalates, all sites with the exception of H_0 can be found in different domains at the same time. Actually, the presence of

several minima in a small range of energies originates from the fact that, on one hand, the adsorption involves four to eight Ag···O contacts in all cases and, on the other hand, the adsorption does not significantly alter the structure of POMs.

Unfortunately, relative energies do not allow us to compare the interaction between different POMs with the surface. In this context we should consider the adsorption energies but, as was shown in Chapter 2, the energy of the neutral POM is not a good reference, so we should proceed otherwise. The Ionic Binding Energy (IBE), which refers the interaction energy of the ionic fragments, is a good alternative to the adsorption energy. We should bear in mind that IBE only allows us to compare isoelectronic systems. Therefore we are only able to analyze the effect of the metal in the adsorption, but not the effect of the charge.

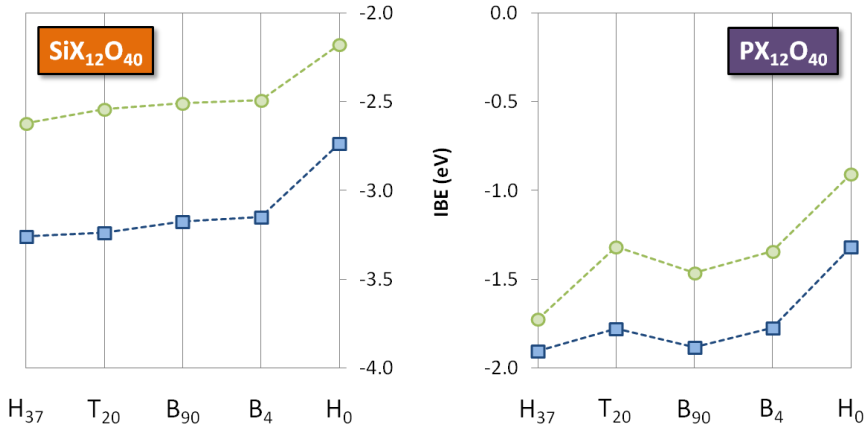

Figure 5.2 Ionic Binding Energy in eV for $[XM_{12}O_{40}]^{n-}$ (X= Si and P) for different active sites on Ag(100). IBE for M= W is represented in green whereas M = Mo is represented in blue.

In Figure 5.2, IBE for two tungstates and two molybdates are compared. In all conformations IBE is always more negative for the molybdate, clearly suggesting that they are more strongly absorbed on silver than polyoxotungstates. This stabilization is somehow larger for silicon than phosphorus, which could be derived from the different POM charge.

We already mentioned that polyoxometalates could be formulated as clathrate structures, in which a neutral cage encapsulates a formal anion. In order to

circumvent the effect of the charge in the IBE values, we have also computed the E_{ads} for the neutral cages, $W_{12}O_{36}$ and $Mo_{12}O_{36}$, without the internal ion at the H_{37} site. It is worth mentioning that E_{ads} for the molybdate cage was computed to be -1.97 eV, about 1.70 eV more negative than for the homologous tungstate, -0.28 eV. E_{ads} for neutral cages also suggest that molybdates present stronger interactions with silver than tungstates. This extra stabilization is due to: i) polyoxomolybdates havinga lower LUMO and therefore easier charge transfer from the surface for XMo than for XW POMs – a fact that would increase the ionic contribution to the bonding; and (ii) Mo-O bonds are more covalent than W-O bonds and therefore, in principle, one should expect better surface attachment for the less ionic species.

5.4.2. Geometric analysis

α-Keggin anions present an idealized T_d symmetry, derived from the regularity in the packing of MO_6 units. However, this arrangement can be altered by several factors, like the one observed on molybdates. They present an alternating "short-and-long" bond length (ABL) distortion[19] as a consequence of their smaller HOMO-LUMO gap. It leads to greater metal-oxygen π-orbital mixing under the influence of the nuclear distortion. This "Jahn-Teller" effect is influenced by the size and the charge of the system.

In Appendix 5.1 and Appendix 5.2 the averaged bond lengths for both polyoxotungstates and polyoxomolybdates (all for the H_{37} active site) are listed for comparison. Contrary to what was expected, no significant differences were observed in the POM structure, regardless of the charge or even the metal.

Where the charge effects are evident is in the POM-surface contacts, listed in Table 5.3. For Ag-O_d bonds, the largest distance is reported for the $W_{12}O_{36}$ and, as the formal charge increases, POM becomes more attached to the surface; the W_d-O_d bond was affected in an opposite fashion, as expected. This tendency is also represented in Figure 5.3, where it is confirmed that this relation is nearly linear.

Yet this linear tendency is logical, the Ag-O_d distance, of 2.16 Å is indeed shorter than expected. We already pointed out in previous chapters that atomic oxygen is placed at 2.15 Å from the silver surface,[20] which we consider as the shortest Ag-O distance possible. Therefore, one would expect asymptotic behavior around

2.15 Å, instead of the linear trend observed in Figure 5.1. It suggests that the Ag-O_d distance for AlW as well as the same distances for both SiW and PW, are somewhat underestimated.

Table 5.3 Most representative average distances (in Å) for $[AlW_{12}O_{40}]^{5-}$, $[SiW_{12}O_{40}]^{4-}$ and $[PW_{12}O_{40}]^{3-}$ on Ag(100) – H_{37} adsorption site.

Bond type	$[AlW_{12}O_{40}]^{5-}$	$[SiW_{12}O_{40}]^{4-}$	$[PW_{12}O_{40}]^{3-}$	$W_{12}O_{36}$
Ag-O_d	2.16 – 2.25	2.20 – 2.29	2.28 – 2.33	2.48
W_d-O_d	1.82	1.80	1.78	1.74
Ag-X	5.50	5.53	5.68	-
	-	$[SiMo_{12}O_{40}]^{4-}$	$[PMo_{12}O_{40}]^{3-}$	$Mo_{12}O_{36}$
Ag-O_d	-	2.21 – 2.25	2.26 – 2.33	2.39
Mo_d-O_d	-	1.82	1.77	1.74
Ag-X	-	5.52	5.61	-

Differences between tungstates and molybdates are also rather scarce. Ag-O_d distances for SiMo and PMo are identical to those in their homologous tungstates, suggesting that the POM-surface interactions are identical in both cases. However, when we examine isolated cages adsorbed on the silver surface, different results are obtained. Ag-O_d distances for $Mo_{12}O_{36}$ are 0.1 Å shorter to those obtained for $W_{12}O_{36}$ (2.39 vs 2.48 Å), behavior that is not observed when the $[XO_4]^{n-}$ anion is encapsulated.

In light of these results, the effects of charge seem to be more important than those of the metal. However, the short distances found for AlW and the observation that, in the absence of charge consideration, molybdates are more strongly adhered to the surface than tungstates, leads us to conclude that this effect is overestimated. It is worth noting here that when site exploration was carried out, counterions were not considered. That is, POMs did not have filled oxo bands, and therefore their strengths were overestimated. In order to fill these empty orbitals, the POMs attached to the closest electron source – the silver surface – and the larger the demand for electrons, the shorter the distance to the surface is.

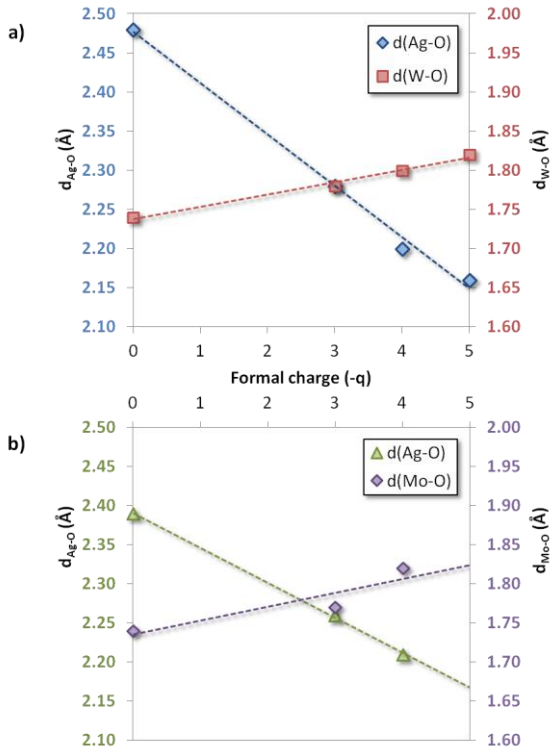

Figure 5.3 Representation of the dependence between Ag-O_d and W_d-O_d distance against the polyoxometalate formal charge for a) polyoxotungstates and b) polyoxomolybdates.

When we studied the adsorption of $[SiW_{12}O_{40}]^{4-}$, the active site, distances, and infrared spectrum were in agreement with experimental results but only without the inclusion of counterions. Apparently, the experimental Ag-O_d distances were all underestimated, fact that would explain why we did not detect it before in our calculations. In order to correct this deviation it is necessary to carry out an optimization on the system after filling the POM oxo band. Keeping in mind that optimization should be performed considering the whole environment; we decided to carry out a single optimization including explicit water molecules and counterions after we would have performed the geometry extraction and single point calculations from the molecular dynamic simulations.

5.5. Electronic structure of dodecatungstate acids on silver surfaces.

The next step in our strategy is to include both solvent and counterions around the adsorbed POM using classic molecular dynamic simulations. In all cases the system is kept neutral by including the necessary number of counterions (K^+) to compensate POM's charge. For all systems the number of water molecules has been kept at 461 molecules. It is worth noting that since we used the 2x2 unit cell, the overall number of POMs is 4.

For PW, the overall number of counterions is 12. *Adsorption, intermediate,* and *bulk regions* are rather similar to those obtained for SiW, as shown in the averaged g(*z*) graphics of Figure 5.4. Counterion trajectories for all simulations considering PW are plotted in Appendix 5.3. For SiW counterion trajectories, see Chapter 4. Although the most intense peak is found in the adsorption region (between 6 and 12.5 Å), the relative intensity of the other peaks in the *intermediate region* is somewhat different. This difference is mainly related to the counterion mobility, which is slightly higher in the case of PW since counterion concentration is lower (12 K^+ vs 16 K^+). As a consequence, the intermediate region for PW is more diffuse compared with SiW. Because of this, we set the cut-off for PW at 22 Å instead of 20 Å, the distance taken for SiW. Using this cut-off, the number of water molecules varies from 27 to 32.

For AlW the T_{20} active site was considered, as it was the lowest in energy. This POM, however, should be treated separately from SiW and PW. The number of counterions is higher than for the other two POMs: 20 K^+ instead of 16 for SiW, or 12 for PW. The shape of the averaged g(*z*) function is clearly different with respect to the other two polyoxotungstates: the most intense peak appears in the intermediate region instead of the adsorption region. This is a consequence of the high number of counterions present in the simulation. In fact, analyzing the trajectories (plotted in Appendix 5.4) we observed that almost all counterions are trapped in the upper part of the adsorbed POMs and they are barely able to reach the adsorption region. In some production runs, no counterions present in this region. In addition, counterions seem to be structured in different layers (between two and three) close to the upper part of the POM, between 14 and 15 Å from the cell origin. This observation is not consistent with the archetypical electrical double layer that appears close to the electrode surface.

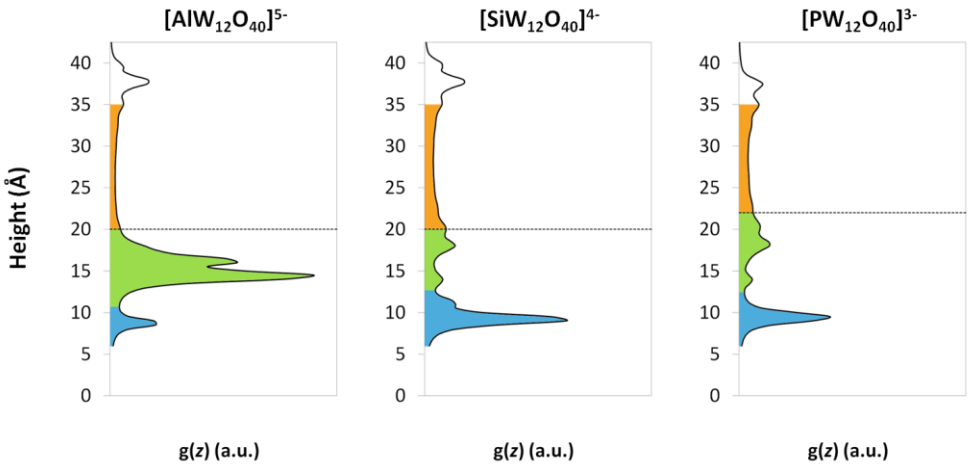

Figure 5.4 g(z) averaged graphics for all polyoxotungstates. In blue, the adsorption region; in green, the intermediate region and in orange, the bulk region.

All this evidences drive us to believe that for this charge, the distance between POMs should be larger, and consequently the coverage should be lower. In fact, it is worth noting that this unit cell is proposed for SiW, which has a charge of -4 and H^+ instead of K^+ as counterions.[8b, 21] Recently, A. Chamount and G. Wipff proved that the higher the charge is, higher condensation between POMs exists, when considering H_3O^+ as a counterion.[22] In contrast, when the counterion is larger (such as Na^+ and Cs^+), the number of POM oligomers is dramatically reduced, regardless of the POM charge. In fact, for Cs^+, Chamount and Wipff reported that AlW would be between 11.40 and 11.90 Å, and for Na^+ between 10.75 and 11.10 Å. The unit cell we are working with set the POM-POM distance at 10.60 Å.

Therefore, although the unit cell should be larger, and consequently counterions differently distributed, we persevere using our strategy since its main propose is to include solvent and counterions around the POM. We should, however, keep in mind that the picture that MD simulations are offering for AlW us is slightly different from what would be expected. Regardless of this, we set the cut-off at 20 Å as we did for SiW.

In order to classify different counterion distributions (*i.e.*, where the counterions are placed in the cell), we defined different sub-regions based on the peaks found

below 22 Å. These sub-regions correspond to the different peaks found both in the adsorption and intermediate regions. Their specific limits are summarized in Appendix 5.7. The different counterion distributions are labeled as (n_1, n_2, n_3, n_4) where n corresponds to the number of counterions in each sub-region. Although there are different possible distributions, we only considered the most probable distribution, which, in the case of PW, is (2,0,1,0), 3 K^+ in total, (2,1,1) for SiW with 4 K^+, and for AlW is (1,2,2), 5 K^+ in total. Finally, for this distribution we considered 5 different snapshots, chosen randomly.

From these different geometries, we took the one closest to the average result and optimized it until self-consistency. In the optimization, we checked the energies, not forces, as the ionic convergence parameter, setting it at $1 \cdot 10^{-5}$ eV. In addition, we reduced the number of K-points to only the Γ point. Finally and, although PW91 works rather well for describing hydrogen bonds,[23] we include Grimme dispersion into the calculations for a correct description of water disposition.[24]

We paid special attention to the Ag-O_d and X-Ag distances after optimization. Indeed, when the environment is considered, all POMs drew away from the surface, by about 0.4 Å for the Ag-O_d bond and approximately 0.6 Å for the X-Ag distance, as presented in Table 5.4. Actually, we observed the same tendency for the model with only counterions, although we considered those distances too large compared with the experimental ones (See also Chapter 3).[8b]

After optimization we also observe that the POM twists slightly with respect to its S_4 improper axis, leading to a wider interval of Ag-O_d distances. These greater distances also indicate that bonding between the POM and surface is not as strong as it was found to be when environment was not considered. However, W_d-O_d distances are almost identical for all polyoxotungstates, 1.75 – 1.76 Å, which suggest that all POMs are similarly affected by the adsorption.

Table 5.4 $Ag\text{-}O_d$, $W_d\text{-}O_d$ and X-Ag bond distances (in Å) for $AlW_{12}O_{40}^{5-}$, $SiW_{12}O_{40}^{4-}$, $PW_{12}O_{40}^{3-}$, and $W_{12}O_{36}$ after optimization considering both water and counterions.

Bond type	$[AlW_{12}O_{40}]^{5-}$	$[SiW_{12}O_{40}]^{4-}$	$[PW_{12}O_{40}]^{3-}$
$Ag\text{-}O_d$	2.37 – 2.64 (2.16 – 2.25)	2.60 – 2.67 (2.20 – 2.29)	2.68 – 2.90 (2.28 – 2.33)
$W_d\text{-}O_d$	1.75 (1.82)	1.76 (1.80)	1.76 (1.78)
Ag-X	6.02 (5.50)	6.10 (5.53)	6.32 (5.68)

Optimization slightly alters the electronic structure of the adsorbed POMs, as shown in Figure 5.5. Firstly, after optimization we observe some discontinuities between -2 and -0.5 eV that did not appear before. Regardless, since they are not found on E_F they do not affect the conductivity of the system. The W(d) band is found below E_F before and after optimization, clearly indicating that all POMs are spontaneously reduced after adsorption. Optimization hardly alters the shape of this band close to E_F, and it is for AlW that this alteration is most evident. Where optimization clearly has a remarkable impact is on the O(p) bands.

The oxo band is getting closer to E_F as the charge of the system increases; the front of that band was approximately -2.4 eV for PW; -2.2 eV for SiW, and -1.8 eV for AlW, while the W(d) band remained at the same energy, showing energetic differences of only 0.1 eV between polyoxometalates. This decrease of the "gap" is not unprecedented, as with increasing charge we expect occupied states to be higher in energy. In addition, the charge has a destabilizing effect, reflected on the oxo band. Optimization lets the system achieve a more stable situation in which repulsion between POMs is minimized. As a result, the front of the O(p) band is placed at approximately -2.5 eV for all cases (see Figure 5.5).

Where differences are more noticeable is on Bader AIM charges. The averaged charges are listed in Table 5.7, and Appendix 5.8 summarized the charges obtained for the structures of each polyoxotungstates. Before optimization neither the charge transferred from the first silver layer, Ag(1), nor the overall charge of the POM (POM + H_2O), showed any expected tendency. For PW one electron was transferred, whereas for SiW and AlW this number was found to be 2 and 2.5 respectively. This finding is in contradiction with the well-established dependence between POM charge and redox potential. Pope demonstrated in the sixties that

the reduction potentials of dodecatungstate acids show a linear dependence on POM charge of -0.16 V·(unit charge)$^{-1}$.[6] In other words, as the charge of the POM increases, the cost of reducing the POM also does, at least in solution.

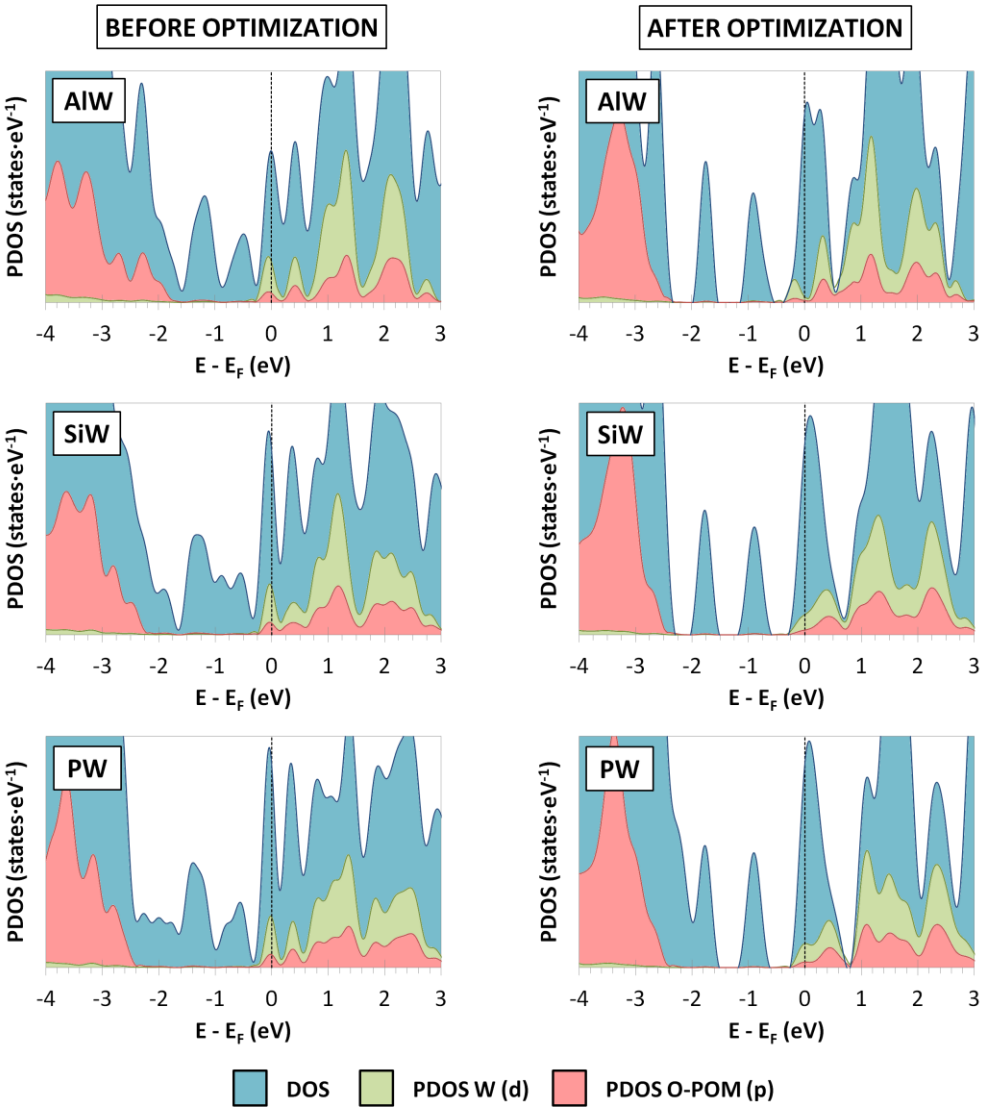

Figure 5.5 Density of States (blue) and Projected Density of States for W(d) band (green) and O(p) band (red) for a) $[AlW_{12}O_{40}]^{5-}$, b) $[SiW_{12}O_{40}]^{4-}$ and c) $[PW_{12}O_{40}]^{3-}$ including both solvent and counterions.

After optimization, the overall charge for POM and water molecules is –6.1 for AlW, -5.0 for SiW and, -4.0 for PW. In other words, for all systems only one electron has been transferred. In addition, the charge transferred from the surface to the polyoxometalate is approximately 1 electron in all cases, which is in agreement with the electronic structure.

It seems clear that optimization of the solvated POM becomes necessary for this comparative study. Although in the electronic structure of all systems, it has a minor impact in the region closest to E_F, it becomes absolutely necessary for obtaining correct results for Bader AIM Charges.

Table 5.5 Average Bader AIM atomic charges for $[AlW_{12}O_{40}]^{5-}$, $[SiW_{12}O_{40}]^{4-}$ and $[PW_{12}O_{40}]^{3-}$ on Ag(100). In parenthesis, average charges obtained before optimization and, in bold, charges after optimization.

	ΣH_2O	$XW_{12}O_{40}$	$W_{12}O_{36}$	XO_4	ΣK	$Ag(1)^a$	$Ag(2)^a$	$Ag(3)^a$	$Ag(4)^a$
AlW	**-1.0** (-1.4)	**-5.1** (-5.6)	**-2.0** (-2.6)	**-3.1** (-3.0)	**4.4** (4.3)	**1.4** (2.5)	**0.2** (0.2)	**0.3** (0.3)	**-0.3** (-0.2)
SiW	**-1.3** (-0.9)	**-3.7** (-4.4)	**-0.9** (-1.6)	**-2.9** (-2.8)	**3.6** (3.2)	**1.2** (1.9)	**0.2** (0.2)	**0.4** (0.3)	**-0.3** (-0.3)
PW	**-1.2** (-1.1)	**-2.8** (-3.2)	**-0.5** (-0.9)	**-2.3** (-2.3)	**2.7** (2.6)	**1.1** (1.5)	**0.3** (0.2)	**0.3** (0.3)	**-0.3** (-0.3)

5.6. Electronic structure of polyoxomolybdates

We followed an identical procedure for polyoxotungstates. We carried out MD simulations for polyoxomolybdates including solvent and counterions. As shown both in Appendix 5.5 and Appendix 5.6, neither the trajectories nor the g(*z*) graphics show significant differences with respect to their homologous tungstates. These results are not unexpected as electrostatic interactions govern the simulation, and for molybdates charges are almost identical to tungstates. Where these similitudes are evident is in g(*z*) graphics that maintain for SiMo and PMo the shape and number of peaks with respect to SiW and PW. Because of that, the cutoff for PMo is set at 22 Å for PMo, and 20 Å for SiMo, the same as we set for their homologous tungstates. From trajectories, we extract different snapshots

and compute the electronic structure and Bader AIM charges. We finally optimized one of these snapshots until self-consistency.

Table 5.6 Ag-O_d and X-Ag distances (in Å) for $[SiMo_{12}O_{40}]^{4-}$ and $[PMo_{12}O_{40}]^{3-}$ before and after optimization considering both water and counterions.

Bond type	$[SiMo_{12}O_{40}]^{4-}$	$[PMo_{12}O_{40}]^{3-}$
Ag-O_d	2.33 – 2.51 (2.21 – 2.30)	2.40 – 2.53 (2.26 – 2.33)
W_d-O_d	1.77 (1.82)	1.77 (1.77)
Ag-X	5.85 (5.52)	5.87 (5.61)

Both Ag-O_d and Ag-X distances increased for molybdates, but the magnitude of this increasing is slightly lower than for tungstates, about 0.2 Å for Ag-O_d, and 0.4 Å for Ag-X. Compared with tungstates, molybdates are 0.3 Å closer to the surface, which is in agreement to what we observed for the $M_{12}O_{36}$ cage, although this difference was only 0.1 Å (Ag-O_d distance was 2.48 Å for $W_{12}O_{36}$ and 2.39 Å for $Mo_{12}O_{36}$). Ag-X distance increased by 0.3 Å, which is less than what was obtained for tungstates, in which the increment was about 0.6 Å. Mo_d-O_d bond length also reflects that the bond between POM and surfaces weakens this bond in the same way regardless of the POM's charge.

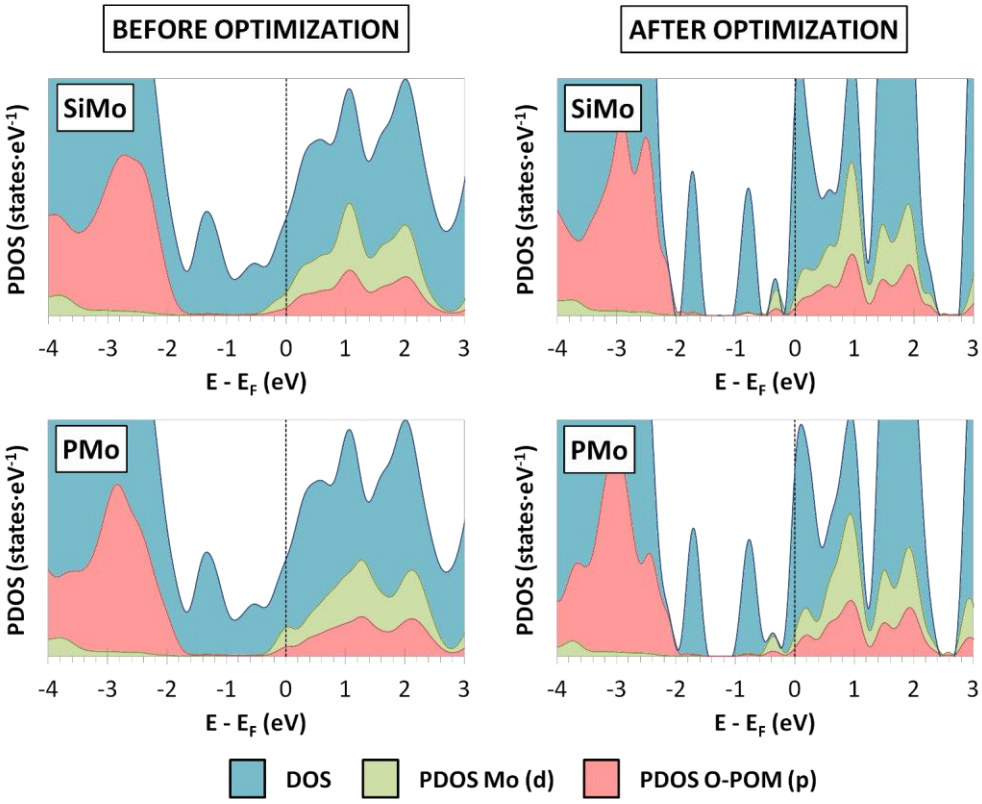

Figure 5.6 Density of States and Projected Density of States for $[SiMo_{12}O_{40}]^{4-}$ and $[PMo_{12}O_{40}]^{3-}$ before and after optimization.

For polyoxomolybdates, optimization has a clear impact on the shape of DOS and PDOS: they become steeper after rearranging the structure of the systems, as can be observed in Figure 5.6. In fact, they become quite similar to the shape observed for polyoxotungstates. Regardless of optimization, W(d) band is also found below E_F, indicating the spontaneous reduction of both polyoxomolybdates. Contrary to what was found for tungstates, O(p) suffers no significant changes after optimization.

Bader AIM charges for molybdates, collected in Table 5.7, show different results than tungstates. The charge located both on POM and bulk water is almost the same for both cases, -4.7 for PMo and -4.5 for SiMo. The difference is in the charge transferred. While for SiMo this charge transfer is of only 0.5 electrons, for PMo it is about 1.7 electrons. In addition, and in contrast to what we saw in tungstates, the first silver layer has the same charge in both cases. Optimization barely

modifies the charges of the system. However, slightly changes in the values seem to indicate that both POMs could be doubly reduced.

Table 5.7 Bader AIM atomic charges for $SiMo_{12}O_{40}$ and $PMo_{12}O_{40}$ on Ag(100) considering no environment and environment.

	ΣH_2O	$XMo_{12}O_{40}$	$Mo_{12}O_{36}$	XO_4	ΣK	$Ag(1)^a$	$Ag(2)^a$	$Ag(3)^a$	$Ag(4)^a$
SiMo	-1.3 (-1.1)	-4.4 (-4.4)	-1.8 (-1.8)	-2.7 (-2.7)	3.5 (3.5)	2.2 (1.7)	0.3 (0.3)	0.3 (0.2)	-0.3 (-0.2)
PMo	-1.3 (-0.7)	-3.6 (-4.0)	-1.4 (-1.8)	-2.2 (-2.2)	-2.7 (2.6)	1.9 (1.7)	0.2 (0.2)	0.4 (0.3)	-0.3 (-0.2)

5.7. Conclusions

We have applied the strategy we presented in the previous chapter to compare the effect of the heteroatom and the metal on the adsorption of α-Keggin anions on silver surfaces. This methodology has revealed some drawbacks, especially for describing bond distances between POMs and the surface. Although we have previously shown that the exclusion of counterions in our calculations allows us to describe the infrared spectra and the geometrical parameters, it does not work for describing electron transfer from the surface to the POM.

The problem is mainly focused on the distance between POM and surface, which is underestimated. We considered POMs as neutral species, but their oxidant strength was overestimated and, as a result, they are found much closer to the surface than expected.

In order to correct this problem, we optimized the final structure, considering both water and counterions in the optimization. With this, we corrected the distances between POM and surface and, in addition, we improved the electronic structure of the systems. It allowed us to conclude that:

- ✓ Ionic Binding Energies and adsorption energies for the external $M_{12}O_{36}$ cage clearly show that the adsorption is preferential for

polyoxomolybdates rather than polyoxotungstates. Despite this, adsorption involves a stabilization of the polyoxometalate in both cases.

✓ The attachment of POMs to the surface is related to both the charge and the metal atom. Hence, molybdates are closer to the surface than tungstates. Also, the higher the charge is, the closer to the surface the POM is.

✘ The coverage for $[AlW_{12}O_{40}]^{5-}$ is higher than the expected for this anion and likely a bigger unit cell is required for improved analysis of adsorption for this anion.

✓ All polyoxometalates are spontaneously reduced when adsorbed on the surface. Thus, polyoxotungstates are reduced by one electron, whereas for polyoxomolybdates, two electrons are transferred.

Appendix Chapter 5
Metal and Charge

Appendix 5.1 Average distances (in Å) for $[AlW_{12}O_{40}]^{5-}$, $[SiWo_{12}O_{40}]^{4-}$ and $[PW_{12}O_{40}]^{3-}$ on Ag(100) – H_{37} adsorption site.

type		AlW		SiW		PW		$W_{12}O_{36}$ [a]
Ag	O_b	2.54		2.44	(2.43)[c]	2.48		3.06
	O_c	2.28		2.20	(2.23)[c]	2.28		
	O_d	**2.16 – 2.25**		**2.20 – 2.29**	(2.06)[c]	**2.28 – 2.33**		2.48
X	O_a	1.73 – 1.79	(1.76)[b]	1.62 – 1.64	(1.64)[b]	1.54 – 1.57	(1.55)[b]	-
	Ag	**5.50**		**5.53**	(4.90)[c]	**5.68**		**-**
O_a	W_u	2.38	(2.30)[b]	2.48	(2.39)[b]	2.55	(2.48)[b]	-
	W_e	2.23 – 2.51		2.35 – 2.52		2.44 – 2.55		-
	W_d	2.15		2.27		2.38		-
O_b	W_u	1.91 – 1.98	(1.95)[b]	1.92 – 1.97	(1.94)[b]	1.92 – 1.96	(1.94)[b]	1.92
	W_e	1.87 – 2.06		1.88 – 2.02		1.89 – 2.00		1.92
	W_d	1.82 – 2.01		1.87 – 2.02		1.85 – 1.98		1.95
O_c	W_u	1.92 – 1.98	(1.94)[b]	1.93 – 1.97	(1.93)[b]	1.92 – 1.95	(1.93)[b]	-
	W_e	1.87 – 2.03		1.88 – 2.01		1.89 – 1.98		-
	W_d	1.86 – 2.07		1.87 – 2.02		1.88 – 1.99		-
O_d	W_u	1.71	(1.75)[b]	1.70	(1.74)[b]	1.70	(1.73)[b]	1.71
	W_e	1.71		1.71		1.71		1.71
	W_d	**1.82**		**1.80**		**1.78**		1.74

[a] In $W_{12}O_{36}$ there is no distinction between O_b and O_c since the angle defined by W-$O_{b/c}$-W is the same.
[b] Distances in parentheses are referred to the isolated anion computed with VASP.
[c] Si-Ag and Ag-O distances are reported for the H_{37} adsorption site in the Ag(100) high coverage situation. The Si-Ag distance is obtained by using X-Ray Specular Reflectivity, and Ag-O distances are obtained by extrapolation, considering the restrictions that Si-Ag distance imposes.

Appendix 5.2 Average distances (in Å) for $[SiMo_{12}O_{40}]^{4-}$ and $[PMo_{12}O_{40}]^{3-}$ on Ag(100) – H_{37} adsorption site.

Bond		SiMo		PMo		$Mo_{12}O_{36}$
Ag[a]	O_b	2.39		2.48		2.83
	O_c	2.19		2.30		-
	O_d	2.21 – 2.30		2.26 – 2.33		2.39
X	O_a	1.63 – 1.66	(1.65)[b]	1.54 – 1.56	(1.55)[b]	-
	Ag	5.52		5.61		-
O_a	Mo_u	2.47	(2.40)[b]	2.54	(2.47)[b]	-
	Mo_e	2.33 – 2.51		2.44 – 2.55		-
	Mo_d	2.28		2.36 – 2.41		-
O_b	Mo_u	1.92 – 1.97	(1.88 – 1.99)[b]	1.92 – 1.95	(1.93)[b]	1.88 – 1.97
	Mo_e	1.86/1.91 – 2.00/2.07		1.89/1.99 – 2.02		1.92 – 1.96
	Mo_d	1.81/1.84 – 1.95		1.99		1.92 – 1.93
O_c	Mo_u	1.91 – 1.94	(1.89 – 2.01)[b]	1.93 – 1.97	(1.94)[b]	-
	Mo_e	1.87 – 1.94/2.07		1.89 – 2.00		-
	Mo_d	1.83/1.98 – 2.07		1.88 – 2.02		-
O_d	Mo_u	1.70	(1.73)[b]	1.70	(1.72)[b]	1.70
	Mo_e	1.71		1.70		1.70
	Mo_d	**1.82**		**1.77**		**1.74**

[a] O_d is placed on bridge, explaining why there are two Ag-O_d distances instead of one.
[b] Distances for the free anion computed with VASP.

Appendix 5.3 Trajectories for all the K^+ ions along the z-axis for a 20-ns-long simulation for each production run for $[PW_{12}O_{40}]^{3-}$ on Ag(100). On the right of each trajectory, g(*z*) derived from the trajectories: blue, the adsorption region; green, the intermediate region and orange, the bulk region region.

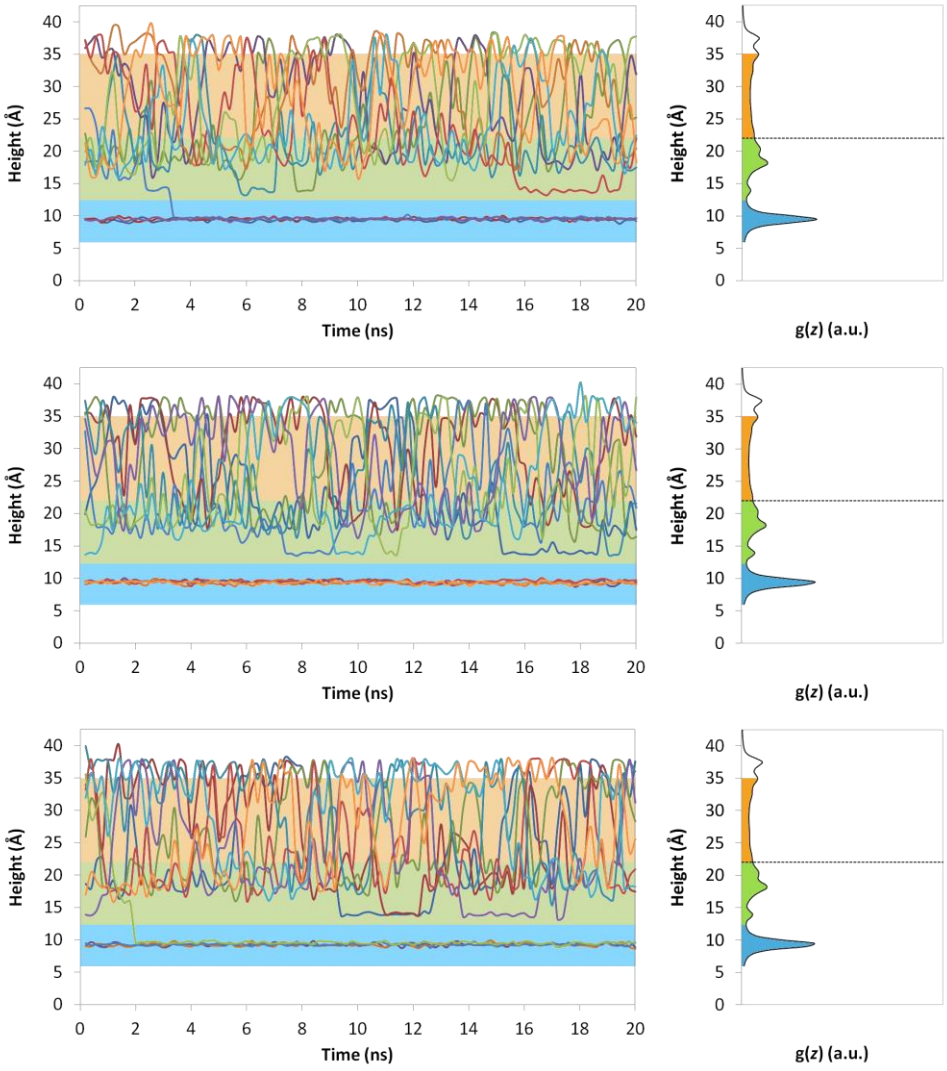

Appendix 5.4 Trajectories for all the K^+ ions along the z-axis for a 20-ns-long simulation for each production run for $[AlW_{12}O_{40}]^{5-}$ on Ag(100). On the right of each trajectory, g(*z*) derived from the trajectories: blue, the adsorption region; green, the intermediate region and orange, the bulk region region.

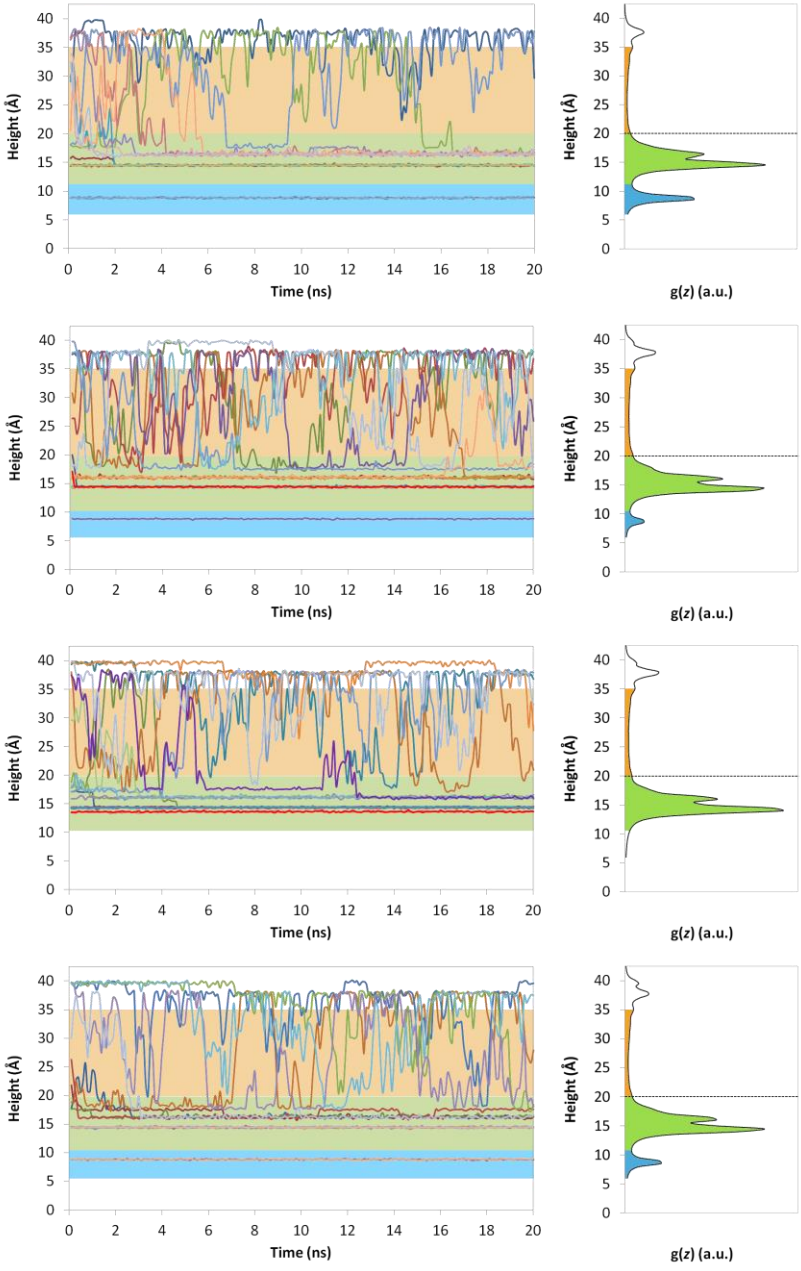

Appendix 5.5 Trajectories for all the K^+ ions along the z-axis for a 20-ns-long simulation for each production run for $[PMo_{12}O_{40}]^{3-}$ on Ag(100). On the right of each trajectory, Linear Distribution Function g(*z*) derived from the trajectories. The different colors represent the different regions: in blue, the adsorption region; in green, the intermediate region and finally, in orange, the bulk region or bulk solution region.

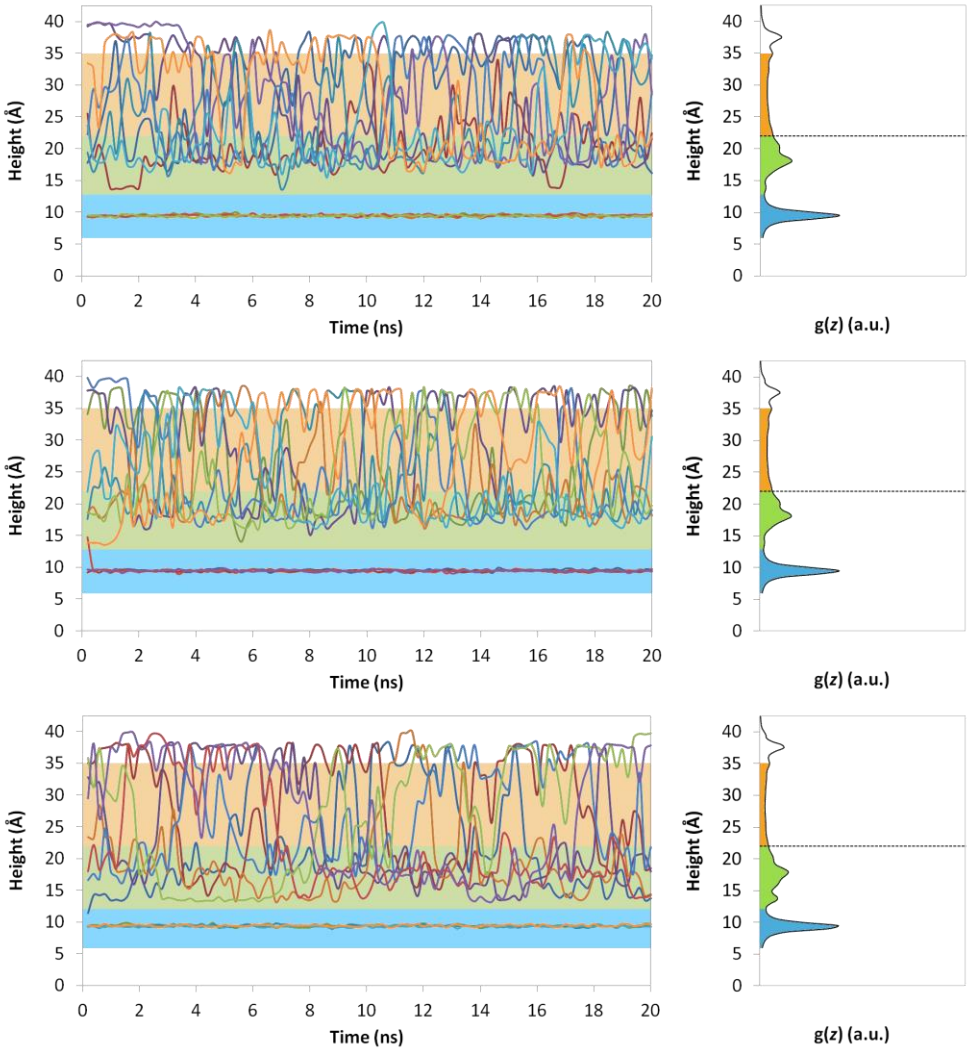

Appendix 5.6 Trajectories for all the K^+ ions along the z-axis for a 20-ns-long simulation for each production run for $[SiMo_{12}O_{40}]^{4-}$ on Ag(100). On the right of each trajectory, Linear Distribution Function g(*z*) derived from the trajectories. The different colors represent the different regions: in blue, the adsorption region; in green, the intermediate region and finally, in orange, the bulk region or bulk solution region.

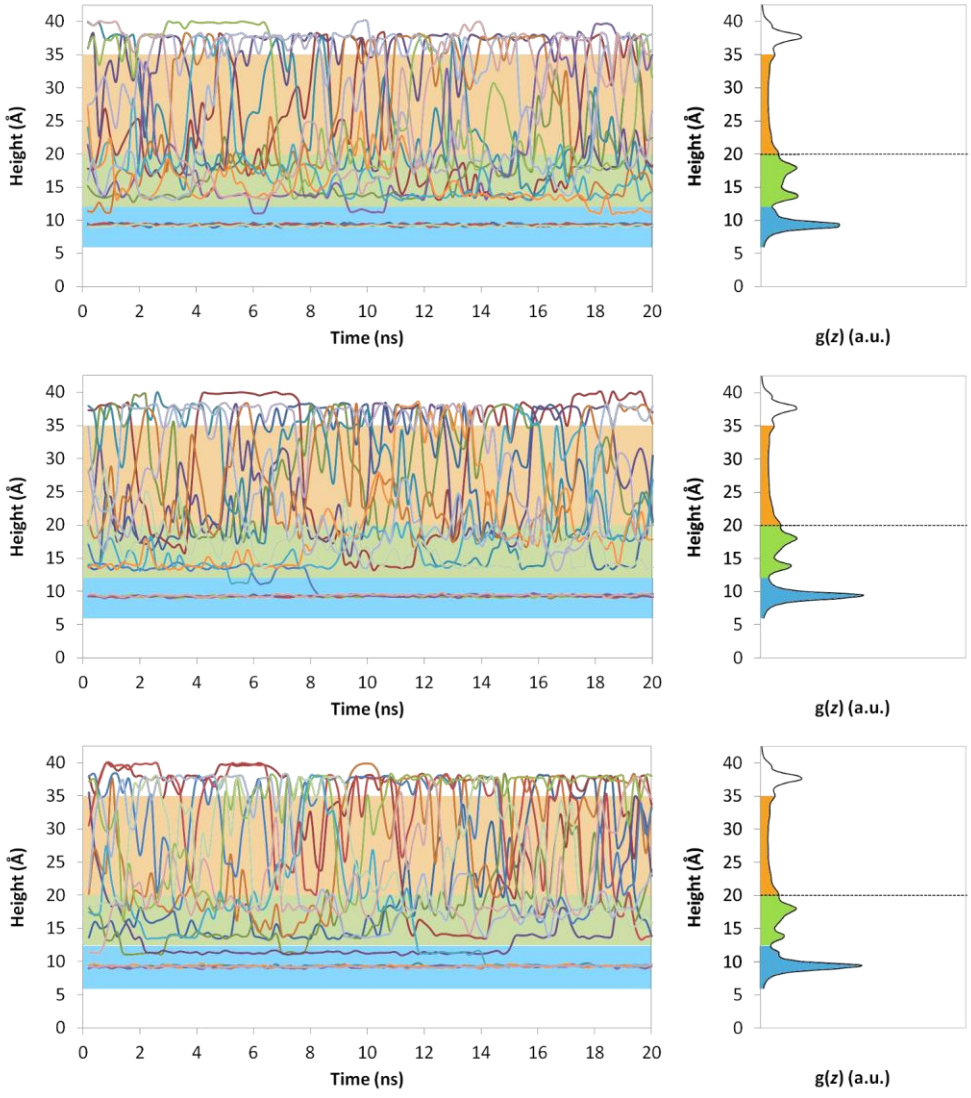

Appendix 5.7 Specific region limits for each polyoxometalate. These limits are referred to the height respect the origin of the cell, in Å.

	AlW	SiW	PW	SiMo	PMo
Int. Region	-	-	19.5 – 22.0	-	19.5 – 22.0
	15.5 - 20.0	16.5 - 20.0	15.0 – 19.5	14.0 – 20.0	15.0 – 19.5
	10.8 – 15.5	12.5 – 16.5	12.5 – 15.0	12.0 – 14.0	12.5 – 15.0
Ads. Region	6.0 – 10.8	6.0 – 12.5	6.0 – 12.5	6.0 – 12.0	6.0 – 12.5

Appendix 5.8 List of Bader AIM atomic charges for the different snapshots obtained for $[AlW_{12}O_{40}]^{5-}$, $[SiW_{12}O_{40}]^{4-}$ and $[PW_{12}O_{40}]^{3-}$ on Ag(100) with and without consideration of the environment.

Dist.	ΣH_2O	$XW_{12}O_{40}$	$W_{12}O_{36}$	XO_4	ΣK	Ag(1)[a]	Ag(2)[a]	Ag(3)[a]	Ag(4)[a]
n.e.[b]	-	-3.3	-0.3	-3.0	-	3.0	0.4	0.1	-0.2
	-1.6	-5.6	-2.6	-3.0	4.4	2.5	0.2	0.3	-0.2
	-1.6	-5.5	-2.5	-3.0	4.3	2.6	0.2	0.3	-0.2
$AlW_{12}O_{40}$ (1,2,2)[c]	-1.3	-5.7	-2.7	-3.0	4.4	2.4	0.2	0.3	-0.2
	-1.3	-5.6	-2.6	-3.0	4.2	2.4	0.1	0.3	-0.2
	-1.2	-5.8	-2.8	-3.0	4.4	2.5	0.2	0.3	-0.2
av	*-1.4*	*-5.6*	*-2.6*	*-3.0*	*4.3*	*2.5*	*0.2*	*0.3*	*-0.2*
n.e.[b]	-	-2.9	-0.1	-2.8	-	1.8	0.2	0.3	-0.3
	-0.7	-4.2	-1.4	-2.8	2.9	1.9	0.1	0.3	-0.3
	-0.7	-4.2	-1.4	-2.8	2.9	1.9	0.1	0.3	-0.3
$SiW_{12}O_{40}$ (2,1,1)[c]	-1.4	-4.1	-1.3	-2.8	3.5	1.8	0.2	0.3	-0.2
	-0.8	-4.3	-1.4	-2.8	3.0	1.9	0.1	0.3	-0.3
	-0.4	-5.0	-2.2	-2.8	3.4	1.9	0.2	0.3	-0.3
av	*-0.9*	*-4.4*	*-1.6*	*-2.8*	*3.2*	*1.9*	*0.2*	*0.3*	*-0.3*
n.e.[b]	-	-2.5	-0.2	-2.3	-	2.1	0.4	0.1	0.0
	-1.0	-3.5	-1.2	-2.3	2.6	1.7	0.2	0.3	-0.3
	-1.4	-2.9	-0.5	-2.3	2.6	1.4	0.2	0.3	-0.3
$PW_{12}O_{40}$ (2,0,1,0)[c]	-0.8	-3.5	-1.1	-2.3	2.6	1.4	0.2	0.3	-0.3
	-1.2	-3.1	-0.8	-2.3	2.6	1.5	0.2	0.3	-0.3
	-1.1	-3.3	-1.0	-2.3	2.6	1.5	0.2	0.3	-0.3
av	*-1.1*	*-3.2*	*-0.9*	*-2.3*	*2.6*	*1.5*	*0.2*	*0.3*	*-0.3*

[a] Ag(X), where X indicates the silver layer, with 1 being the closest to the adsorbate.
[b] n.e. means no embedding effects are considered, *i.e.* Ag + POM.
[c] Numbers (n_1, n_2, n_3, n_4) identify the K^+ ions belonging to adsorption region, intermediate region and solution, respectively (see text for more details). We consider here the whole environment, *i.e.* Ag + POM + 17/20 H_2O + 5 K for $AlW_{12}O_{40}$; Ag + POM + 21/23 H_2O + 4 K for $SiW_{12}O_{40}$ and Ag + POM + 27/32 H_2O + 3 K for $PW_{12}O_{40}$.

Appendix 5.9 List of Bader AIM atomic charges for the different snapshots obtained for $[SiMo_{12}O_{40}]^{4-}$ and $[PMo_{12}O_{40}]^{3-}$ on Ag(100) with and without consideration of the environment.

Dist.	ΣH_2O	$XMo_{12}O_{40}$	$Mo_{12}O_{36}$	XO_4	ΣK	Ag(1)[a]	Ag(2)[a]	Ag(3)[a]	Ag(4)[a]
n.e.[b]	-	-3.0	-0.3	-2.7	-	2.7	0.3	0.2	-0.2
	-1.2	-4.4	-1.8	-2.6	3.5	1.8	0.3	0.2	-0.2
	-1.1	-4.4	-1.7	-2.7	3.5	1.7	0.3	0.2	-0.3
$SiMo_{12}O_{40}$ (2,1,1)[c]	-1.1	-4.2	-1.6	-2.6	3.3	1.7	0.3	0.2	-0.3
	-1.0	-4.4	-1.8	-2.6	3.5	1.6	0.3	0.2	-0.2
	-0.9	-4.8	-2.1	-2.7	3.6	1.7	0.3	0.2	-0.2
av	*-1.1*	*-4.4*	*-1.8*	*-2.7*	*3.5*	*1.7*	*0.3*	*0.2*	*-0.2*
n.e.[b]	-	-2.5	-0.2	-2.3	-	2.2	0.3	0.2	-0.2
	-0.7	-3.8	-1.6	-2.2	2.6	1.7	0.2	0.3	-0.2
	-0.7	-3.9	-1.7	-2.2	2.6	1.7	0.2	0.3	-0.2
$PMo_{12}O_{40}$ (2,0,1,0)[c]	-0.1	-4.4	-2.1	-2.2	2.6	1.7	0.2	0.3	-0.3
	-1.2	-3.4	-1.2	-2.2	2.6	1.8	0.2	0.3	-0.2
	0.0	-4.6	-2.4	-2.2	2.6	1.7	0.2	0.3	-0.2
av	*-0.7*	*-4.0*	*-1.8*	*-2.2*	*2.6*	*1.7*	*0.2*	*0.3*	*-0.2*

[a] Ag(X), where X indicates the silver layer, with 1 being the closest to the adsorbate.
[b] n.e. means no embedding effects are considered, *i.e.* Ag + POM.
[c] Numbers (n_1, n_2, n_3, n_4) identify K^+ ions belonging to adsorption region, intermediate region, and solution, respectively (see text for further details). We consider here the whole environment, *i.e.* Ag + POM + 18/20 H_2O + 4 K for $SiMo_{12}O_{40}$ and Ag + POM + 26/30 H_2O + 3 K for $PW_{12}O_{40}$.

References Chapter 5
Effect of the charge and the metal

[1] M. Sadakane, E. Steckhan, *Chem. Rev.* **1998**, *98*, 219-238.
[2] (a) X. Lopez, C. Bo, J. M. Poblet, *J. Am. Chem. Soc.* **2002**, *124*, 12574-12582; (b) J. M. Maestre, X. Lopez, C. Bo, J. M. Poblet, N. Casan-Pastor, *J. Am. Chem. Soc.* **2001**, *123*, 3749-3758.
[3] J. M. Poblet, X. Lopez, C. Bo, *Chem. Soc. Rev.* **2003**, *32*, 297-308.
[4] (a) V. W. Day, W. G. Klemperer, *Science* **1985**, *228*, 533-541; (b) M. T. Pope, *Heteropoly and Isopoly Oxometalates, Vol. 8*, Springer-Verlag, Berlin, **1983**.
[5] (a) X. Lopez, J. A. Fernandez, J. M. Poblet, *Dalton Trans.* **2006**, 1162-1167; (b) X. López, J. A. Fernández, S. Romo, J. F. Paul, L. Kazansky, J. M. Poblet, *J. Comput. Chem.* **2004**, *25*, 1542-1549.
[6] M. T. Pope, G. M. Varga, *Inorg. Chem.* **1966**, *5*, 1249-1254.
[7] A. Dolbecq, E. Dumas, C. R. Mayer, P. Mialane, *Chem. Rev.* **2010**, *110*, 6009-6048.
[8] (a) X. Aparicio-Angles, P. Miro, A. Clotet, C. Bo, J. M. Poblet, *Chem. Sci.* **2012**, *3*, 2020-2027; (b) C. M. Teague, X. Li, M. E. Biggin, L. Lee, J. Kim, A. A. Gewirth, *J. Phys. Chem. B* **2004**, *108*, 1974-1985.
[9] J. P. Perdew, J. A. Chevary, S. H. Vosko, K. A. Jackson, M. R. Pederson, D. J. Singh, C. Fiolhais, *Phys. Rev. B: Condens. Matter* **1992**, *46*, 6671-6687.
[10] P. E. Blöchl, *Phys. Rev. B: Condens. Matter* **1994**, *50*, 17953-17979.
[11] H. J. Monkhorst, J. D. Pack, *Phys. Rev. B: Condens. Matter* **1976**, *13*, 5188-5192.
[12] (a) R. F. W. Bader, *Atom in Molecules: A Quantum Theory*, Oxford University Press, Oxford, **1990**; (b) G. Henkelman, A. Arnaldsson, H. Jonsson, *Comput. Mater. Sci.* **2006**, *36*, 354-360.
[13] L. Martínez, R. Andrade, E. G. Birgin, J. M. Martínez, *J. Comput. Chem.* **2009**, *30*, 2157-2164.
[14] W. L. Jorgensen, J. Chandrasekhar, J. D. Madura, R. W. Impey, M. L. Klein, *J. Chem. Phys.* **1983**, *79*, 926-935.
[15] (a) X. Lopez, C. Nieto-Draghi, C. Bo, J. B. Avalos, J. M. Poblet, *J. Phys. Chem. A* **2005**, *109*, 1216-1222; (b) F. Leroy, P. Miro, J. M. Poblet, C. Bo, J. B. Avalos, *J. Phys. Chem. B* **2008**, *112*, 8591-8599; (c) H. Heinz, R. A. Vaia, B. L. Farmer, R. R. Naik, *J. Phys. Chem. C* **2008**, *112*, 17281-17290.
[16] M. P. Allen, D. J. Tildesley, *Computer Simulation of Liquids*, Clarendon Press, Oxford, **1989**.
[17] (a) S. Nosé, *J. Chem. Phys.* **1984**, *81*, 511-519; (b) S. Nosé, *Mol. Phys.* **1984**, *52*, 255-268.
[18] W. Humphrey, A. Dalke, K. Schulten, *J. Molec. Graphics* **1996**, *14*, 33-38.
[19] (a) H. R. Allcock, E. C. Bissell, E. T. Shawl, *J. Am. Chem. Soc.* **1972**, *94*, 8603-8604; (b) H. R. Allcock, E. C. Bissell, E. T. Shawl, *Inorg. Chem.* **1973**, *12*, 2963-2968.
[20] Y. Wang, L. L. Jia, W. N. Wang, K. N. Fan, *J. Phys. Chem. B* **2002**, *106*, 3662-3667.
[21] (a) L. Lee, J. X. Wang, R. R. Adžić, I. K. Robinson, A. A. Gewirth, *J. Am. Chem. Soc.* **2001**, *123*, 8838-8843; (b) L. Lee, A. A. Gewirth, *J. Electroanal. Chem.* **2002**, *522*, 11-20.

[22] A. Chaumont, G. Wipff, *Eur. J. Inorg. Chem.* **2013**, *2013*, 1835-1853.
[23] S. Tsuzuki, H. P. Luthi, *J. Chem. Phys.* **2001**, *114*, 3949-3957.
[24] S. Grimme, *J. Comput. Chem.* **2006**, *27*, 1787-1799.

Chapter 6
Gold surfaces as Nanoparticles Model

Polyoxometalates are known to stabilize metal (0) nanoparticles in solution. This stabilization occurs via the formation of self-assembled monolayers on a nanoparticle's surface. In the structure of the monolayer, counterions are structurally included in the interface and play an important role in the stabilization of the monolayer. In this context, we want to extend and enhance our strategy for modelling the adsorption of highly charged POMs on nanoparticle surfaces.

UNIVERSITAT ROVIRA I VIRGILI
COMPUTATIONAL MODELLING OF POLYOXOMETALATES ADSORBED ON METALLIC SURFACES
Xavier Aparicio Anglès
Dipòsit Legal: T. 1525-2013

6.1. Introduction

Polyoxometalates form organized self-assembled monolayers not only on planar surfaces, but also on metal nanoparticles (NPs).[1] In the context of nanoparticles, the POM plays the role of ligand protector, stabilizing the whole nanocluster.[2] Considering, then, the wide range of POMs and NPs, we can realize an uncountable number of composite materials, some of which has been applied in different fields such as synthesis and catalysis.[3] Indeed, these nanocluster applications are derived from the unique redox properties of POMs in combination with NP catalytic power.

Interactions between the POM and NP surface results in adsorption, like in the case of a metallic surface.[4] In fact, one can associate extended surfaces as a first approximation to modeling large NPs. We have already demonstrated that the charge of POMs has a major influence in the adsorption. As we saw in the last chapter, higher charge brings about stronger interactions. To provide a good description of the system counterions must be taken into account, so counterions play an important role in the self-assembled monolayers (SAM) structure.

Combining Cryo-TEM images and UV-visible spectroscopy, Weinstock *et al*. observed that the stability of POM SAM on metal NPs depended on the nature of the counterion, as they were structurally integrated into the POM-NP interface.[5] These authors also provided information about the orientation of POMs with different shapes on the NP surface by means of Cryo-TEM images.[6]

Despite the strong potential that these techniques have for elucidating structural information regarding this interface, they present some limitations. In the case of the laccunary $AlW_{11}O_{39}^{9-}$, Cryo-TEM images only provide information about the thickness of the interface, as well as the separation between POMs, but not about the orientation of the structure. One of the peculiarities of this compound is that the vacancy can be filled by another molecular species, allowing for POM functionalization.[7] If the vacancy lays open to the solution instead of facing down on the surface, the POM could be specifically tuned depending on desired application. To address this question, we turn to computational studies.

6.2. Motivation and Objectives

We want to study the possible orientations of $AlW_{11}O_{39}^{9-}$ on gold nanoparticles for determining the POM's lacuna orientation once the POM is adsorbed on the surface. To answer this question we want to employ our initial strategy (see Chapter 4). Unfortunately, this strategy overestimates POM-surface interactions; whose deviation increases with the charge. One way to fix this problem is to optimize the system considering in the same calculation all of the surface, POM, and environment (see Chapter 5). However, it turns our strategy into a highly time consuming task, which evidences the need of circumventing this problem in the first steps of the strategy.

Hence, the aim of this chapter is devoted to optimizing the procedure for analyzing the adsorption of high charged POMs on metal surfaces. Instead of using the lacunary POM (because of its high charge), we used the $[AlW_{12}O_{40}]^{5-}$ for performing our test. The experimental data for the test model was obtained by the group of Prof. Ira Weinstock, from the Ben Gurion University of the Negev, but not published yet.

Therefore, the objectives for this chapter are to:

- ✓ Modify our initial strategy in adequately model the adsorption of highly charged POMs on metallic surfaces in a facile manner.
- ✓ Determine how $[AlW_{12}O_{40}]^{5-}$ is adsorbed on gold surfaces.
- ✓ Evaluate the effect of different counterions on the adsorption of $AlW_{12}O_{40}^{5-}$ on gold surfaces.
- ✓ Obtain the electronic structure of the whole system and see whether or not the POM is spontaneously reduced by the surface.

6.3. Computational Details

In this work we used both quantum mechanics and molecular dynamics simulation. All calculations performed using quantum mechanics were done using the Perdew-Wang 91 exchange correlation functional[8] and the electron-ion interaction was described by means of the Projector Augmented Wave (PAW).[9] All geometries were optimized to self-consistency, setting the convergence parameters for the electronic and ionic optimization to $1 \cdot 10^{-5}$ eV in both cases,

allowing both the POM and the gold layer closest to it to relax. The reciprocal space was described using only the Γ point, obtained by the 1 x 1 x 1 Monkhorst Pack Scheme.[10] Finally, Bader AIM charges were obtained using the Henkelman algorithm.[11]

Initial configurations for molecular dynamic simulations were obtained using the Packmol package.[12] In simulations we considered the POM, counterions, and surface to be frozen. Solvent was modeled by means of the rigid TIP3P water model, including 246 water molecules in the cage for a density of 1 $g \cdot cm^{-3}$.[13] Electrostatic interactions were computed using the Ewald summation in the reciprocal space, which was described using a 5 x 6 x 15 scheme and a convergence factor α of 0.393 $Å^{-1}$. Cut off for electrostatic and Lennard-Jones potentials was set to 7.37 Å. Lennard-Jones parameters were obtained from the literature,[14] and the cross terms were calculated using the Lorentz–Berthelod mixing rules.[15] All simulations were carried out under the Canonical Ensemble (NVT), using the Nosé-Hoover thermostat with a reequilibration time of 0.01 ps.[16] Equilibration and simulations were performed using a timestep of 1 fs, lasting 300 ps and 2 ns respectively. Radial Distribution Functions and 3D probability maps were obtained using VMD.[17]

6.4. Surface Model

Diameters of gold nanoparticle cores can vary depending on the preparation method used. Independently, their size is large enough (more than 6.6 nm) for considering the slab model as a first candidate for modeling gold NP surface. Analyzing the images reported by Weinstock *et al*., most of the gold NPs are nearly spherical but it is often observed some polyhedral particles with flat faces, as shown in Figure 6.1. The size and the presence of flat faces justify the use of the slab model as a first approximation for modeling the adsorption on gold nanoparticles.

$[AlW_{12}O_{40}]^{5-}$ anions are placed about 14 ± 2 nm from each other. Due to the variability of the distance and to the fact that we have no specific information regarding either the unit cell or the surface, decided to set up two different unit cells, one for the (100) and other for the (111) gold surface.

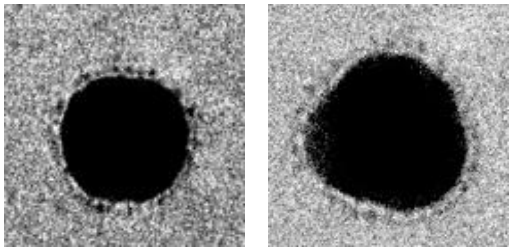

Figure 6.1 Cryo-TEM images for $AlW_{12}O_{40}^{5-}$ on gold nanoparticles with Cs^{+} as the counterion, obtained by the group of Ira Weinstock.

For Au(111) surface we used the $\begin{pmatrix} 5 & 0 \\ 6 & 3 \end{pmatrix}$ unit cell, in the matrix notation; the one we used for modeling the Ag(111) low coverage unit cell. In this cell, the length of the axis is $|\overrightarrow{a_2}| = 5 \cdot |\overrightarrow{a_1}| = 14.76$ Å, and $|\overrightarrow{b_2}| = 3\sqrt{5} \cdot |\overrightarrow{a_1}| = 15.34$ Å. The angle between $\overrightarrow{a_2}$ and $\overrightarrow{b_2}$ is 90°. The number of atoms per layer is 30, therefore the coverage for this superstructure is θ = 1/30 = 0.03, and three layers were considered in the model.

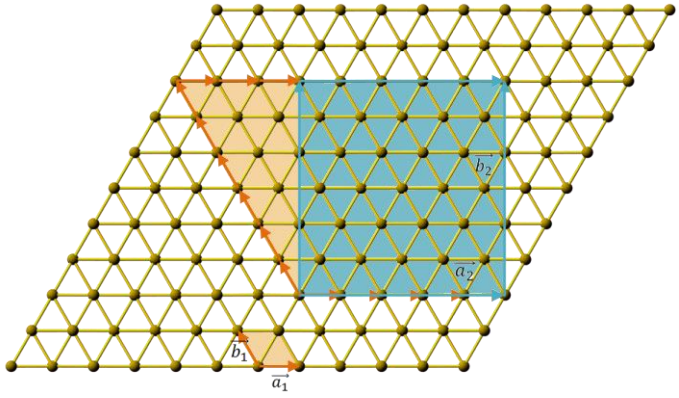

Figure 6.2 Unit cell for the adsorption of $AlW_{12}O_{40}$ on the Au(111) surface.

6.5. New strategy

Until now, the steps we followed for determining the electronic structure of our system were conditioned by the first one, which involved evaluating the relative energies of different sites considering the adsorption of the neutral POM. We

showed that despite being able to reproduce the adsorption site as well as the IR spectrum, the neutral model did not correctly describe the charge transfer.

In order to minimize the error in the initial step, we considered that the first analysis should include the exact number of counterions required to compensate for the charge of the POM. We also wanted to evaluate whether this strategy allowed us to determine the stability of the SAM depending on the identity of the counterion, so we considered Cs^+ and K^+ as counterions. The cations were randomly distributed around the POM and optimized along with the whole POM geometry and the first gold layer.

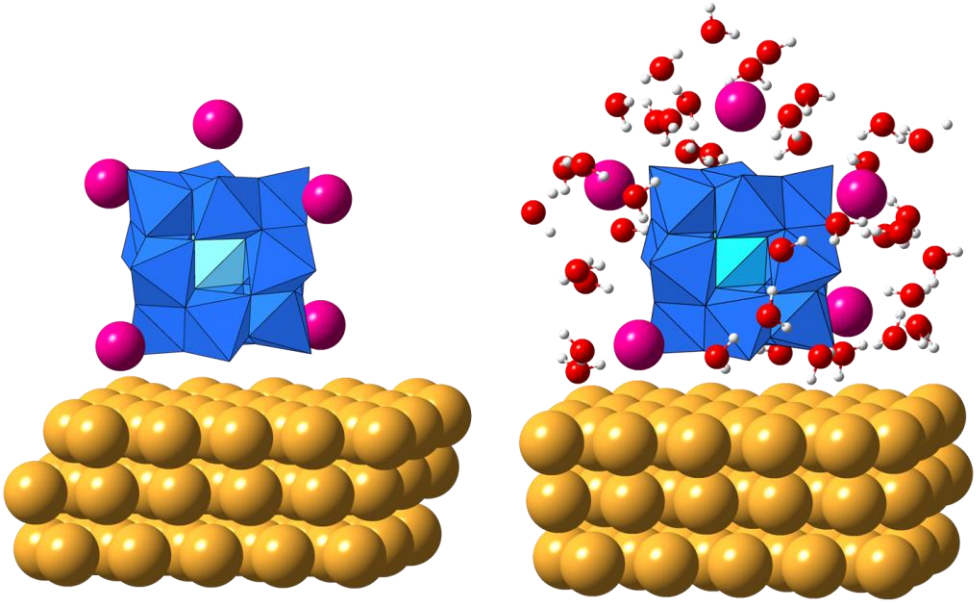

Figure 6.3 Polyhedral-and-Balls representation for $Cs_5AlW_{12}O_{40}$ on Au(111) and solvated $Cs_5AlW_{12}O_{40}$ on Au(111).

As the analysis without counterions allows for determination of the adsorption site, we wanted to compare the data obtained using both systems. After that, we included water around the POM in order to rearrange the orbital energies and to obtain a more precise picture of the electronic structure.

6.5.1. Adsorption sites for $Cs_5AlW_{12}O_{40}$, $K_5AlW_{12}O_{40}$, and $AlW_{12}O_{40}$

For Au(111) we evaluated the relative energy of active sites for the three aforementioned POM systems. Table 6.1 lists the relative energies for B_0, Fcc_0, T_0, and B_{30} active sites on the Au(111) surface. We chose these sites for the same reasons outlined in Chapter 5: B_0, Fcc_0, B_{30} were the lowest in energy for Ag(111) in low coverage situation whereas T_0 was found to be the highest.

Focusing on the Au(111) surface, for Cs^+ and K^+ as counterions, B_0 is the lowest energy POM active site, whereas without counterions we find that this site is Fcc_0. For the model including counterions, all sites were found in a very narrow range of energies, only 4 kcal·mol^{-1}, which means that all sites are equally probable. On the contrary, the energy difference between sites without counterions were more acute with an energy range of about 19 kcal·mol^{-1}. This is a consequence of the neutral model as the energies are strongly dependent on the interaction between terminal oxygens and gold atoms.

Although both approximations reported different minima for adsorption sites, B_0 for the counterion model and Fcc_0 for the neutral model, it should be observed that Fcc_0 is only 1.3 kcal·mol^{-1} higher in energy. Therefore, we can assume that the error encountered when counterions were considered is negligible.

We also computed the adsorption energies by optimizing the free POM with counterions located at the same locations. Counterion location can alter the E_{ads}, so we can only consider these energies as a reference. In all cases, E_{ads} was negative, so adsorption is favorable.

Table 6.1 Relative energies (in kcal·mol^{-1}) and adsorption energies (in eV) for $AlW_{12}O_{40}$ and $M_5AlW_{12}O_{40}$ (M = Cs and K) adsorbed on Au(111).

	E_{rel} (kcal·mol^{-1})			E_{ads} (eV)	
site	Cs	K	-	Cs	K
B_0	**0.0**	**0.0**	6.1	**-0.71**	**-0.81**
Fcc_0	1.3	0.9	**0.0**	-0.65	-0.77
T_0	2.2	2.4	13.0	-0.61	-0.70
B_{30}	3.9	3.8	18.8	-0.54	-0.64

We have also observed in previous chapters that considering counterions had a strong influence in POM's adsorption onto the surface. In the model with counterions, Au-O_d distances were found between 2.8 and 3.1 Å, as shown in Table 6.2. These distances are in agreement with those found between 2.5 and 3 Å for $[AlW_{11}O_{39}]^{9-}$ on gold NPs.[6] It should be noted that, although the system is not identical, experimental data gives us an idea about the expected POM adhesion to the surface. On the other hand, we notice that when counterions are not considered, the interaction between the POM and surface is overestimated. Therefore, the POM was found too close to the surface, as we observed previously for silver surface. Hence, we could conclude that the model with counterions was in agreement with the experimental data whereas the model without is not.

Table 6.2 Au-O_d and Au-X distances (in Å) for $M_5AlW_{12}O_{40}$ with M = Cs and K.

	Au-O_d (Å)			Au-X (Å)		
site	Cs	K	-	K	Cs	-
B_0	2.81 – 2.86	2.79 – 2.83	2.12	6.53	6.49	5.58
Fcc_0	2.82 – 2.92	2.82 – 2.92	2.10 – 2.12	6.53	6.53	5.55
T_0	2.97 – 3.05	2.97 – 3.06	2.18 – 2.21	6.56	6.56	5.51
B_{30}	3.09 - 3.20	3.09 – 3.21	2.24 – 2.33	6.53	6.54	5.42

6.5.2. Electronic structure for $Cs_5AlW_{12}O_{40}$ and $K_5AlW_{12}O_{40}$

DOS and PDOS for $Cs_5AlW_{12}O_{40}$ and $K_5AlW_{12}O_{40}$, represented in Figure 6.4, illustrate that the nature of the counterion does not significantly alter the system's electronic structure. No charge transfer from the surface was expected for any system, since the W(d) band was found at nearly +0.8 eV with respect to the Fermi Level. From this information it can be inferred that the POM is not spontaneously reduced by the gold surface. The O(p) band was found 2 eV below the Fermi Level so the gap between W(p) and O(p) band was of 2.8 eV, perfectly matching the HOMO-LUMO gap for free $AlW_{12}O_{40}^{5-}$.[18]

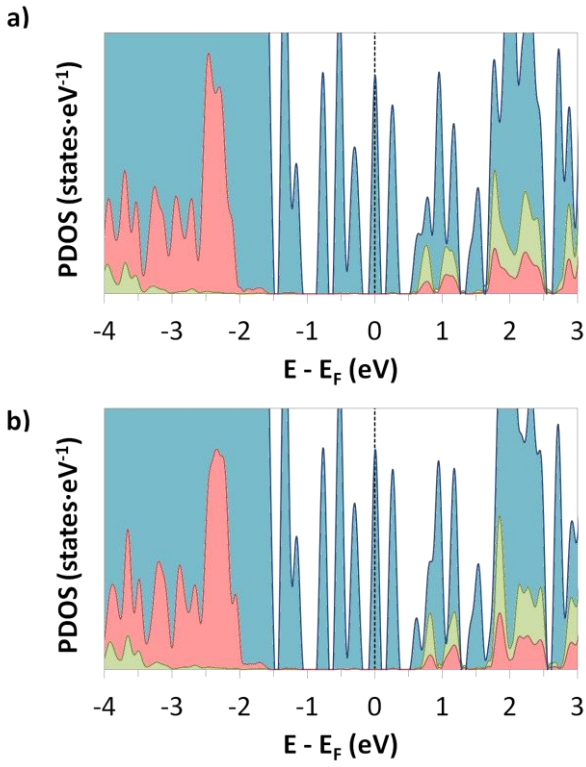

Figure 6.4 DOS and PDOS for a) $K_5AlW_{12}O_{40}$ and b) $Cs_5AlW_{12}O_{40}$ on Au(111). (DOS: blue, W(d) PDOS: green; O(p) PDOS: red).

Bader AIM charges were found to be coherent with the electronic structure of both systems, as shown in Table 6.3. Neither system reflected a spontaneous reduction of the POM nor the surface remained neutral. However, the gold surface suffered a strong layer polarization, which was reflected in the charge per layer that was found to be between one and two electrons per layer. It should be noted that this polarization was also found for the free gold slab. Some tests were performed for the isolated gold slab indicating that this polarization was not related to the number of gold layers. At this point we decided to include solvent around the POM to analyse the effect of solvation on the electronic structure and charges.

Table 6.3 Bader AIM charges for the Au(111) surface model, $AlW_{12}O_{40}$, and for $M_5AlW_{12}O_{40}$ (M=K, Cs) adsorbed on several active sites.

	M	$AlW_{12}O_{40}$	AlO_4	$W_{12}O_{36}$	ΣM	ΣAu	Au(1)	Au(2)	Au(3)
slab		-	-	-	-	0.0	-0.9	1.8	-0.9
B_0	-	-3.0	-3.1	0.1	-	3.0	2.1	1.7	-0.8
	K	-4.6	-3.1	-1.5	4.5	0.0	-0.8	1.8	-0.9
	Cs	-4.6	-3.1	-1.5	4.6	0.1	-0.8	1.8	-0.9
Fcc_0	-	-3.0	-3.0	0.0	-	3.0	2.2	1.8	-0.9
	K	-4.7	-3.2	-1.5	4.4	0.3	-0.7	1.9	-0.9
	Cs	-5.0	-3.2	-1.8	4.8	0.2	-0.7	1.8	-0.9
T_0	-	-3.1	-3.1	0.0	-	3.1	2.2	1.7	-0.8
	K	-4.7	-3.2	-1.5	4.4	0.3	-0.6	1.8	-0.9
	Cs	-5.0	-3.2	-1.8	4.8	0.2	-0.7	1.8	-0.8
B_{30}	-	-3.1	-3.1	0.0	-	3.1	2.2	1.8	-0.9
	K	-4.7	-3.1	-1.5	4.4	0.3	-0.7	1.8	-0.8
	Cs	-5.1	-3.2	-1.9	4.8	0.2	-0.6	1.7	-0.8

6.5.3. Solvation of $Cs_5AlW_{12}O_{40}$ on gold surface

For incorporating the solvation of $Cs_5AlW_{12}O_{40}$ on gold surface, we performed a 2 ns molecular dynamic simulation. In this case however, we kept counterions frozen and close to the polyoxometalate to reduce the computational cost of the strategy. From the simulation, we took a snapshot considering only the first solvation sphere. The solvation sphere was determined using the radial distribution function g(*r*) between POM oxygen and water oxygen atoms ($g(r)_{O\text{-}OW}$), as well as between counterions and water oxygens ($g(r)_{Cs\text{-}OW}$). Through g(*r*), both represented in Figure 6.5 we set that the first solvation sphere at 4.05 Å, and 3.65 Å from Cs atoms for OW and Cs atoms, respectively. The number of water molecules is 44 and the whole model is represented in Figure 6.3.

Two different calculations were performed from a snapshot randomly extracted from the simulation. We first determined the electronic structure of the single geometry and, following this, compared these results with the optimized geometry

obtained from the snapshot. This comparison primarily used to determine whether or not the optimization step was necessary.

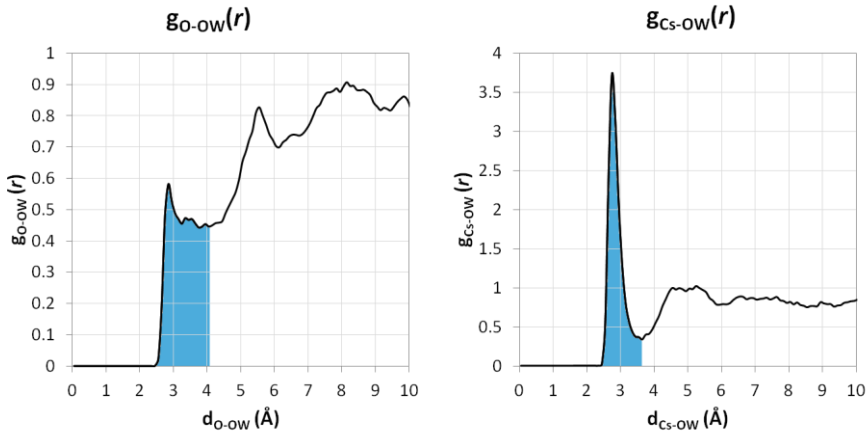

Figure 6.5 Radial distribution function for a) POM-oxygen and water-oxygen and b) Cs and water oxygen. The first solvation sphere is colored in blue.

DOS and PDOS before and after solvation are plotted in Figure 6.6. After incorporating solvent and counterions, W(d) was lowered by 0.4 eV in energy with respect to the non-solvated model, but still above E_F. The same stabilization was observed for the oxo band, which indicates that stabilization affected the entire adsorbate. In addition, these bands did not suffer a dramatic change in their shapes, nor in the general DOS. We conclude that solvent only corrected orbital positions slightly in this case, as was observed in previous chapters. Moreover, solvation does not change the unreduced character of the adsorbed POM.

The charge residing on the POM decreased from 4.6 to 3.9 e whereas the charge transferred from the surface increased by half electron. In addition, the charge residing on water was about two electrons. This data indicates that even though solvent stabilized the electronic structure, its disposition around the POM was far from the minimum, so Bader analysis crashed in delimiting atomic regions, as we observed in other systems. We proceeded as we did in the last chapter, and we optimized the structure to compute more accurate Bader AIM Charges. From the electronic structure we observed no changes with respect to the non-optimized system, as shown in Figure 6.6 b) and c).

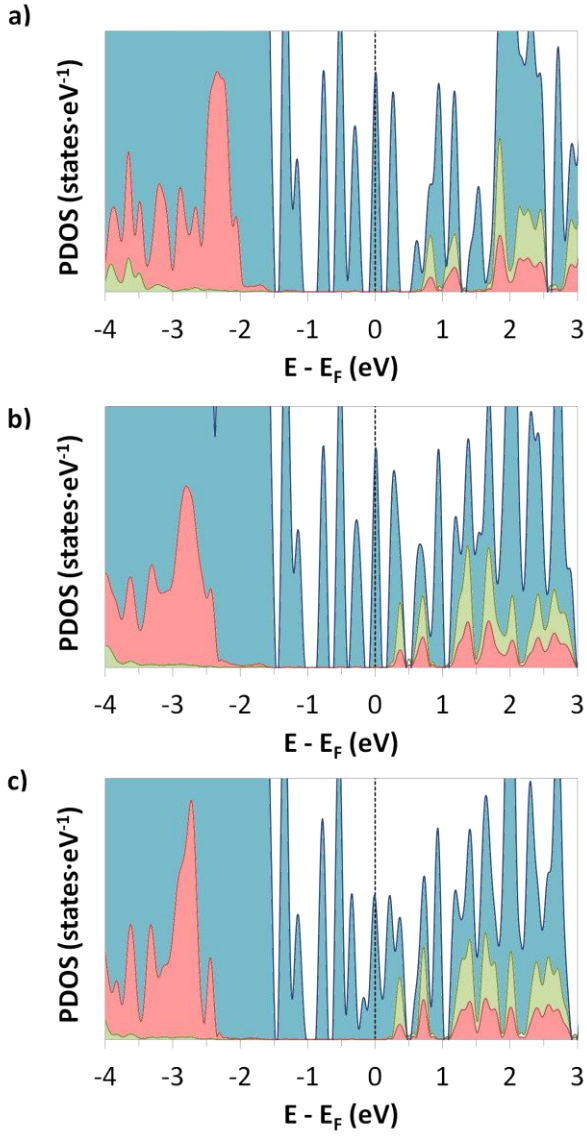

Figure 6.6 DOS (blue), W(d) (green) and O(p) (red) PDOS for a) non-solvated $Cs_5AlW_{12}O_{40}$, b) non-optimized solvated $Cs_5AlW_{12}O_{40}$, and c) optimized solvated $Cs_5AlW_{12}O_{40}$, on Au(111) surface.

According to the electronic structure, Bader AIM charges did not show any significant difference when compared with the non-optimized structure, meaning that in this case, geometry optimization did not enhance the atomic charges. However, the overall charge for counterions is higher than 5 e, meaning that Cs

atoms have a charge higher than 1 electron. This unexpected result is derived from the Bader partition, in which atomic regions are likely to be wrongly defined.

Table 6.4 Bader AIM charges for solvated $Cs_5AlW_{12}O_{40}$ adsorbed on B_0 - Au(111) active site.

site	ΣH_2O	$AlW_{12}O_{40}$	AlO_4	$W_{12}O_{36}$	ΣM	ΣAu	Au(1)	Au(2)	Au(3)
no solv.	-	-4.6	-3.1	-1.5	4.6	0.1	-0.8	1.7	-0.9
no opt.	-2.1	-3.9	-3.2	-0.7	5.3	0.7	-0.1	1.7	-0.9
opt.	-2.1	-3.7	-3.2	-0.5	5.1	0.6	-0.3	1.8	-0.8

6.6. Conclusions and perspectives

The strategy we described in the previous chapter revealed some limitations when highly charged POMs were involved in adsorption. Hence, we reformulated our strategy to address this drawback. Determination of the active site was performed by compensating the POM's charge with an appropriate number of counterions. After that we introduced the solvent by means of molecular dynamic simulations and extracted snapshots considering only the first solvation sphere. Although the electronic structure of POM was stabilized by the presence of solvent; Bader AIM charges did not show an acceptable behavior, even though we optimized the solvated system.

Based on the preliminary results obtained, we can infer that:

- ✓ Minima obtained with and without counterions in the model revealed that both methods reported different active sites. However, energy differences reported for all sites in the model with counterions show that all sites are probable and therefore, the error we obtained with this model is negligible.

- ✓ Compensate the charge with counterions allowing us to obtaining a good description of POM-surface distances, which are found within the experimental range of distances.

- ✓ As expected, gold surface is unable spontaneously reduce the aluminotungstate acid. W(d) states are found 0.8 eV above the Fermi level when solvent is not considered, and 0.4 eV when solvent is considered.

- ✘ Bader AIM Charges also show no spontaneous reduction when solvation is not considered. Unfortunately, they were in disagreement with the electronic structure when solvent was taken into account.

As we said, this work has not come to an end and further studies are required. In order to describe a robust strategy, we should also improve all the following aspects:

- Optimize the solvated structure in order to correct Bader AIM charges and solvate the POM adsorbed on other active sites.

- Analyze the adsorption *via* the C_3 POM symmetry axis. Adsorption *via* this axis is less favorable than via S_4 but only when counterions are not considered. Since relative energies are minimized when counterions are included, it would be interesting if in this situation and this coverage C_3 becomes more competitive.

- Apply this strategy to other surfaces like Au(100) and other metals such as Ag to check the validity of the strategy.

- Once the strategy is validated, determine how the laccunary $AlW_{11}O_{39}^{9-}$ is adsorbed on gold nanoparticles.

References Chapter 6
Gold Surface and Nanoparticles Model

[1] (a) A. Neyman, L. Meshi, L. Zeiri, I. A. Weinstock, *J. Am. Chem. Soc.* **2008**, *130*, 16480-16481; (b) Y. Wang, A. Neyman, E. Arkhangelsky, V. Gitis, L. Meshi, I. A. Weinstock, *J. Am. Chem. Soc.* **2009**, *131*, 17412-17422.

[2] A. Troupis, A. Hiskia, E. Papaconstantinou, *Angew. Chem., Int. Ed.* **2002**, *41*, 1911-1914.

[3] (a) X. Xing, R. Liu, X. Yu, G. Zhang, H. Cao, J. Yao, B. Ren, Z. Jiang, H. Zhao, *J. Mater. Chem. A* **2013**, *1*, 1488-1494; (b) T. Hsu-Yao, K. P. Browne, N. Honesty, Y. J. Tong, *Phys. Chem. Chem. Phys.* **2011**, *13*, 7433-7438; (c) K. M. Wiaderek, J. A. Cox, *Electrochim. Acta* **2011**, *56*, 3537-3542; (d) A. Corma, S. Iborra, F. X. Llabrés i Xamena, R. Montón, J. J. Calvino, C. Prestipino, *J. Phys. Chem. C* **2010**, *114*, 8828-8836.

[4] Y. Wang, I. A. Weinstock, *Chem. Soc. Rev.* **2012**, *41*, 7479-7496.

[5] Y. Wang, O. Zeiri, S. Sharet, I. A. Weinstock, *Inorg. Chem.* **2012**, *51*, 7436-7438.

[6] S. Sharet, E. Sandars, Y. Wang, O. Zeiri, A. Neyman, L. Meshi, I. A. Weinstock, *Dalton Trans.* **2012**, *41*, 9849-9851.

[7] A. Proust, B. Matt, R. Villanneau, G. Guillemot, P. Gouzerh, G. Izzet, *Chem. Soc. Rev.* **2012**, *41*, 7605-7622.

[8] J. P. Perdew, J. A. Chevary, S. H. Vosko, K. A. Jackson, M. R. Pederson, D. J. Singh, C. Fiolhais, *Phys. Rev. B: Condens. Matter* **1992**, *46*, 6671-6687.

[9] P. E. Blöchl, *Phys. Rev. B: Condens. Matter* **1994**, *50*, 17953-17979.

[10] H. J. Monkhorst, J. D. Pack, *Phys. Rev. B: Condens. Matter* **1976**, *13*, 5188-5192.

[11] (a) R. F. W. Bader, *Atom in Molecules: A Quantum Theory*, Oxford University Press, Oxford, **1990**; (b) G. Henkelman, A. Arnaldsson, H. Jonsson, *Comput. Mater. Sci.* **2006**, *36*, 354-360.

[12] L. Martínez, R. Andrade, E. G. Birgin, J. M. Martínez, *J. Comput. Chem.* **2009**, *30*, 2157-2164.

[13] W. L. Jorgensen, J. Chandrasekhar, J. D. Madura, R. W. Impey, M. L. Klein, *J. Chem. Phys.* **1983**, *79*, 926-935.

[14] (a) X. Lopez, C. Nieto-Draghi, C. Bo, J. B. Avalos, J. M. Poblet, *J. Phys. Chem. A* **2005**, *109*, 1216-1222; (b) F. Leroy, P. Miro, J. M. Poblet, C. Bo, J. B. Avalos, *J. Phys. Chem. B* **2008**, *112*, 8591-8599; (c) H. Heinz, R. A. Vaia, B. L. Farmer, R. R. Naik, *J. Phys. Chem. C* **2008**, *112*, 17281-17290.

[15] M. P. Allen, D. J. Tildesley, *Computer Simulation of Liquids*, Clarendon Press, Oxford, **1989**.

[16] (a) S. Nosé, *J. Chem. Phys.* **1984**, *81*, 511-519; (b) S. Nosé, *Mol. Phys.* **1984**, *52*, 255-268.

[17] W. Humphrey, A. Dalke, K. Schulten, *J. Molec. Graphics* **1996**, *14*, 33-38.

[18] J. M. Maestre, X. Lopez, C. Bo, J. M. Poblet, N. Casan-Pastor, *J. Am. Chem. Soc.* **2001**, *123*, 3749-3758.

Chapter 7
Concluding Remarks

UNIVERSITAT ROVIRA I VIRGILI
COMPUTATIONAL MODELLING OF POLYOXOMETALATES ADSORBED ON METALLIC SURFACES
Xavier Aparicio Anglès
Dipòsit Legal: T. 1525-2013

In the present thesis we have studied the adsorption of α-Keggin anions on silver and gold surfaces. This chapter is devoted to summarizing the most important achievements and conclusions presented throughout this thesis.

- Based on the structural information reported by Gewirth and co-workers, we have determined the adsorption site and mode for $[\alpha\text{-}SiW_{12}O_{40}]^{4-}$ on Ag(100) and Ag(111) for two unique unit cells in each surface. The results obtained revealed that electrostatic interactions between neighbouring POMs should be considered in the maximum coverage situation.

- We computed vibrational frequencies and simulated the infrared spectra for $[\alpha\text{-}SiW_{12}O_{40}]^{4-}$ on silver surfaces for different active sites. We have reproduced the experimental spectra and reassigned intense bands, indicating that the Ag-O stretching generates the most intense signal in almost all spectra.

- To accurately reproduce the electronic structure, environmental effects must be taken into account. Therefore, a strategy combining both Quantum Mechanics and Classical Molecular Dynamics has been designed to introduce the effect of solvent and counterions in calculations.

- After the inclusion of the environment, the computed electronic structures have revealed the spontaneous reduction of the $[\alpha\text{-}SiW_{12}O_{40}]^{4-}$ after adsorption on the silver surface.

- A comparative study of the behaviour of $[\alpha\text{-}XW_{12}O_{40}]^{q-}$ with X = Al, Si, and P, and q = 5, 4, and 3 was performed. We also studied the isostructural $[\alpha\text{-}XMo_{12}O_{40}]^{q-}$, with X = Si, and P, and q = 4, and 3 revealed some limitations of the strategy, which overestimated the interaction between both moieties, an errar that was reflected in the distance to the surface. To account for this, we introduced a final optimization procedure, including solvent and counterions, to correct these distances.

- Following optimization, the electronic structure of all systems explored has revealed that an electron is transferred from the surface to the adsorbate.

- A modification of our initial strategy has been proposed for studying highly charged polyoxometalates on gold nanoparticles, firstly including the counterions around the polyoxometalate. In this system, in which the nanoparticle is modelled as a surface, no spontaneous reduction is observed for $[\alpha\text{-}AlW_{12}O_{40}]^{5-}$.

UNIVERSITAT ROVIRA I VIRGILI
COMPUTATIONAL MODELLING OF POLYOXOMETALATES ADSORBED ON METALLIC SURFACES
Xavier Aparicio Anglès
Dipòsit Legal: T. 1525-2013

UNIVERSITAT ROVIRA I VIRGILI